EIS INVESTIGATION OF CARBON DIOXIDE AND HYDROGEN SULFIDE CORROSION UNDER FILM FORMING CONDITIONS

A thesis presented to
the faculty of the
Fritz J. and Dolores H. Russ
College of Engineering and Technology
of
Ohio University

In partial fulfillment

of the requirements for the degree

Master of Science

Shilpha R. Parakala
June 2005

This thesis entitled

EIS INVESTIGATION OF CARBON DIOXIDE AND HYDROGEN SULFIDE CORROSION UNDER FILM FORMING CONDITIONS

by

Shilpha R. Parakala

has been approved for

the Department of Chemical Engineering

and the Russ College of Engineering and Technology by

Srdjan Nesic

Professor of Chemical Engineering

Dennis Irwin

Dean, Russ College of Engineering and Technology

PARAKALA, SHILPHA P. M.S. JUNE 2005. Chemical Engineering

EIS Investigation of Carbon dioxide and Hydrogen sulfide Corrosion Under Film Forming Conditions (132 p.)

Director of Thesis: Srdjan Nesic

The present study has been conducted to find the corrosion mechanisms and rates of an AISI 1018 steel in the presence of CO_2 and trace amounts of H_2S using classical electrochemical techniques. The results obtained from experiments using electrochemical impedance spectroscopy measurements were theoretically analyzed by a semi-mechanistic model to reveal the conditions on the surface of the specimen used in the experiment. The experiments were designed to see the effect of different saturation values of iron carbonate and iron sulfide in the bulk solution on the corrosion rate of the sample. The experiments were conducted in a large scale (1000 lit) hastelloy flow loop at a fixed temperature of 60 ^{o}C and total pressure of 7.9 bar. All experimental conditions were monitored regularly for the duration of the experiment.

It was observed that the presence of trace amounts of H_2S in the system decreased the corrosion rate significantly over time under the specific experimental conditions studied. This was due to the formation of an iron carbonate scale or iron sulfide scale, or both, which acted as a barrier to the diffusion of the corrosive species to the surface of the metal, thus decreasing corrosion rate.

Approved: Srdjan Nesic

Professor of Chemical Engineering

DEDICATION

To

Rama Rani and Vijayapal Reddy Parakala (my parents)

and

Ulpha Reddy Parakala (my sister)

and

Rama Krishna Malka (my husband)

Whose mental support made this work a success

ACNOWLEDGEMENTS

I would like to express my gratitude to Dr. Srdjan Nesic for his continuous academic and moral support. His attitude towards everything in life has inspired me and always encouraged me to perform better in every aspect of my life. This thesis is a tribute to his immense patience and his exceptional guidance and mentorship during my entire stay at the Ohio University.

I would like to acknowledge my indebtedness to Dr. Sandra Hernandez, Dr. Daniel Gulino, and Dr. David Young for their priceless suggestions.

I would like to acknowledge my indebtedness to Mr. Bruce Brown for his immense patience and intense help during the experimentation.

I would also like to thank the technical staff at the Institute for Corrosion and Multiphase Technology, including Mr. Al Schubert and Mr. John Goettge for their assistance in technical matters, and the research students: Rama Malka, Kunal Chokshi, and Wei Sun for providing a wonderful research environment.

I would also like to acknowledge the academic contribution and financial support of consortium of companies whose continuous financial support and technical guidance made this research at the Ohio University's Institute for Corrosion and Multiphase Technology possible.

TABLE OF CONTENTS

LIST OF TABLES

LIST OF FIGURES

CHAPTER 1: INTRODUCTION

The corrosion of steel by CO_2 and CO_2/H_2S is a significant problem in oil refineries and natural gas treatment facilities and can occur at all stages of production, from down hole to surface processing equipment (Hausler and Stegman, 1988). The capital and operational expenditures and health, safety, and environment of the oil and gas industry are enormously affected by corrosion (Kermani and Morshed, 2003). The simultaneous presence of CO_2 and H_2S in produced fluids makes for a very aggressive environment which leads to severe corrosion of mild steel (Videm and Kvarekval, 1994), which still constitutes an estimated 99% of the pipeline material used in the oil and gas industry. In the past two decades, pipeline corrosion investigations and predictions have generated an extensive literature on "sweet" CO_2 corrosion, but there are very few studies that enlighten CO_2/H_2S corrosion. Hence, more emphasis has been placed on H_2S's role in the CO_2 corrosion process since it has been shown by some researchers that even small concentrations of H_2S can radically affect the corrosion rate of mild steel (Kvarekval *et al.,* 2002), and by others that the corrosion rate of the metal decreases radically in the presence of trace amounts of H_2S in the system (Lee *et al.*, 2003, Brown *et al.*, 2003, Brown *et al.*, 2004).

The electrochemistry of CO_2/H_2S corrosion has been investigated to a certain extent at high temperatures and atmospheric pressures at a concentration of H_2S up to 300 ppm (Lee et al., 2003) and at high temperatures and high pressures at a concentration of H_2S up to 100 ppm (Brown *et al.*, 2003, Brown *et al.*, 2004). At present, it is imperative to evaluate the effect of other complicated parameters such as formation of protective

scales, effect of inhibitors, hydrocarbons, glycols, methanol, condensation in dry gas transport, and multi-phase flow on the corrosion mechanism in the presence of H_2S. Hence a dedicated study is considered where the effect of film formation on the surface of the metal in CO_2/H_2S environment is investigated. Also, this kind of basic data is indispensable for the development of more unswerving mechanistic CO_2/H_2S corrosion prediction models.

In order to fulfill this objective, classical electrochemical techniques like linear polarization and electrochemical impedance spectroscopy will be used in combination with weight loss to find the corrosion rates in the CO_2/H_2S environment. The experiments will be performed in a high temperature, high pressure, large scale (2000 lit) H_2S hastelloy flow loop where flow conditions are greatly similar to industrial conditions and offer an excellent opportunity to do the study. The temperature and total pressure at which the experiments will be done are 60 ^oC and 7.9 bar, respectively, at different concentrations of Fe^{+2} and H_2S, and different pH values. The experimental conditions were chosen to result in different saturation values for both iron sulfide and iron carbonate films.

The theoretical interpretation of the data from electrochemical impedance spectroscopy (Nyquist plots) was done using an appropriate mechanistic mathematical model developed to analyze the EIS results in the presence of H_2S. The cathodic reaction mechanism used in the mathematical model for the analysis of EIS data from the experiments has been supported by many researchers (Bonis and Crolet, 1989, Gray *et al.,* 1990, Nesic *et al.,* 1995).

Hence, this project aims to investigate the corrosion rate of AISI 1018 steel in a CO_2/H_2S environment and to model the data according to changes in parameters like diffusivity, boundary layer thickness and porosity of the surface film, if any, and this model will be integrated into the currently existing OU MULTICORP V3.0 corrosion prediction model for better prediction of corrosion rates in the presence of H_2S.

CHAPTER 2: LITERATURE REVIEW

CO_2 corrosion

Carbon dioxide corrosion, or "sweet corrosion", of carbon steel is a major technical problem in the oil and gas industry. The presence of CO_2 gas in the aqueous phase (CO_2 saturated aqueous solution) in contact with the surface of the metal leads to corrosion and consequent failures. The basic CO_2 corrosion reaction mechanisms have been well understood and accepted by many researchers through the work done over the past few decades (Nesic *et al.,* 1995). The major chemical reactions include CO_2 dissolution and hydration to form carbonic acid,

$$CO_{2(g)} \Leftrightarrow CO_{2(aq)} \tag{2-1}$$

$$CO_{2(aq)} + H_2O_{(aq)} \Leftrightarrow H_2CO_{3(aq)} \tag{2-2}$$

The carbonic acid then dissociates into bicarbonate and carbonate ions in two steps:

$$H_2CO_{3(aq)} \Leftrightarrow H^+{}_{(aq)} + HCO^-_{3_{(aq)}} \tag{2-3}$$

$$HCO^-_{3\,(aq)} \Leftrightarrow H^+{}_{(aq)} + CO^{2-}_{3\,(aq)} \tag{2-4}$$

It was proposed that carbonic acid provides a reservoir of H^+ ions at a given pH value of the solution. Therefore, hydrogen ion reduction or hydrogen evolution is assumed to be the most dominant cathodic reaction.

When hydrogen ions diffuse through the diffusion boundary layer to the metal surface, hydrogen evolution involving an intermediate adsorbed hydrogen atom take place according to the following reactions.

$$H^+ + e^- \leftrightarrow H_{ads} \tag{2-5}$$

$$H^+ + e^- + H_{ads} \leftrightarrow H_{2\,ads} \tag{2-6}$$

$$H_{ads} + H_{ads} \leftrightarrow H_{2\,ads} \quad (2\text{-}7)$$

The resulting adsorbed hydrogen atom from the reduction of hydrogen ion by equation (2-5) or can either recombine with another adsorbed hydrogen atom to form H_{2ads} as in equation (2-7) or it can under go another charge transfer reaction as in equation (2-6). The additional charge transfer reaction was first proposed by Heyrosky and was also known as Heyrosky's reaction (Heyrovsky, 1925).

The electrochemical reactions at the steel surface include the anodic dissolution of iron being the oxidation of iron at the metal surface, given by (Bockris et al., 1961):

$$Fe + OH^- \rightarrow FeOH + e^- \quad (2\text{-}8)$$

$$FeOH \rightarrow FeOH^+ + e^- \quad (2\text{-}9)$$

$$FeOH^+ \rightarrow Fe^{2+} + OH^- \quad (2\text{-}10)$$

The net anodic reaction is given by:

$$Fe \rightarrow Fe^{2+} + 2e^- \quad (2\text{-}11)$$

and two cathodic reactions, namely reduction of H^+ ions and direct reduction of carbonic acid as follows:

$$2H^+ + 2e^- \rightarrow H_2 \quad (2\text{-}12)$$

$$2H_2CO_3 + 2e^- \rightarrow H_2 + 2HCO_3^- \quad (2\text{-}13)$$

Despite more than three decades of intense research, it is still not known which of the two reactions among equation (2-12) and equation (2-13) actually occur on the metal surface. Hence, the net cathodic current was assumed to be the sum of the currents of the two cathodic reactions (Gray *et al., 19*90). Therefore, CO_2 corrosion is an electrochemical process with the overall combined reaction given by:

$$Fe + CO_2 + H_2O \Leftrightarrow FeCO_3 + H_2 \quad (2\text{-}14)$$

Thus, CO_2 corrosion leads to the formation of a solid corrosion product, iron carbonate ($FeCO_3$), which, when precipitated, could form a protective or a non-protective layer, depending on several environmental conditions such as iron concentration, pH of the solution, temperature, and partial pressure of CO_2 in the solution.

H_2S Corrosion

There are a limited number of studies that cover H_2S corrosion, particularly when compared to the extensive literature available on CO_2 corrosion (Brown *et al.,* 2003). The few experimental studies that have been published in the open literature (Ikeda *et al.,* 1984, Videm *et al.,* 1994, Valdes *et al.,* 1998) are limited to small scale glass cells and autoclaves whose geometry and flow conditions vary significantly from the actual flow conditions in the field. The presence of even small amounts of H_2S with CO_2 has been proven to increase the general and localized corrosion rate radically (Videm and Kvarekval, 1994).

The reactions that happen in the system when there is H_2S present in the system are as follows:

$$H_2S_{(g)} \Leftrightarrow H_2S_{(aq)} \quad (2\text{-}15)$$

The dissociation of aqueous H_2S happens as follows:

$$H_2S_{(aq)} \rightarrow H^+_{(aq)} + HS^-_{(aq)} \quad (2\text{-}16)$$

$$HS^-_{(aq)} \rightarrow H^+_{(aq)} + S^{2-}_{(aq)} \quad (2\text{-}17)$$

Therefore, hydrogen ion reduction or hydrogen evolution is assumed to be the most dominant cathodic reaction in H_2S corrosion also.

A probable mechanism for iron dissolution in aqueous solutions containing H_2S as proposed by researchers (Ma *et al.,* 1998) is as follows:

$$Fe + H_2S + H_2O \Leftrightarrow FeSH^-_{ads} + H_3O^+ \quad (2\text{-}18)$$

$$FeSH^-_{ads} \Leftrightarrow Fe(SH)_{ads} + e^- \quad (2\text{-}19)$$

$$Fe(SH)_{ads} \rightarrow FeSH^+ + e^- \quad (2\text{-}20)$$

The species $FeSH^+$ at the electrode surface could be incorporated directly into a growing layer of mackinawite (Shoesmith *et al.,* 1980) according to the following reaction:

$$FeSH^+ \rightarrow FeS_{(1-x)} + xSH^- + (1-x)H^+ \quad (2\text{-}21)$$

or it may be hydrolyzed to yield Fe^{+2} depending upon the pH value of the solution (Ma *et al.,* 1998) via the reaction

$$FeSH^+ + H_3O^+ \Leftrightarrow Fe^{2+} + H_2S + H_2O \quad (2\text{-}22)$$

If reaction (2-21) leads to local super saturation of $FeS_{(1-x)}$ at the electrode surface, nucleation and growth of one or more forms of iron sulfides, such as mackinawite, cubic ferrous sulfide, or troilite occurs. H_2S begins to exhibit its inhibitive effect with the formation of mackinawite via reaction (2-21). This mackinawite can convert into troilite or other kinds of sulfides with varying protective properties. The protective nature and

composition of the corrosion product depend greatly on the pH of the solution and the concentration of H_2S in the solution.

At lower values of pH (<2.0), iron is dissolved and iron sulfide is not precipitated on the surface of the metal due to a very high solubility of iron sulfide phases at pH values less than 2.0. In this case, H_2S exhibits only the accelerating effect on the dissolution of iron. At pH values from 3.0 to 5.0, inhibitive effect of H_2S is seen as $FeSH^+$ species may form mackinawite via reaction (2-21). The metastable mackinawite can convert into other forms of sulfides which are more protective such as troilite, and the protective or inhibitive effect of H_2S depends on the stability and protectiveness of the transformed sulfide (Ma *et al.,* 2000).

H_2S concentration has an immense influence on the protective ability of the sulfide film formed. As the concentration of H_2S increases, the amount of mackinawite in the film also increases (Shoesmith *et al.,* 1980), which has some structural defects resulting in an inability to effectively prevent iron corrosion. In addition, when the concentration of H_2S is higher, an appreciable amount of mackinawite deposits on the electrode or metal surface at a pH range of 3.0 to 5.0, forming a loose film on the surface which is not contributory to the inhibiting effect.

Having outlined the mechanism of corrosion in the presence of CO_2/H_2S, it could be anticipated that there are many environmental factors, such as solution chemistry, flow velocity, temperature, pressure, concentration of H_2S, pH value, etc., which determine the corrosion rate of the metal. The formation of the corrosion product scales due to the

environmental conditions which act as a diffusion barrier for the corrosive species could also have a significant impact on the corrosion rate of the metal.

Corrosion product film formation

Different kinds of iron carbonate corrosion product films

CO_2/H_2S corrosion on the metal surface is strongly dependent on the type of corrosion product film formed on the surface of the metal during the corrosion process. The precipitation rate or the formation of these films depends on various environmental factors and greatly on the concentration of species. The stability, protectiveness, and adherence of these films determine the nature and the rate of corrosion (uniform corrosion / localized corrosion). Depending on the composition, the corrosion films can be classified as follows:

a) Iron carbide (Fe_3C):

Iron carbide is an undispersed component of mild steel, which is left behind after the corrosion of iron from the steel structure. Iron carbide films are conductive electrically, very porous, and non-protective (Jasinski, 1987). These films can significantly affect the corrosion process by either decreasing the corrosion rate by acting as a diffusion barrier, or increasing the corrosion (Gulbrandsen *et al.*, 1998) by increasing the active specimen surface area by forming a conductive bridge between the counter and working electrodes. Also, this kind of film formation could result in galvanic coupling of the film to the metal or acidification of the solution inside the corrosion product film which is very dangerous and by far the strongest reason that could be given for the occurrence of localized corrosion.

b) Iron carbonate ($FeCO_3$):

In a CO_2 corrosion situation, iron carbonate is formed from the reaction of iron and carbonate ions given by:

$$Fe^{2+} + CO_3^{2-} \Leftrightarrow FeCO_3(s) \tag{2-23}$$

The rate of precipitation of iron carbonate is so slow that most often the precipitation kinetics rather than the thermodynamics come into consideration. Precipitation of solid iron carbonate occurs when the product of the concentrations of Fe^{2+} and CO_3^{2-} ions in the solution exceed a certain limit known as the solubility limit.

The rate of precipitation of the iron carbonate ($R_{FeCO_{3(S)}}$) is governed by an equation given as follows (Van Hunnik *et al.,* 1996):

$$R_{FeCO_{3(S)}} = \frac{A}{V} \cdot f(T).K_{sp} \cdot f(SS) \tag{2-24}$$

Where supersaturation of iron carbonate is defined as:

$$SS = \frac{c_{Fe^{2+}} c_{CO_3^{2-}}}{K_{sp}} \tag{2-25}$$

Since CO_3^{2-} ion concentration is dependent on the pH, it can be deduced in broad-spectrum that:

$$SS = f(Fe^{2+}, pH) \tag{2-26}$$

Therefore, supersaturation and temperature are the most important factors affecting the rate of precipitation, and nature and protectiveness of the iron carbonate film. Precipitation of iron carbonate on the surface of the metal decreases the corrosion rate by acting as a diffusion barrier for the corrosive species to travel to the metal surface

by blocking few areas on the steel surface and preventing electrochemical reactions from happening on the surface (Nesic *et al.*, 2003).

Different kinds of iron sulfide corrosion product films

The structure and composition of the protective FeS film depends greatly on the concentration of H_2S in the system. The species $FeSH^+$ at the electrode surface could be incorporated directly into a growing layer of mackinawite (Shoesmith *et al.,* 1980) according to reaction (2-21), or it may be hydrolyzed to yield Fe^{+2} depending upon the pH value of the solution (Ma *et al.,* 1998) via reaction (2-22). At a solution pH value of 3.0-5.0, with a small concentration of H_2S, a protective film of FeS inhibited the corrosion rate of the metal coupon (Ma *et al.,* 2000). In nearly neutral pH (7.0 – 7.4) and at room temperature, mackinawite forms through a solid state reaction, while at a pH value between 5.5 and 7.0, amorphous FeS precipitates (Harmandas and Koutsoukos,1996).

The kinetics of FeS formation are very complicated, and the mechanism involved in the formation of the FeS is even more so. The solution supersaturation (σ_{FeS}) of FeS is governed by the following equation (Harmandas and Koutsoukos,1996):

$$\sigma_{FeS} = \Omega^{1/2} - 1 \qquad (2\text{-}27)$$

Where $\Omega = \dfrac{c_{Fe^{2+}} c_{S^{2-}}}{K_{sp,FeS}}$, $K_{sp,FeS}$ is the thermodynamic solubility product for FeS and Ω is the super saturation ratio relative solution supersaturation for FeS.

It could also be observed that the supersaturation of FeS is a strong function of the concentrations of H_2S and Fe^{2+} and of temperature. At the metal surface, because of the

fast depletion of H^+ ions, the local pH near the metal surface is greater than the bulk pH. This could result in a larger supersaturation of FeS and precipitation happens even faster at the metal surface. Since iron sulfide is a semi-conductive film, precipitation of iron sulfide in combination with other kind of non-conductive film (eg. $FeCO_3$) on the surface of the metal could decrease the corrosion rate by acting as a diffusion barrier for the corrosive species to travel to the metal surface. If FeS is the only one material precipitating on the surface of the metal, even if the film is thick, the corrosion rate may not be low because of the conductivity of the film. Also, precipitation of only FeS on the surface could result in false depiction of corrosion rate if electrochemical techniques are used. The reason is the interference of the conductive FeS film in the process of electron transfer.

Due to corrosion of the pipe wall (dissolution of Fe from pipe wall), the water phase in the pipeline transporting oil and gas accumulates Fe^{++}. The amount of Fe^{++} has an immense influence on the formation and nature of the iron carbonate and iron sulfide scale. Increased Fe^{++} concentration can lead to higher supersaturation of both iron carbonate and iron sulfide according to equations(2-24) and (2-27), respectively, which could increase the precipitation rate of iron carbonate and sulfide. The precipitated film could be very protective by being dense and acting as a diffusion barrier to the corrosive species, or it could be porous and thick and still could not be protective. Porous and incomplete films are very hazardous to the pipe wall as they are very favorable for localized attack of the metal. Hence, porosity of the film is the most important factor in determining the corrosion rate of the metal under filming conditions.

An increase in the Fe^{++} ion concentration could lead to a higher supersaturation value which could increase the precipitation rate of iron carbonate and iron sulfide and decrease the uniform corrosion rate if the film is dense and uniform or could increase the chances of localized corrosion if the film is porous.

The growth of iron carbonate is a very slow, temperature dependent process (Johnson and Tomson, 1991, Dugstad, 1992). Increasing in the temperature increases the precipitation rate of iron carbonate and iron sulfide significantly. The increase in temperature also leads to acceleration of all of the other processes involved in corrosion, (electrochemical reactions, chemical reactions, transport of species etc.) which leads to an increase in the corrosion rate. Since temperature has a very high impact on the electrochemical processes and the corrosion, it is imperative that the experiments be conducted at high temperature.

****

In summary, little data exists about CO_2 and H_2S corrosion in the open literature, and the data extracted over the last two decades by few researchers since about CO_2 – H_2S corrosion was at low temperatures (room temperature) and low pressures, the conditions which are very far from realistic oil and gas field conditions. Since there is no adequate data for the situation, the effect of different complicated parameters like the formation of protective scales, effect of inhibitors, hydrocarbons, glycols on the corrosion mechanism in the presence of H_2S is still not understood well. Hence there is a dire need for experimental data at high pressures and high temperatures to investigate the mechanism of CO_2-H_2S corrosion, since this is the major step in reducing the corrosion

costs, developing preventive measures, and mitigating the corrosion of oil and gas pipe lines.

The EIS technique is a less intrusive corrosion measurement technique that is very sensitive to the surface conditions of the specimen and could reveal very vital information about the different processes happening at different paces on the surface of the sample. Even though the corrosion occurring on the metal is definitely a surface phenomenon, very few researchers used the technique to analyze experimental data to reveal the vital parameters involved in the surface corrosion process. The following chapter gives an introduction about the EIS theory, expressions given by various authors to calculate the overvoltage responses for different processes that could be used to calculate the impedance response of a system to an input AC current signal.

CHAPTER 3: EIS THEORY

Introduction

AC Impedance or Electrochemical Impedance Spectroscopy (EIS) technique is a less intrusive transient electrochemical measurement technique that is very sensitive to the surface characteristics of the specimen and can extract reliable qualitative information about the processes happening on the surface of the specimen. Even though the technique is very sensitive and could provide us with an exclusive insight about some of the very important parameters which influence the corrosion mechanism, very few researchers have used this technique to interpret the experimental data in corrosion experiments (Keddam *et al.,* 1981), (Altoe *et al.*, 1996), (Ma *et al.,* 1998), (Ma *et al.,* 2000). Most generally, the application of the EIS technique has been used by researchers for the evaluation of corrosion inhibitors, anodic coatings, and polymeric coatings. A brief introduction to the measurement technique is given below:

The ability of a circuit element to resist the flow of electrical current is called resistance. The resistance of an ideal resistor is defined by Ohm's law as the ratio between the voltage E and current I as follows:

$$R = \frac{E}{I} \tag{3-1}$$

An ideal resistor follows Ohm's law at all voltage and current levels and its resistance value is independent of frequency. Circuit elements which exhibit much more complex behavior are encountered in real world situations where the simple concept of ideal resistor cannot be applicable. Impedance is a more general circuit parameter which

is similar to resistance in a way that it is also a measure of the ability of the circuit to resist the flow of electrical current but it is more complicated in its behavior.

Electrochemical impedance is usually measured by applying an AC potential or current signal of varying frequencies and measuring the response of the cell which is AC current or potential respectively. Variation of the frequency of the applied signal during the measurement provides the unique opportunity to capture different processes (different reactions also) happening on the surface of the metal at different rates. Since electrochemical cells are not linear in their behavior, electrochemical impedance is measured using an AC signal of a very small amplitude so that the response of the cell is pseudo-linear with in the range of the applied current or voltage signal.

Consider an AC sinusoidal current signal as an input, given by

$$i = I\sin(\omega t) \tag{3-2}$$

where , I is the magnitude of current in A, ω is the frequency of the signal in s^{-1}, t is the time period of the signal in s,

The response to the input current signal is the sinusoidal voltage signal given by

$$e = E\sin(\omega t + \phi) \tag{3-3}$$

where , E is the magnitude of voltage in V, φ is the phase difference between the voltage and the current signals.

In a linear (or pseudo-linear) system, the potential response to a sinusoidal input current will be a sinusoid at the same frequency with a phase shift. So, applying the Ohm's law for AC circuits to calculate the impedance Z of the cell,

$$Z = \frac{e}{i} = \frac{E\sin(\omega t + \varphi)}{I\sin(\omega t)} \tag{3-4}$$

Using Euler's relationship,

$$\exp(j\varphi) = \cos(\varphi) + j\sin(\varphi) \tag{3-5}$$

The impedance can be written as

$$Z = \frac{E\sin(\omega t + \varphi)}{I\sin(\omega t)} = Z_0\exp(j\varphi) = Z_0(\cos(\varphi) + j\sin(\varphi)) \tag{3-6}$$

where $Z_0 = \frac{E}{I}$

The expression for impedance *Z* is composed of both real and imaginary parts. A plot of real part of impedance on X-axis and negative of imaginary part of impedance on Y-axis is called a Nyquist plot. Figure 1 shows the shape of Nyquist plot for the simple equivalent circuit with one time constant, as shown in Figure 2. The impedance on the Nyquist plot can be represented as a vector of length $|Z|$ and the angle between the vector and the X-axis, φ, is the phase. The major short coming of a Nyquist plot is that the frequency used to create a particular data point cannot be recognized. The semicircle shown in Figure 1 is characteristic of a single "time constant" (for e.g. a combination of an ideal capacitance with a single resistance). EIS plots for real cases contain more than one time constant and often only a portion of one or more of the semicircles is seen.

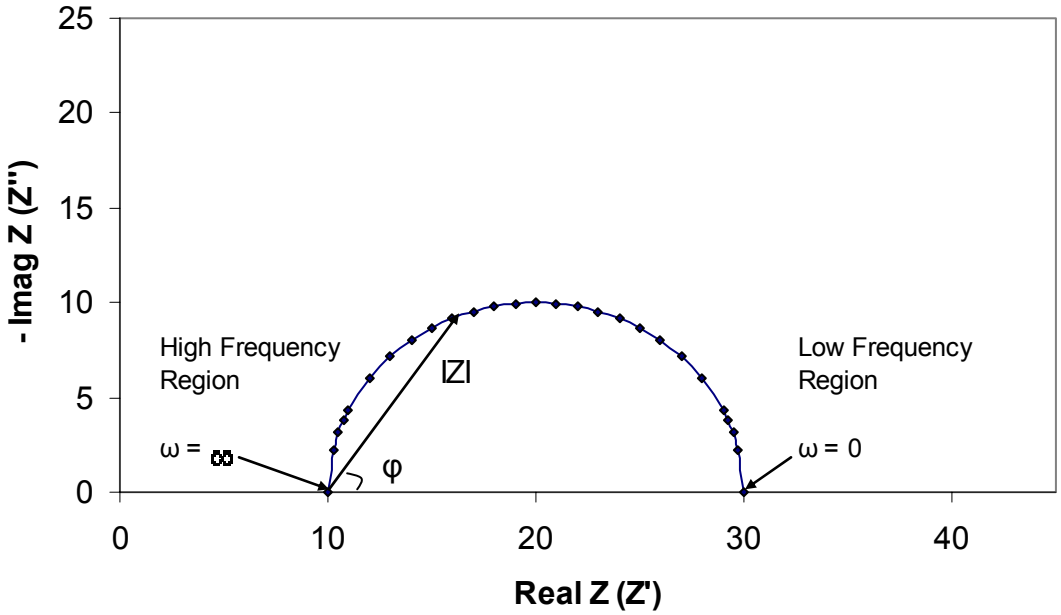

Figure 1. Nyquist plot with one time constant for the circuit shown in Figure 2.

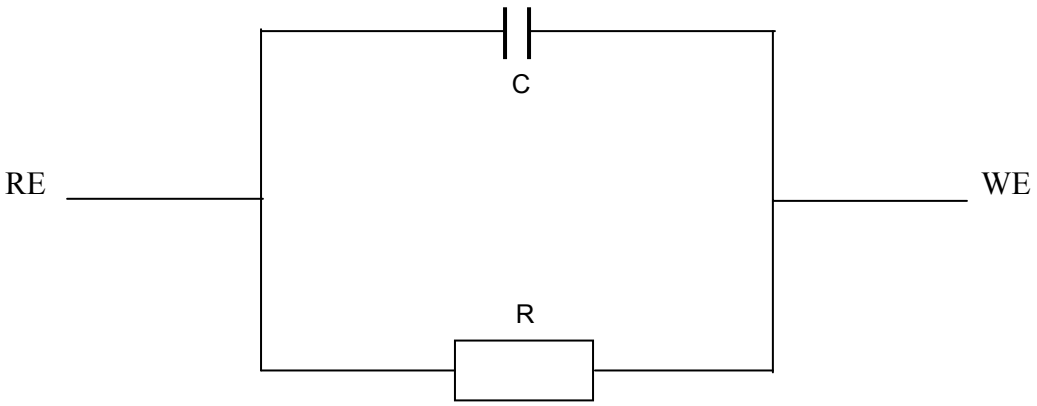

Figure 2. Simple circuit with one time constant.

EIS data was most commonly analyzed by researchers by fitting the data to an equivalent electrical circuit model (Ma et al., 2000, Darowicki, 1993, Kinsella et al., 1998). The elements in the model are common electrical elements such as capacitors and resistors, for example the solution resistance was substituted by a resistor and the electrochemical double layer by a non ideal capacitor (constant phase element). In order to extract useful information from modeling the EIS data, the model should reflect the electrochemical cell that is used to collect the data. Modeling of EIS data using equivalent circuit theory is not a feasible solution for analysis of data. The reason is, there exists more than one combination of electrical elements that can give the same response. It is very difficult to conclude which combination of the elements in the circuit is accurate with respect to the electrochemical cell.

Hence mechanistic modeling of EIS data is a motivating option to extract information about the processes happening on the surface of the specimen. Equivalent circuit models could still be used in parallel with mechanistic model to represent the electrochemical cell and to enhance the understanding of the reader. In the following section, an introduction about the calculation of impedance in different situations (for e.g. charge transfer and diffusion control) is given briefly:

Background

EIS data is collected by applying a small AC current or voltage signal to the specimen. The response to the applied AC current would be an AC voltage signal with a phase difference. The response signal is the change in the potential or voltage at which the process was occurring when the system is unperturbed by the input signal. This

change in the potential is called overvoltage, and the impedance for the electrochemical cell is calculated from the overvoltage and input AC current as follows:

$$Z_{total} = \frac{\eta_{total}}{i} \tag{3-7}$$

where, Z_{total} is the total impedance in ohms, $i = I\sin(\omega t)$ is the applied AC current in *A,* η_{total} is the total overvoltage response from the different processes happening in the system in *V*.

For a simple circuit mentioned in Figure 2, the total overvoltage response is the voltage drop across the R component in the circuit. Hence the impedance calculation becomes very simple. But for a complicated electrochemical cell where there is more than one process happening (for e.g. charge transfer and diffusion control), impedance calculation becomes difficult. The impedance for the electrochemical system with charge transfer process and diffusion in finite boundary layer can be given as

$$Z_{total} = \frac{\eta_{total}}{i} = \frac{\eta_{d,\delta.,r} + \eta_t}{i} \tag{3-8}$$

where $\eta_{d,\delta,r}$ is the overvoltage response due to the diffusion or the mass transfer of the reactants through the boundary layer, in *V* and η_t is the overvoltage response in *v*, due to the charge transfer process happening in the system.

Researchers have developed expressions to calculate the overvoltage response in different situations. The equations derived by various researchers, that can be used to calculate the impedance in a system with different processes are given in the following:

Charge transfer overvoltage

Charge transfer over voltage arises when there is a charge transfer step (reaction involving electron transfer) involved in the mechanism, that is, equation (2-5) or (2-6) is the rate determining step in the mechanism during the flow of current. This charge transfer reaction has a certain speed and the speed of the reaction depends on the temperature in the system, the kind of reaction, the concentration of the reaction species, and the potential or the current that is applied.

The relationship between the charge transfer overvoltage when a sinusoidal current of small amplitude is given as an input was derived by Gerischer and Mehl as follows (Gerischer and Mehl, 1955):

$$\eta_t = \frac{I\sin(\omega t)}{L_D - \frac{ab}{b^2 + C_H^2\omega^2} + \frac{aC_H\omega}{b^2 + C_H^2\omega^2}\,j} \tag{3-9}$$

where, j = imaginary component = $\sqrt{-1}$.

The details of equation are given in Appendix A.

It can be seen from equation (3-9) that the overvoltage response in a charge-transfer controlled process is dependent on the frequency and has a phase shift with respect to the input current signal.

Figure 3 shows the shape of a Nyquist plot when the process is pure charge transfer controlled. A simple electrochemical cell with a pure charge transfer process can be modeled with simplest and the most common cell model called Randles cell. Figure 4 shows the equivalent circuit for Randles cell. RE is the reference electrode and WE is the working electrode. The circuit includes a solution resistance, a double layer capacitance

and a charge transfer resistance. The double layer capacitance is in parallel to the impedance due to charge transfer reaction. Nyquist plot for Randles cell looks exactly the same as is shown in Figure 3.

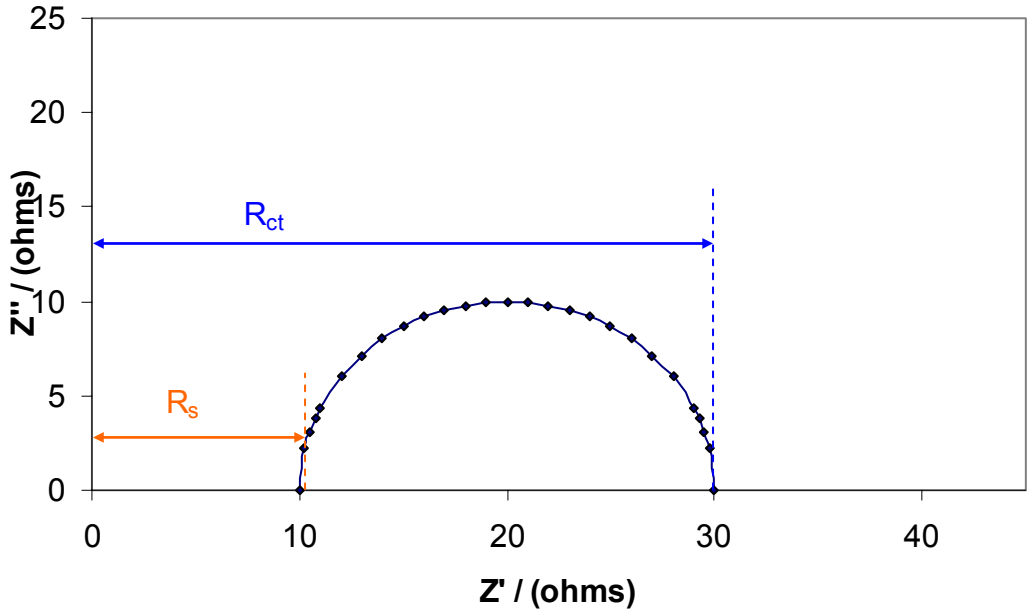

Figure 3. Shape of a Nyquist plot in pure charge transfer controlled situation.

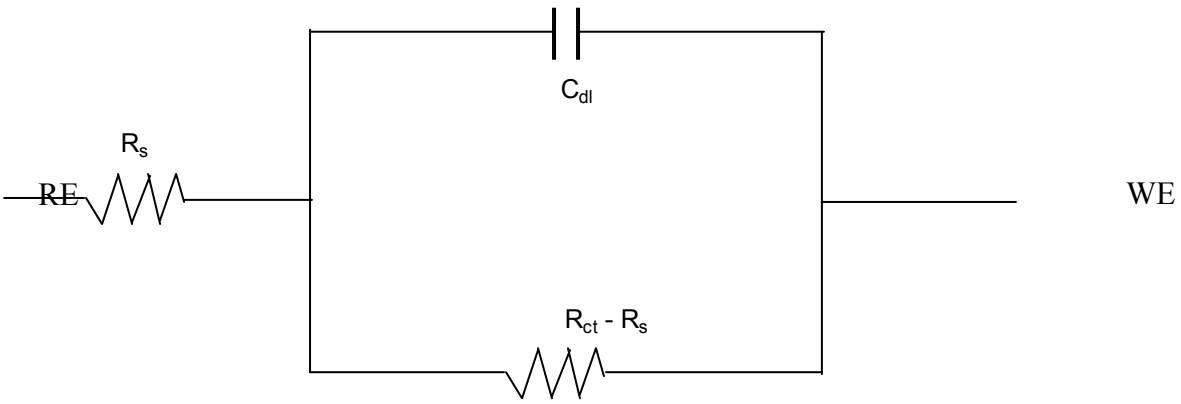

Figure 4. Equivalent circuit for Randles cell.

In the Figure 3, the point where the curve meets the X-axis at the high frequency is the solution resistance (R_s) and the point where the curve meets the X-axis at the low frequency region is the charge transfer resistance (R_{ct}) (if the tail end of the curve meets the X-axis). The difference between these resistances (R_{ct} - R_s) is called "polarization resistance" from the EIS method, and this also could be used to calculate the corrosion rate. The details of the calculation of corrosion rate from the linear polarization measurement technique is given in Appendix B.

Diffusion overvoltage

When the supply of the reactants or the removal of the corrosion products at the surface of the metal is the rate determining step, diffusion overvoltage comes into the picture. In other words, when the diffusion of the reactants or the products from the surface of the metal is the rate limiting step, the overvoltage response to the input current is called diffusion overvoltage.

The relationship between the overvoltage and the input current in a diffusion limitation through infinite boundary layer situation was given by Warburg and is known as Warburg's impedance, as follows (Warburg, 1899):

$$\eta_d = \frac{RT}{n^2F^2}\frac{v^2}{\sqrt{\omega}\,\bar{c}\sqrt{D_{H^+}}} I\sin(\omega t - \frac{\pi}{4}) \qquad (3\text{-}10)$$

where, η_d is the over voltage response in v when the diffusion or the mass transfer of the reactants through infinite boundary layer is limiting step, R is the universal gas constant in joule/mole-K, T is temperature in K, n is the number of equivalents exchanged (n = 1 for hydrogen ion reduction), F is the Faraday's constant (F = 96,490 coulombs/equivalent), v is the viscosity of the solution in kg/m-s, $\bar{c}$ is the bulk concentration of H^+ in the solution in moles/lit (can be determined from the pH value of the solution), D_{H^+} is the diffusivity of H^+ ions in the solution in m^2/s (diffusivity of H^+ ions through the film on to the metal surface if a surface film is present).

In a diffusion controlled situation, there is a phase shift of 45^o between overvoltage and current. This results in a Nyquist plot which is a straight line inclined at 45^o. Figure 5 shows the shape of a Nyquist plot when the process in the system is a perfect mass transfer or diffusion controlled situation. The polarization resistance, which is the difference of charge transfer resistance and the solution resistance, is infinity because the Nyquist plot is a straight line with 45^o inclination to the horizontal. The curve (Nyquist plot) is no longer a semi circle. The change in the process from charge transfer to mass transfer or diffusion controlled can be understood by seeing the change

in the shape of the Nyquist plots. Figure 6 and Figure 7 show the change in the shape of the Nyquist plot from pure charge transfer control (Figure 3) to pure mass transfer control (Figure 5) (lifting of the tail of the plot).

Figure 8 shows the equivalent circuit that can be used to model the pure mass transfer controlled situation. The resistance that is parallel to the double layer capacitance in Figure 8 is represented by a 'W' (Warburg impedance). The Nyquist plot for the circuit in Figure 8 is shown in Figure 5. For a mixed diffusion and charge transfer control situation, the equivalent circuit in between the working and reference electrodes, shown in Figure 9 could be used to model the situation. The Nyquist plot for a mixed control look similar to the Nyquist plots shown in Figure 6 and Figure 7(for a process that is changing from charge transfer control o diffusion control).

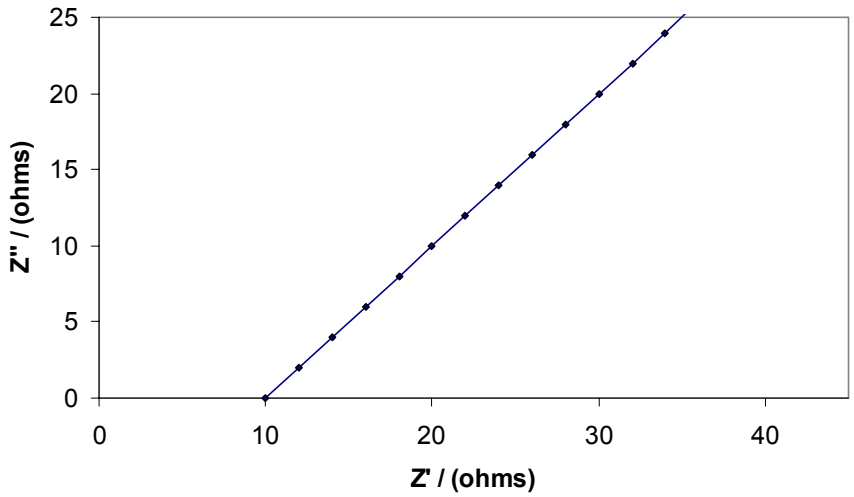

Figure 5. Shape of a Nyquist plot when the process is strictly mass transfer or diffusion controlled.

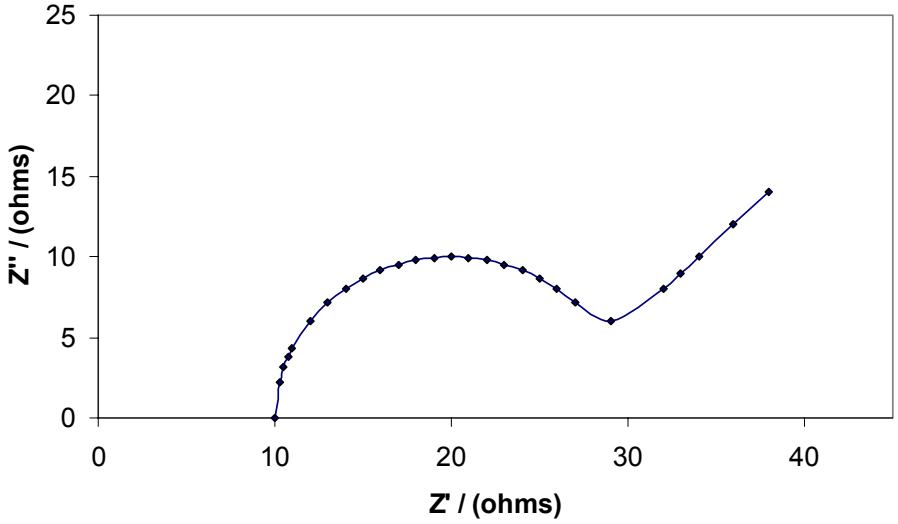

Figure 6. Shape of the Nyquist plot when the process is changing from charge transfer control to diffusion control.

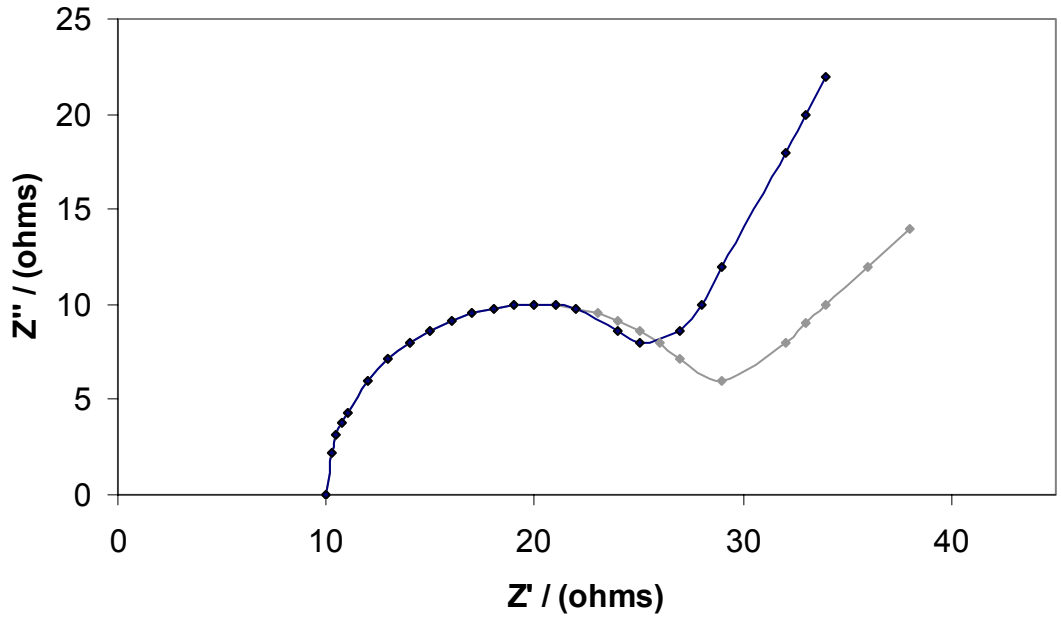

Figure 7. Shape of the Nyquist plot when the process is changing from charge transfer control to diffusion control. The gray line in the plot is Figure 6.

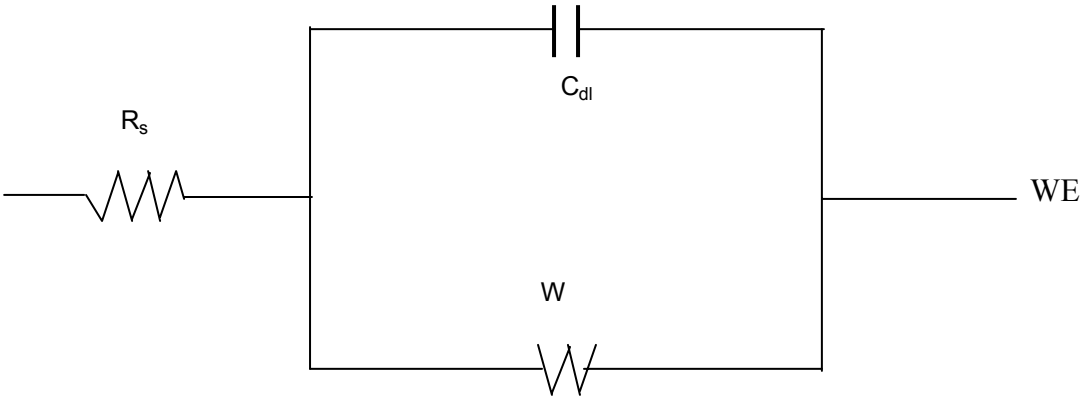

Figure 8. Equivalent circuit for a pure diffusion controlled situation.

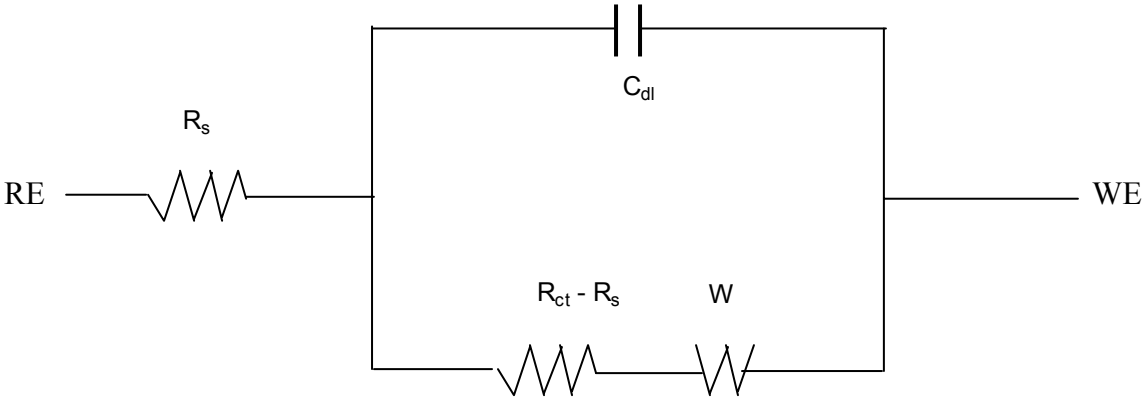

Figure 9. Equivalent circuit for a mixed diffusion and charge transfer control. The Nyquist plot for this kind of situation is shown in Figure 10.

However, Warburg's impedance was derived assuming an infinite boundary layer thickness meaning stagnant conditions, which are rarely encountered in oil and gas fields. Therefore, a more appropriate relationship between the diffusion overvoltage with a finite thickness boundary layer due to turbulent flow condition was derived by Sluyters *et al* as follows (Sluyters *et al.,* 1970):

$$\eta_{d,\delta} = \frac{RT}{n^2F^2}\frac{1-i}{[H^+]_{bulk}\sqrt{2\omega D_{H^+}}}\tanh\left[\delta\sqrt{\frac{i\omega}{D_{H^+}}}\right]I\sin\omega t \qquad (3\text{-}11)$$

where, $\eta_{d,\delta}$ is the over voltage response in v when the diffusion or the mass transfer of the reactants through a finite boundary layer is the limiting step and δ is the thickness of mass transfer boundary layer in *m.*

As the boundary layer thickness *'δ'* in the equation (3-11) increases, the '$\eta_{d,\delta}$' increases, increasing the impedance. It can be seen in Figure 10 that increasing the boundary layer thickness increases the diameter of the semi-circle located at the tail end of the Nyquist plot in the figure, which in turn increases the impedance. Further increase in the boundary layer thickness results in the shape of Nyquist plots shown in Figure 7. The shape of the Nyquist plot for an infinite boundary layer thickness is the same as the one shown in Figure 8 for a pure mass transfer control case as the impedance becomes Warburg impedance (diffusion through infinitely thick boundary layer).

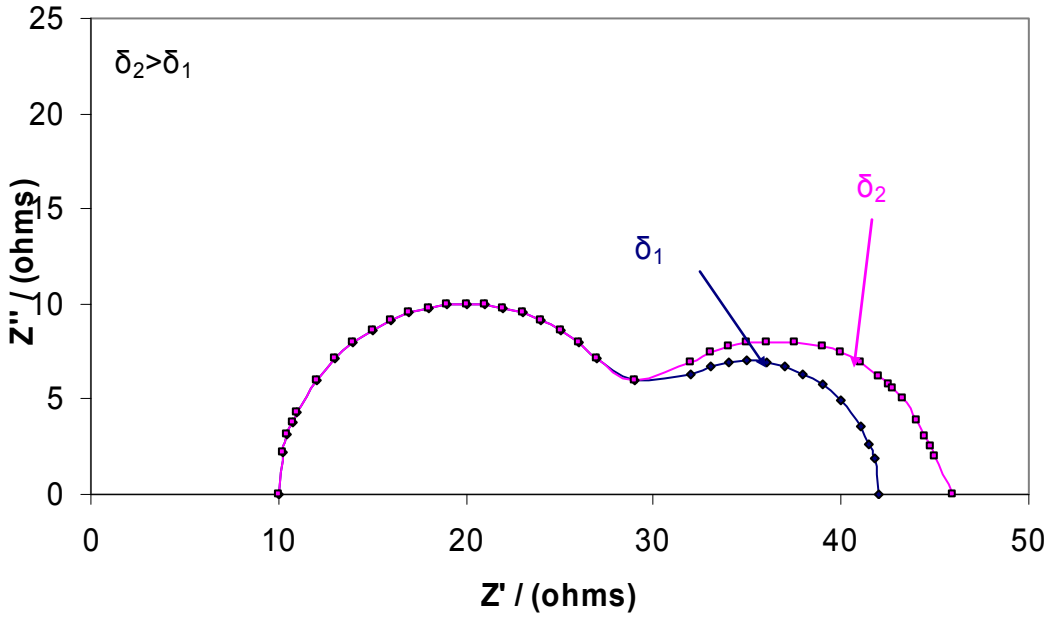

Figure 10. Effect of boundary layer thickness on the shape of Nyquist plot in a combined charge and mass transfer controlled situation.

Reaction Overvoltage

Reaction overvoltage is the voltage response obtained when there exists a slow chemical reaction or when a chemical reaction is the rate determining step. In the case of CO_2 corrosion, the slow hydration of CO_2 as in equation (2-1) is the slowest and hence the rate determining reaction and contributes partly to the limiting current. Previous studies by other researchers (Vetter, 1961) and (Nesic *et al.,* 1995) suggest that the superposition of diffusion and chemical reaction controlled limiting currents was legitimate. Therefore the influence of diffusion in infinite boundary layer and rate determining reaction were treated simultaneously and the over voltage response with both diffusion and reaction when an alternating sinusoidal current is given as an input was given by Vetter as follows (Vetter, 1961):

$$\eta_r = \frac{RT}{n^2F^2}\frac{v^2}{\sqrt{\omega}[H^+]_{bulk}\sqrt{2D_{H^+}}}\sqrt{\frac{\sqrt{1+\left(\frac{k}{\omega}\right)^2}+\frac{k}{\omega}}{1+\left(\frac{k}{\omega}\right)^2}}I\sin\omega t - \frac{RT}{n^2F^2}\frac{v^2}{\sqrt{\omega}[H^+]_{bulk}\sqrt{2D_{H^+}}}\sqrt{\frac{\sqrt{1+\left(\frac{k}{\omega}\right)^2}-\frac{k}{\omega}}{1+\left(\frac{k}{\omega}\right)^2}}I\cos\omega t \quad (3\text{-}12)$$

where, η_r is the over voltage response in V when there is both diffusion and limiting reaction in the infinite boundary layer.

This kind of response is very difficult to analyze using equivalent circuits because it cannot be modeled using simple circuits. The system could be modeled using complicated circuits but more than one combination of the electrical elements gives the same response and it is difficult to decide which combination of the elements is accurate with respect to the electrochemical cell that was used to generate the EIS data.

The details of the equation (3-12) are given in Appendix A.

The diffusion overvoltage with rate limiting reaction has a varying phase shift with respect to the AC current input but it is a strong function of the frequency. However, equation (3-12) was derived for the case of infinite boundary layer condition, because Vetter assumed that the fluid was well mixed and in equilibrium, which was a good assumption for laminar and stagnant flow conditions. Whereas for a high enough velocity and turbulent flow condition, one needs to assume that the edge of the mass transfer boundary layer is the point where the fluid is well mixed. Therefore, the diffusion

overvoltage involving the rate determining reaction in turbulent flow conditions was derived by Lee as follows (Lee, 2003):

$$\eta_{d,\delta,r} = \frac{RT}{n^2 F^2 \left[H^+\right]_{bulk} D_{H^+} \lambda} \tanh(\lambda\delta)\, I \sin \omega t \qquad (3\text{-}13)$$

where, $\eta_{d,\delta,r}$ is the diffusion overvoltage response involving chemical reaction and turbulent flow conditions in *V,* and $\lambda = \sqrt{\frac{i\omega + k}{D_{H^+}}}$

Details of equation (3-13) are given in Appendix A.

Hence this expression can be used to model the shape of the Nyquist plots acquired from electrochemical systems and the data can be used to analyze the processes happening on the surface of the specimen in the system.

Based on the above mentioned theory, a mechanistic model was developed to analyze the EIS data from the experiments where trace amounts of H_2S is present. The model is developed in such a way that the critical surface parameters like the thickness of the surface film, porosity of the film and the mass transfer boundary layer on the surface of the metal are included. A detailed description of the model used to analyze the experimental EIS data is explained in the following section.

Mechanistic EIS Model

Figure 11 shows the schematic of a metal surface section with a film of porosity ε and a concentration boundary layer in the liquid phase. The turbulence is the main mechanism for mass transfer in the other part of the hydrodynamic boundary layer whose thickness is δ_{hb} while molecular diffusion is the major transport mechanism through the mass transfer boundary layer (of thickness δ_{mbl}) and the porous film (of thickness δ_f). The

corrosion rate of the metal depends primarily on the thickness of the film, δ_f, and, more importantly, the porosity of the film as this is the main barrier for mass transfer of species.

Hence a parameter called effective permeability is derived that takes into account the thickness of the film δ_f, the effective diffusion coefficient $D_{H+,}$ and the porosity of the film ε.

Effective Permeability of the species

The resistance to mass transfer in a layer of fluid whose thickness is δ and diffusivity is *D,* is *(δ/D)*. Total resistance for mass transfer of the corrosive species through the mass transfer boundary layer and the porous film is calculated by assuming that the individual resistances in series,

$$\frac{D}{\delta} = \frac{1}{\frac{\delta_{mbl}}{D_{H^+}^{mbl}} + \frac{\delta_f}{D_{H^+}^{f}}} \tag{3-14}$$

where δ_{mbl} is the mass transfer boundary layer thickness.

The mass transfer boundary layer thickness is calculated by the following relationship (Levich, 1962):

$$\delta_{mbl} = \delta_{hbl} * \left(\frac{\nu}{D_{H^+}} \right)^{-0.33} \tag{3-15}$$

where δ_{hbl} is the turbulent boundary layer thickness, calculated according to the following relationship (Davies, 1972):

$$\delta_{hbl} = 25 * \mathrm{Re}^{-\frac{7}{8}} * d \tag{3-16}$$

where *Re* is the Reynolds number of the flow in the pipe and *d* is the hydraulic diameter of the pipe.

The diffusion coefficient of corrosive species is calculated as follows:

$$D_{H^+}^{f} = D_{H^+}^{mbl} * \frac{T}{273} * \frac{0.001002}{\nu} * \varepsilon^{1.5} \tag{3-17}$$

Where ν is the kinematic viscosity.

The total impedance response of the system can be calculated using the equations (3-8), (3-9), (3-14), (3-15), (3-16) and (3-17). Hence by changing the film thickness, film porosity and diffusivity, experimental Nyquist plots can be fitted by a model curve which ultimately reveals the information about the required parameters.(porosity and film thickness).

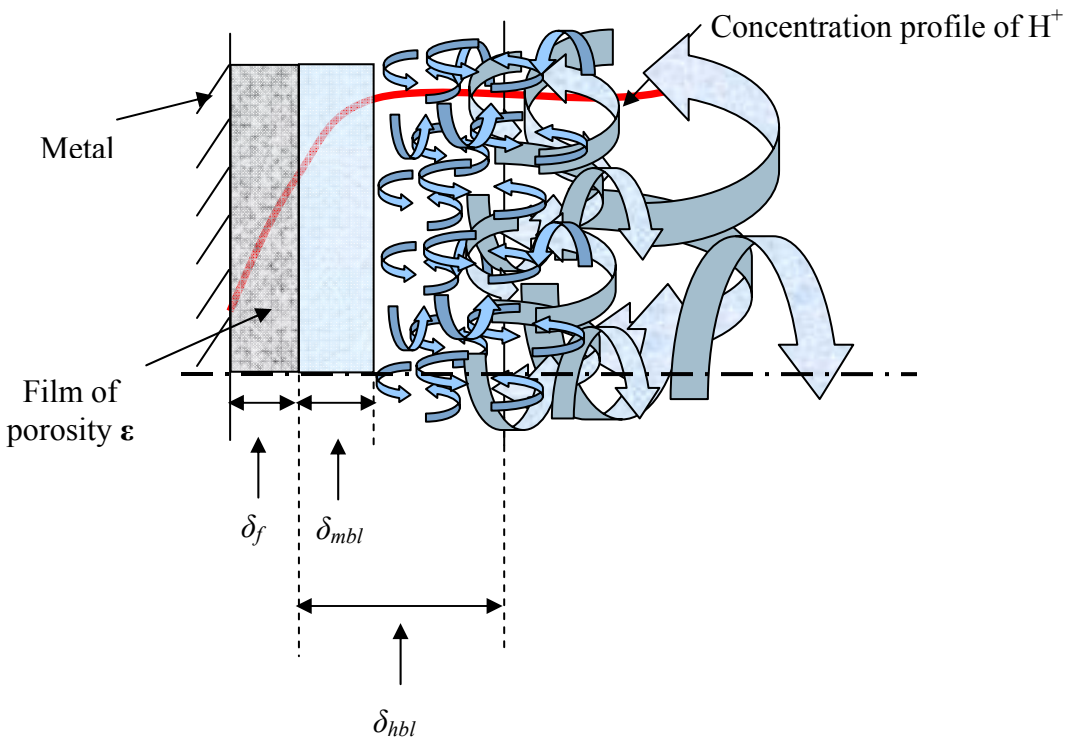

Figure 11. Surface of the metal in the solution with a porous film formed.

Double layer capacitance

In the electrochemical impedance spectrum (Nyquist Plot), the semi-circle at high frequency contains information about the electrical double layer. The behavior of the double layer that is formed on the surface of the metal due to the separation of the ions in the solution when the metal is immersed in the solution, is similar to that of a capacitor. Even though it is similar to a capacitor, it cannot be modeled using an ideal capacitor because the behavior of the double layer is not exactly the same as an ideal capacitor. Hence a constant phase element (CPE) that is in parallel to the total impedance is used to model the double layer.

The so-called CPE is an element whose impedance value is a function of the frequency, and its phase is independent of the frequency. Its impedance is defined as:

$$Z_{CPE} = \frac{1}{Y_o}(j\omega)^{-n} \tag{3-18}$$

Where Y_o = modulus of CPE (magnitude of the capacitance), ω = angular frequency = $2\pi f$ n = phase of CPE (it varies from 0 to 1).

The reason that CPE is used instead of capacitors when one analyses the impedance spectra is that most impedance curves measured in experiments are not ideal semi-circles, but are depressed due to various factors like heterogeneous surface roughness and the non-uniform distribution of current density on the surface. The depression degree depends on the phase *n* of the CPE. The capacitance of CPE depends on various factors like the electrode potential, the concentration of the ions, surface impurities, etc. The value of the capacitance that was used during the modeling of data was 0.0002 to 0.0006 F. (Ma *et al.,* 1999)

Therefore CPE is the only element in the model that is not mechanistic, and it is assumed to be in a parallel configuration with total impedance Z_{total}. Figure 12 shows the equivalent circuit for the model.

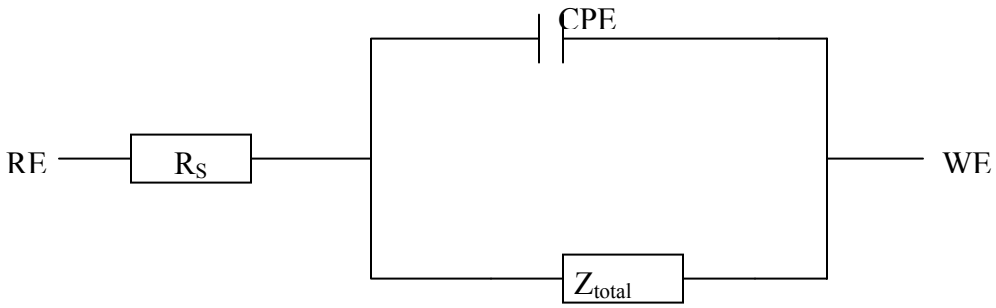

Figure 12. Equivalent Circuit for the EIS model.

where WE = Working Electrode, RE = Reference Electrode, R_S = Solution resistance acquired from the experiment, CPE = Constant Phase Element, Z_{total} = Impedance calculated from the model from the equation (3-8).

Hence the model is used to analyze the experimental data to extract meaningful information about the important parameters like diffusivity, film thickness and film porosity. A detailed discussion about the modeling of experimental data is given in chapter 7.

CHAPTER 4: RESEARCH OBJECTIVES AND TEST MATRIX

Research objectives

Based on the previous research, the principal question that need to be answered is:

1. What are the effects of film formation on the mechanisms of CO_2 corrosion when there is a small concentration of H_2S in the system?

Test Matrix

The following test matrix was defined to answer the above questions.

Table 1. Test Matrix for research

Steel Type	AISI 1018
Composition of the Solution	1% NaCl
Temperature, T (°C)	60
Partial Pressure of CO_2, P_{CO2} (bar)	7.7
Velocity of the liquid (m/s)	1
pH	6.0 , 6.6
Fe^{++} concentration (ppm)	5 - 25
Concentration of H_2S (ppm)	10 - 100

The above set of experiments was designed to see the effect of different saturation values of iron carbonate and iron sulfide on the general and localized corrosion rates of the metal in a CO_2 and H_2S environment in the above mentioned conditions. The saturation values of iron carbonate and iron sulfide are strongly dependent on the concentration of dissolved iron in the solution and hence could be changed by changing the concentration of dissolved iron in the system.

It was reported that there exists a "gray zone" where the probability of occurrence of localized corrosion is very high when the saturation values of the iron carbonate range from 0.3 to 3 (Nesic and Sun, 2003). So, it was decided to target the gray zone conditions and investigate corrosion rates of the metal under these conditions.

The chemical composition of the AISI 1018 steel (according to wt %) used for all the experiments is shown in

Table 2 .

Table 2. Chemical Composition of AISI 1018 steel (balance Fe)

Al	As	B	C	Ca	Co	Cr	Cu	Mn	Mo	Nb
0.0032	0.005	0.0003	0.050	0.004	0.006	0.042	0.019	1.32	0.031	0.046
Ni	P	Pb	S	Sb	Si	Sn	Ta	Ti	V	Zr
0.039	0.013	0.020	0.002	0.011	0.31	0.001	0.007	0.002	0.055	0.003

CHAPTER 5: EXPERIMENTAL SETUP AND PROCEDURE

Experimental setup and procedure

The experiments were done in a large scale (2000 lit capacity) hastelloy H_2S flow loop to simulate real field conditions. Figure 13 shows the process and instrumentation diagram of the flow loop.

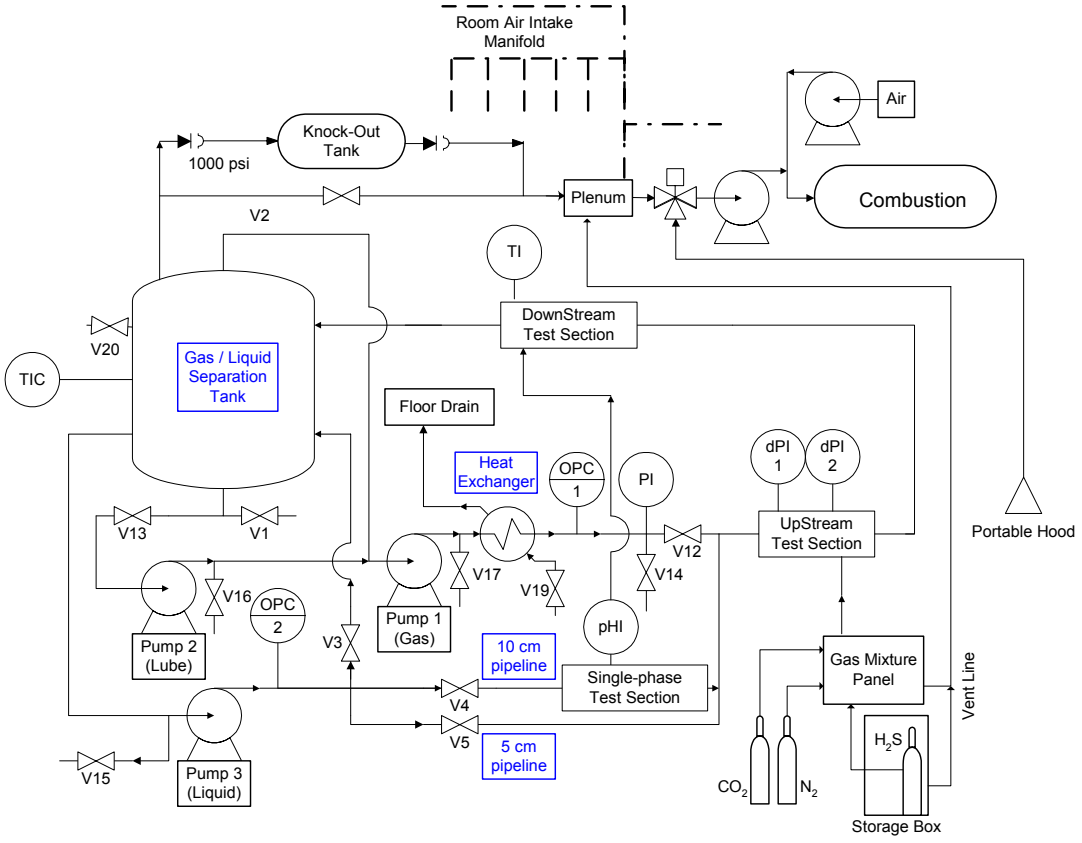

Figure 13. PID of the hastelloy H_2S experimental flow loop.

A picture of the original flow loop is given in Figure 14. The flow loop consists of both single phase and multiphase test sections, but only the results from the single phase

test section were used in this work. All pipe sections in the flow loop are insulated to minimize heat loss due to the temperature gradient between the liquid in the pipe and the ambient environment. Details about the flow loop are given elsewhere (Brown and Schubert, 2002).

Figure 14. Hastelloy H_2S flow loop.

Electrochemical measurements were taken using a concentric ring probe, and weight loss measurements were taken using three small button coupons of 1.12 cm^2 area embedded in a Teflon holder. Figure 15 is a photo of the concentric ring probe used in the experiments.

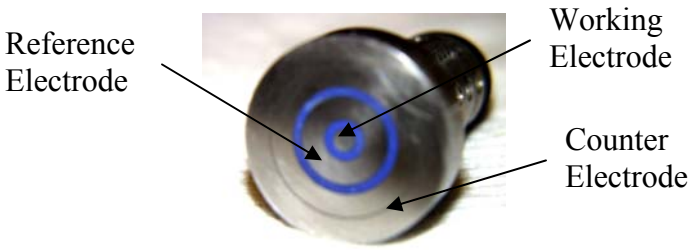

Figure 15. Concentric ring probe used for taking electrochemical measurements during the experiments.

The center pin and the first ring in the electrode are made of AISI 1018, and the outer ring is made up of stainless steel. Electrochemical measurements were taken using the center pin as the reference electrode and the first ring as the working electrode. The outer ring in the probe is used as the counter electrode. The area of the working electrode is 0.95 cm^2.

Figure 16 shows the picture of the arrangement of the AISI 1018 coupons embedded in the Teflon holder.

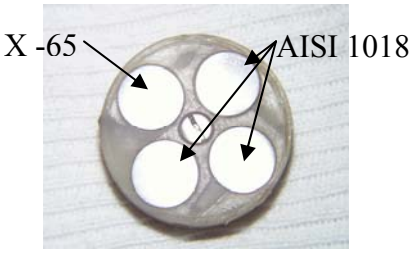

Figure 16. Arrangement of the metal button coupons in the Teflon holder used to take weight loss measurements.

Three coupons made out of AISI 1018 steel are embedded into a Teflon holder and the holder is fastened to a probe using a nylon screw to avoid electrical contact and then the probe is flush mounted into the system. Prior to immersion, the carbon steel specimen surfaces were polished with 240, 400 and 600 grit silicon carbide (SiC) paper, rinsed with alcohol and degreased using acetone to avoid the presence of any foreign materials or corrosion products from the previous experiments.

The tank was initially filled with 1000 liters of distilled water with NaCl added to make the solution 1% wt. The solution was then heated to 60 ^{0}C and purged with 7.7 bar CO_2 gas. After the solution was deoxygenated, H_2S gas was purged at a very low rate and the concentration of H_2S is measured continuously. After the desired concentration of H_2S was achieved, the purging of H_2S was stopped and the pH value of the solution was adjusted from the equilibrium pH value of 3.98 to the desired value (6.0 or 6.6) by adding a calculated amount of deoxygenated sodium bicarbonate solution. The desired concentration of Fe^{2+} was attained by adding a calculated amount of deoxygenated ferrous chloride salt ($FeCl_2.4H_2O$) solution. Then the concentric ring probe was flush mounted into the system to acquire electrochemical measurements, and the weight loss

probe was inserted to measure the weight of the metal lost during the experiment. The length of the experiment varied from 4 to 30 days depending on the experimental conditions. During the experiments, all parameters, such as the pH value, Fe^{+2} concentration, H_2S concentration, temperature, and pressure were regularly monitored.

Electrochemical corrosion measurements were performed by using a potentiostat connected to a PC. Measurements were started with corrosion potential and other electrochemical measurements taken after the corrosion potential was stabilized (after about 20 minutes). Corrosion rates were measured by using the linear polarization resistance (LPR) method. The sample with iron carbonate or iron sulfide scale was observed using Scanning Electron Microscopy (SEM).

Corrosion Rate Measurement Techniques

The electrochemical impedance spectroscopy results were analyzed using the mechanistic model mentioned in the previous section. The electrochemical methods used to measure the corrosion rate are as follows:

- The linear polarization resistance (LPR) technique is used to measure the *in-situ* corrosion rate. The metal sample was polarized ±5 mV around the corrosion potential during the LPR measurement. The resistance for the current flow measured using the LPR technique was the total resistance, and the solution resistance needed to be compensated by, using the electrochemical impedance spectroscopy (EIS) technique. The equations used to calculate the corrosion rate using LPR are shown in Appendix B.

- In the electrochemical impedance technique, the metal electrode is polarized with an AC current signal of very small amplitude (5 amp) and the technique

measures the total impedance in the system which is a function of the input AC current signal and the output voltage response of the system for the input current. The total impedance is a complex value, and the plot of total impedance is called a Nyquist plot (an example of Nyquist plot is shown in Figure 5).

An experimental uncertainty analysis due to the inherent error in the instrument was done. (Uncertainty analysis is explained in detail in Appendix C).

CHAPTER 6: EXPERIMENTAL RESULTS AND DISCUSSION

Experimental results obtained are presented below in the following manner (SS_{FeS} is the integrated average of the bulk saturation value for iron sulfide and SS_{FeCO3} is the integrated average of the bulk saturation value for iron carbonate):

Experiment 1. concentration of Fe^{2+} = 10 ppm, concentration of H_2S = 25 ppm, pH value = 6.0**,** SS_{FeS} = 34, SS_{FeCO3} = 10.

Experiment 2. concentration of Fe^{2+} = 8 ppm, concentration of H_2S = 100 ppm, pH value = 6.6**,** SS_{FeS} = 500, SS_{FeCO3} = 37.

Experiment 3. concentration of Fe^{2+} = 15 ppm, concentration of H_2S = 20 ppm, pH value = 6.0, SS_{FeS} = 7, SS_{FeCO3} = 9.

Experiment 4. concentration of Fe^{2+} = 5 ppm, concentration of H_2S = 10 ppm, pH value = 6.0, SS_{FeS} = 3, SS_{FeCO3} = 6.

Experiment 1

The corrosion rate as measured by the linear polarization method (LPR) with time and as calculated by the weight loss (WL) method is shown in Figure 17. From the figure it can be observed that the corrosion rate from the LPR method decreased for a period of 18 hours from the beginning of the experiment and stabilized at about 0.1 mm/yr. Weight loss measurement (WL) was done at the end of four days and the value was averaged for four day period. The integrated average value of the corrosion rates from LPR method with time was found (explained in Appendix B) and the value was 0.21 mm/yr which is higher than the value from weight loss method. Figure 18 shows the change in the shape of Nyquist plots as a function of time for this experimental condition. It can be observed

from the figure that the processes happening on the surface of the metal change from charge transfer control (shape of the Nyquist plot being a near semicircle) to diffusion or mass transfer control (shape of the Nyquist plot being a near 45^{o} straight line). From these observations, it can be confirmed that there is film growth that reduced the corrosion rate considerably, and this fact can also be backed up by a porous film of 38 μm thickness found on the surface of the specimen at the end of the experiment as shown in Figure 19.

The saturation values for FeS and $FeCO_3$ during this experiment were calculated to be 34 and 10 respectively. The precipitated film found on the specimen due to supersaturation of iron carbonate and sulfide was porous and the porosity of the film was calculated to be 75 % (porosity calculations are explained in detail in Appendix B). LPR measurements were taken for three days and weight loss measurement was done after a four day period. The deviation of last data point in the LPR measurements was attributed to the failure of the probe.

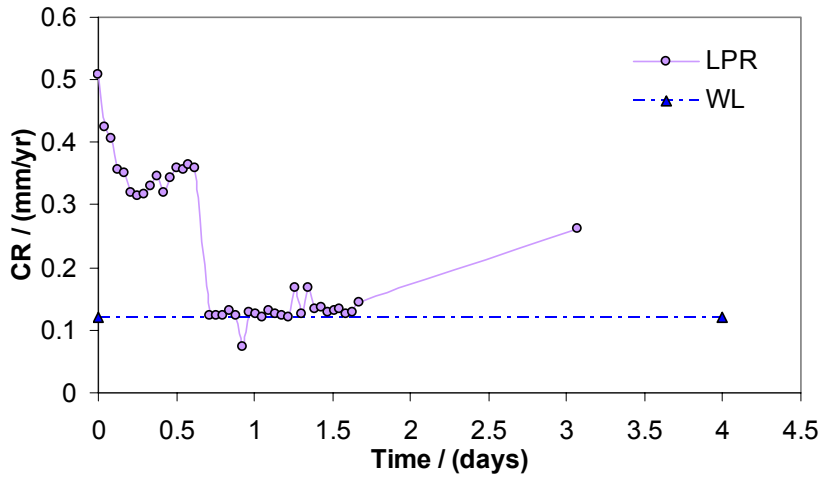

Figure 17. Experiment 1- Corrosion rates with time obtained from linear polarization resistance (LPR) and weight loss (WL) measurements (10 ppm Fe^{2+}, 25 ppm H_2S, pH = 6.0, SS_{FeS} = 34, SS_{FeCO3} = 10). Nyquist plots with time for this experiment are shown in Figure 18 and the cross section of the film obtained is shown in Figure 19.

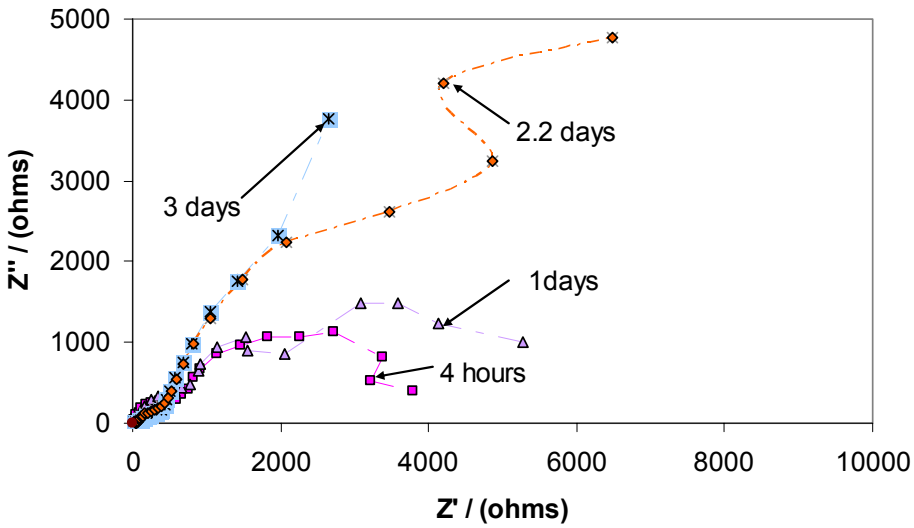

Figure 18. Experiment 1- Change in the shape of Nyquist plot with time (10 ppm Fe^{2+}, 25 ppm H_2S, pH = 6.0, SS_{FeS} = 34, SS_{FeCO3} = 10). Corrosion rates with time for this experiment are shown in Figure 17 and cross section of the film obtained is shown in Figure 19.

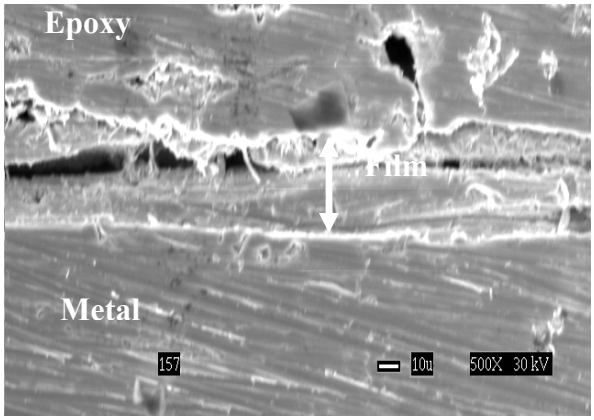

Figure 19. Experiment 1 - SEM cross section of the film obtained. (10 ppm Fe^{2+}, 25 ppm H_2S, pH = 6.0, SS_{FeS} = 34, SS_{FeCO3} = 10). Corrosion rates with time for this experiment are shown in Figure 17 and Nyquist plots with time are shown in Figure 18.

Experiment 2

The corrosion rate as measured by the linear polarization method with time (LPR) and calculated by the weight loss method is shown in Figure 20. From the figure it can be observed that the corrosion rate from the LPR method decreased for a period of two days from the beginning of the experiment and stabilized at about 0.16 mm/yr. Corrosion rate from weight loss method was calculated to be 0.16 mm/yr. Weight loss measurement (WL) was done at the end of four days, and the value is averaged for the four day period. The integrated average of the corrosion rate from LPR method was 0.15 mm/yr which is very close to that obtained from weight loss method.

Figure 21 shows the change of the shape of Nyquist plots with time for this experiment. It can be observed from the figure that the processes happening on the surface of the metal change from charge transfer control to diffusion or mass transfer

control which is the same mechanism happened during the experiment 1. In this case the process is completely mass transfer controlled because of the shape of the final Nyquist plot (inclined nearly at 45^{o}). Also it can be confirmed that there is a film growth that reduced the corrosion rate considerably, and this fact is backed up by the SEM image of the cross section of the specimen showing a film of 30 μm thickness.

The saturation values for FeS and $FeCO_3$ during this experiment were 500 and 37, respectively. Even though the saturation of FeS was very high when compared to that in experiment 1, the final film thickness was nearly the same and the porosity of the film in this case was calculated to be 77 %. Weight loss measurement was done after a four day period but LPR measurements were continued to observe the trend of corrosion rate. The corrosion rate was decreasing slightly after four days from the beginning of the experiment. Hence it was decided to continue future experiments for a longer period of time to get more information on the trend of corrosion rate.

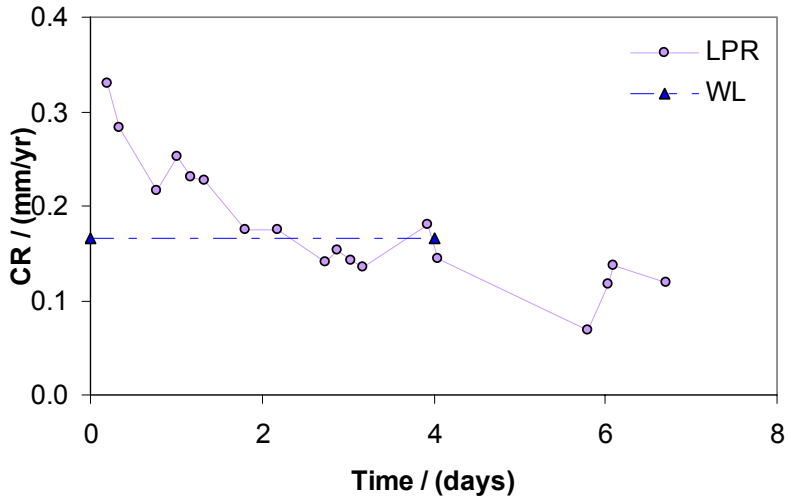

Figure 20. Experiment 2 - Corrosion rates with time obtained from linear polarization resistance (LPR) and weight loss (WL) measurements (8 ppm Fe^{2+}, 100 ppm H_2S, pH = 6.6, $SS_{FeS} = 500$, $SS_{FeCO3} = 37$). Nyquist plots with time for this experiment are shown in Figure 21 and the cross section of the film obtained is shown in Figure 22.

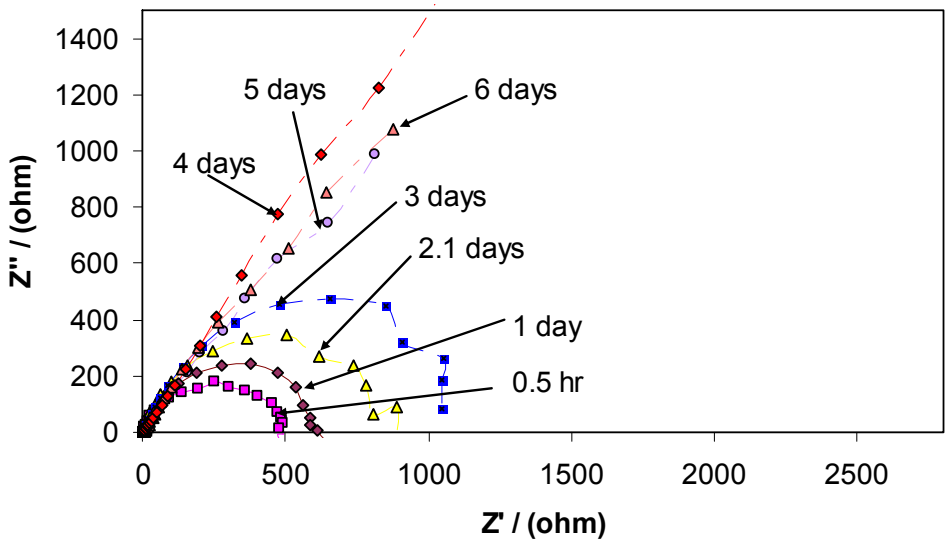

Figure 21. Experiment 2 - Change in the shape of Nyquist plot with time (8 ppm Fe^{2+}, 100 ppm H_2S, pH = 6.6, $SS_{FeS} = 500$, $SS_{FeCO3} = 37$). Corrosion rates with time for this experiment are shown in Figure 20 and cross section of the film obtained is shown in Figure 22.

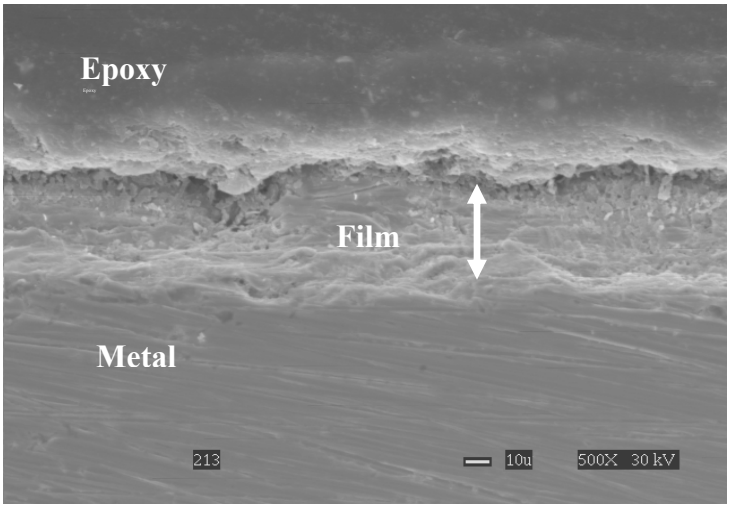

Figure 22. Experiment 2 – SEM cross section of the film obtained (8 ppm Fe^{2+}, 100 ppm H_2S, pH = 6.6, SS_{FeS} = 500, SS_{FeCO3} = 37). Corrosion rates with time for this experiment are shown in Figure 20 and Nyquist plots with time are shown in Figure 21.

Experiment 3

The corrosion rates of the sample as measured by the linear polarization method (LPR) and calculated by the weight loss method is shown in Figure 23. From the figure it can be observed that the corrosion rate from the LPR method increased initially but then decreased for a period of five days from the beginning of the experiment and stabilized at about 0.05 mm/yr for the rest of the experiment. Weight loss measurement (WL) was done at the end of thirty days, and the value was averaged for thirty day period. The integrated average of the corrosion rate from the LPR method was 0.07 mm/yr which was nearly equal to that obtained from weight loss method (0.05 mm/yr). Figure 24 shows the shape of Nyquist plot as a function of time for this experiment for two days and Figure 25 shows the shape of Nyquist plots as a function of time for this experimental condition

from two to thirty days. The inset rectangle in Figure 25 is Figure 24. The axes had to be expanded to fit the experimental data in the plot. It can be observed from Figure 24 and Figure 25 that the processes happening on the surface of the metal change from charge transfer control to diffusion or mass transfer control (lifting of the tail part of the Nyquist plot gradually) similar to the mechanism happened in experiment 1 and experiment 2. It can be confirmed for this experiment that there was a film that reduced the corrosion rate considerably by acting as a diffusion barrier, and this fact can also be backed up by the SEM image of the cross section of the specimen that was used in the experiment, shown in Figure 26.

The saturation values for FeS and $FeCO_3$ during this experiment were 7 and 9 respectively. The saturation values for iron carbonate and iron sulfide for this experiment fall near to the "gray zone" defined for the occurrence of localized attack but no localized corrosion was seen on the particular material used for this experiment. The time that was required for film formation in this experiment was longer than the time taken for film formation in the previous experiments, as observed from the decrease in corrosion rate measured by LPR method, because of the lower values of saturation of iron carbonate and iron sulfide. The final corrosion rate from LPR measurement for this experiment was nearly an order of magnitude less than that obtained for the experiments 1 and 2. The porosity of the 65 μm thick film formed during the experiment (shown in Figure 26) was calculated to be 65 %. LPR measurements were taken for 34 days and weight loss measurement was taken after 30 days from the beginning of the experiment.

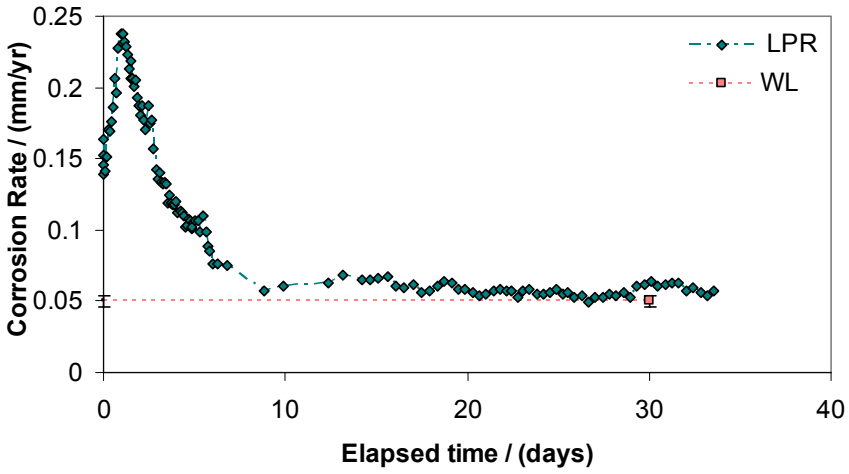

Figure 23. Experiment 3 - Corrosion rates with time obtained from linear polarization resistance (LPR) and weight loss (WL) measurements (15 ppm Fe^{2+}, 20 ppm H_2S, pH = 6.0, $SS_{FeS} = 7$, $SS_{FeCO3} = 9$). Nyquist plots with time for this experiment are shown in Figure 24 and Figure 25 and the cross section of the film obtained is shown in Figure 26.

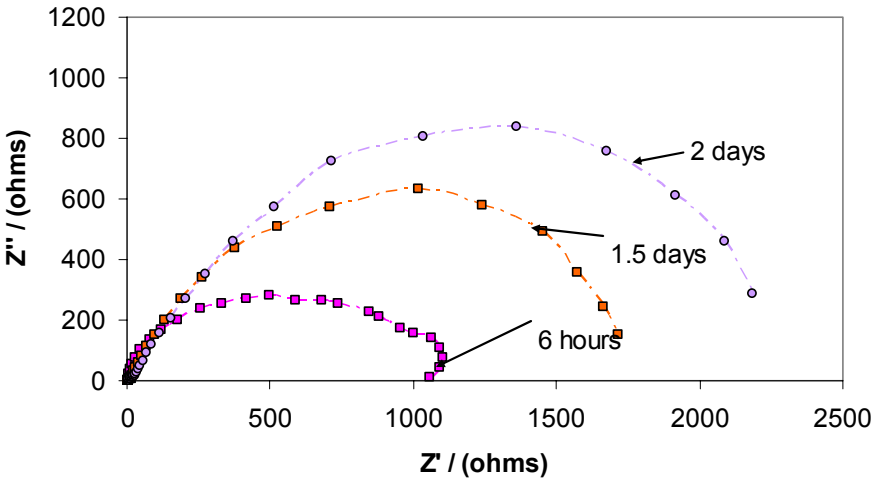

Figure 24. Experiment 3 - Change in the shape of Nyquist plot with time from 0 to 2 days (15 ppm Fe^{2+}, 20 ppm H_2S, pH = 6.0, $SS_{FeS} = 7$, $SS_{FeCO3} = 9$). Corrosion rates with time for this experiment are shown in Figure 23 and cross section of the film obtained is shown in Figure 26.

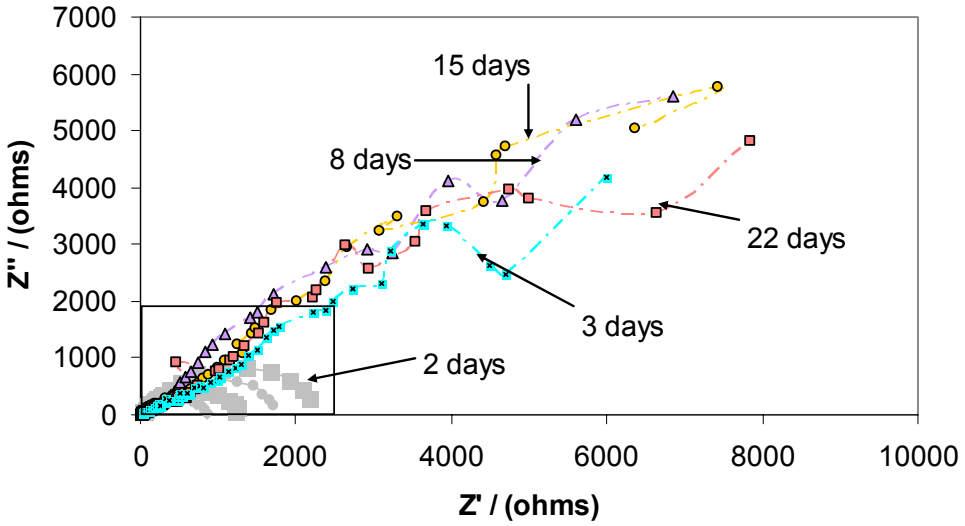

Figure 25. Experiment 3 - Change in the shape of Nyquist plot with time for from 2 - 30 days (15 ppm Fe^{2+}, 20 ppm H_2S, pH = 6.0, $SS_{FeS} = 7$, $SS_{FeCO3} = 9$). Insert picture is Figure 24. Expanded axes decreased the size of the picture. Corrosion rates with time for this experiment are shown in Figure 23 and cross section of the film obtained is shown in Figure 26.

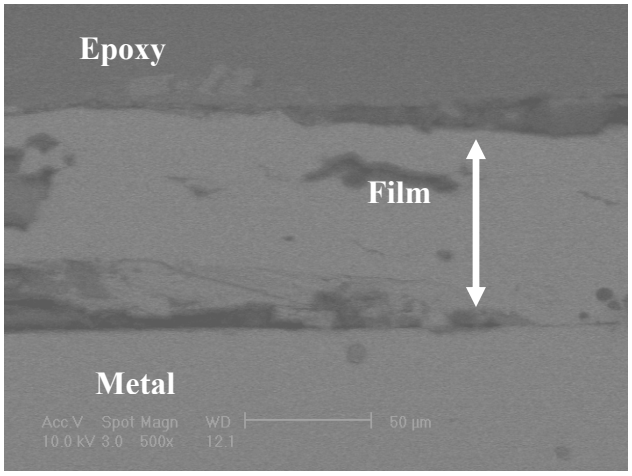

Figure 26. Experiment 3 - SEM cross section of the film obtained (15 ppm Fe^{2+}, 20 ppm H_2S, pH = 6.0, $SS_{FeS} = 7$, $SS_{FeCO3} = 9$). Corrosion rates with time for this experiment are shown in Figure 23 and Nyquist plots with time are shown in Figure 24 and Figure 25.

Experiment 4

The corrosion rates of the sample as measured by the linear polarization method (LPR) and calculated by the weight loss method is shown in Figure 27. From the figure it can be observed that the corrosion rate from the LPR method decreased immediately after one day, remained constant for fifteen days and decreased slightly to 0.008 mm/yr and remained constant for the remaining duration of the experiment. Weight loss measurement (WL) was done at the end of thirty days, and the value was averaged for thirty day period. The integrated average of corrosion rate from the LPR method was 0.012 mm/yr which was less than that obtained from the weight loss method (0.023 mm/yr). Figure 28 shows the shape of Nyquist plots as a function of time for this experiment for thirty day period. From Figure 28, it can be said that the processes happening on the surface of the metal change by the end of experiment to diffusion or mass transfer control (lifting of the tail part of the Nyquist plot) which is the same mechanism happening in all the other experiments in the presence of H_2S. The saturation values for FeS and $FeCO_3$ during this experiment were 3 and 6 respectively which fall in the "gray zone". The final corrosion rate from LPR method was similar to that obtained for experiment 3 and nearly a magnitude less than that obtained for experiments 1 and 2. There was a film of 85 μm thick (as shown in Figure 29) on the surface of the specimen and the porosity of the film as calculated was 80 %. Even though the film was very porous, it was very protective. Length of the experiment was thirty days.

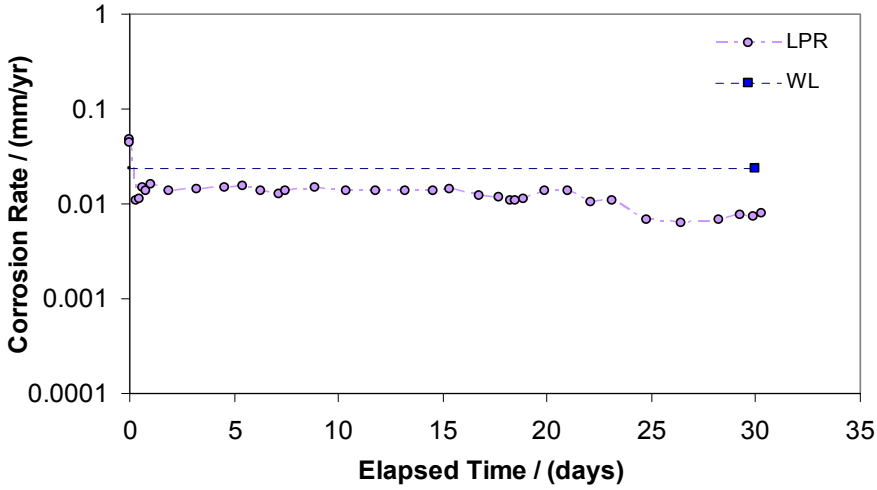

Figure 27. Experiment 4 - Corrosion rates with time obtained from linear polarization resistance (LPR) and weight loss (WL) measurements (5 ppm Fe^{2+}, 10 ppm H_2S, pH = 6.0, $SS_{FeS} = 3$, $SS_{FeCO3} = 6$). Nyquist plots with time for this experiment are shown in Figure 28 and the cross section of the film obtained is shown in Figure 29.

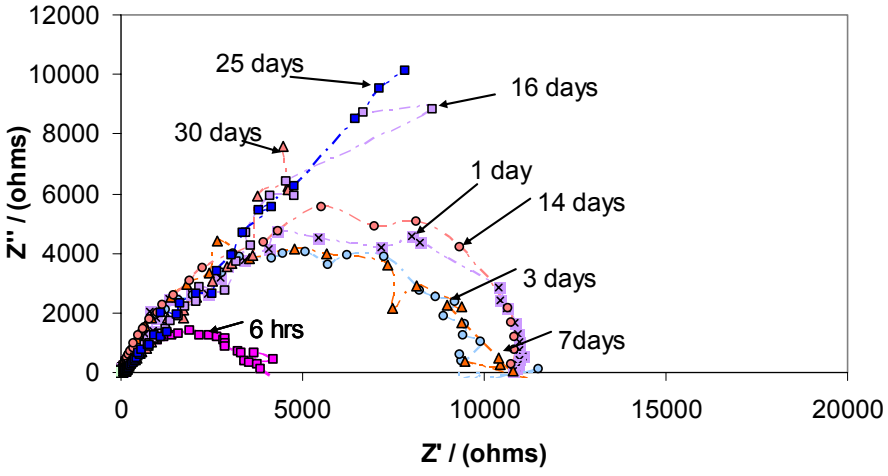

Figure 28. Experiment 4 - Change in the shape of Nyquist plot with time (5 ppm Fe^{2+}, 10 ppm H_2S, pH = 6.0, $SS_{FeS} = 3$, $SS_{FeCO3} = 6$). Corrosion rates with time for this experiment are shown in Figure 27 and cross section of the film obtained is shown in Figure 29.

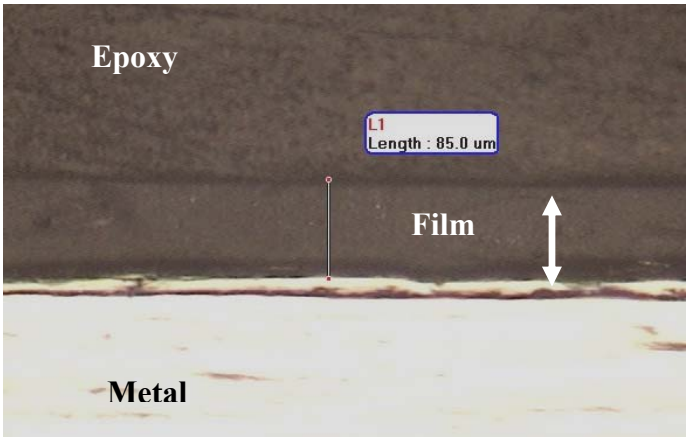

Figure 29. Experiment 4 - Optical microscopy picture of the cross section of the film obtained (5 ppm Fe^{2+}, 10 ppm H_2S, pH = 6.0, $SS_{FeS} = 3$, $SS_{FeCO3} = 6$). Corrosion rates with time for this experiment are shown in Figure 27 and Nyquist plots with time are shown in Figure 28.

In general it was observed in all the experiments for the experimental conditions studied, there was a protective film on the surface of the metal that was acting as a diffusion barrier to the corrosive species and reducing the corrosion rates (corrosion rate < 0.1 mm/yr) regardless of the saturation values of iron carbonate and iron sulfide. Thicker and more porous films were obtained in experiments 3 and 4 where the saturation values of iron carbonate and iron sulfide are near to the "gray zone". The films formed in all the experiments were very protective regardless of their porosity.

The corrosion rates at the temperature, partial pressure of CO_2, pH values and concentrations of iron tested should be at around 7 mm/yr (as predicted by corrosion prediction software MULTICORP V3.0). The initial corrosion rates as measured by LPR method for all the experiments were very less than what they should be in a pure CO_2

environment. This helped us to come to a conclusion that the presence of any amount of H_2S in the system was the reason for the drastic drop in the initial corrosion rate.

Once the results were obtained, an attempt was made to analyze them using the Electrochemical Impedance Spectroscopy model described in Chapter 3 to extract information about the critical parameters in the experiment that influenced the corrosion rate of the metal sample. The analysis of the experimental data is given in the following chapter.

CHAPTER 7: ANALYSIS USING THE EIS MODEL

For each of the four experiments, the Nyquist plots are modeled, and the model curve that fits the experimental data best is shown for each experimental curve. The parameters in the model, effective permeability (D/δ), film thickness (δ_f) and porosity of the film (ε) that led to that best fit are listed for each curve, and in the end, the trend of these parameters are plotted with time for each experiment. The porosity of the film at the beginning of the experiment was assumed to be 1 while modeling (meaning no film is found on the surface of the metal at time = 0) and the calculated value of porosity from the experimental results is based on a 100% $FeCO_3$ film.

Experiment 1

Corrosion rates from LPR and weight loss method for this experiment are shown in Figure 17. Figure 30 through Figure 32 show the comparison of the experimental Nyquist plots with time with that of the curves given by the mode for Experiment 1. Values of the effective permeability, porosity and the thickness of the film which led to the best fit of experimental curve are given for each figure. It can be observed from the change in the shape of Nyquist with time that the corrosion rate for this experiment has decreased with time and reached a constant value after two days. No change in the Nyquist plots was seen after two days. Figure 33 shows the change in porosity and thickness of the film on the surface of the metal with time. Figure 34 shows the trend of effective permeability with time as given by the model and the corrosion rate as measured by LPR method by time. Decrease in the permeability of the corrosive species decreased the corrosion rate and hence the corrosion rate is directly related to the effective

permeability of the species. Figure 35 shows the comparison of film thickness from the model and experiment and Figure 36 shows the comparison of the film porosity as calculated from the experiment (shown in Appendix B) and as given by the model. Figure 19 shows the SEM cross section of the sample that was used during for this experiment.

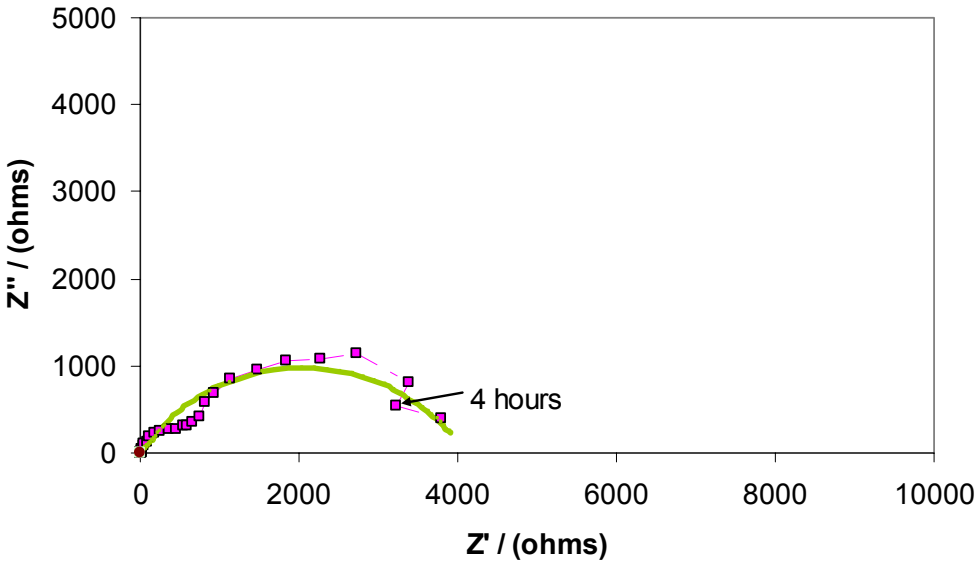

Figure 30. Experiment 1 - Comparison of Nyquist plot (4 hours) from experiment and model (10 ppm Fe^{2+}, 25 ppm H_2S, pH = 6.0, SS_{FeS} = 34, SS_{FeCO3} = 10). Model parameters: $D/\delta = 8.12 \times 10^{-4}$ m/s, δ_f = 5 μm and $\varepsilon = 0.89$. The continuous line is the model curve and the discontinuous one is the experimental curve.

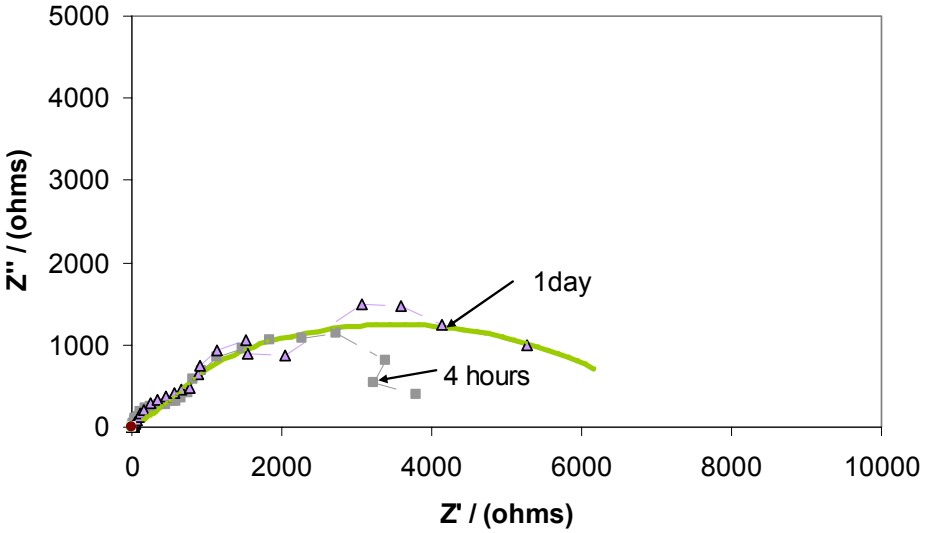

Figure 31. Experiment 1 - Comparison of Nyquist plot (1 day) from experiment and model (10 ppm Fe^{2+}, 25 ppm H_2S, pH = 6.0, SS_{FeS} = 34, SS_{FeCO3} = 10). Model parameters: $D/\delta = 4.8 \times 10^{-4}$ m/s, δ_f = 15 µm and ε = 0.79. The continuous line is the model curve and the discontinuous one is the experimental curve.

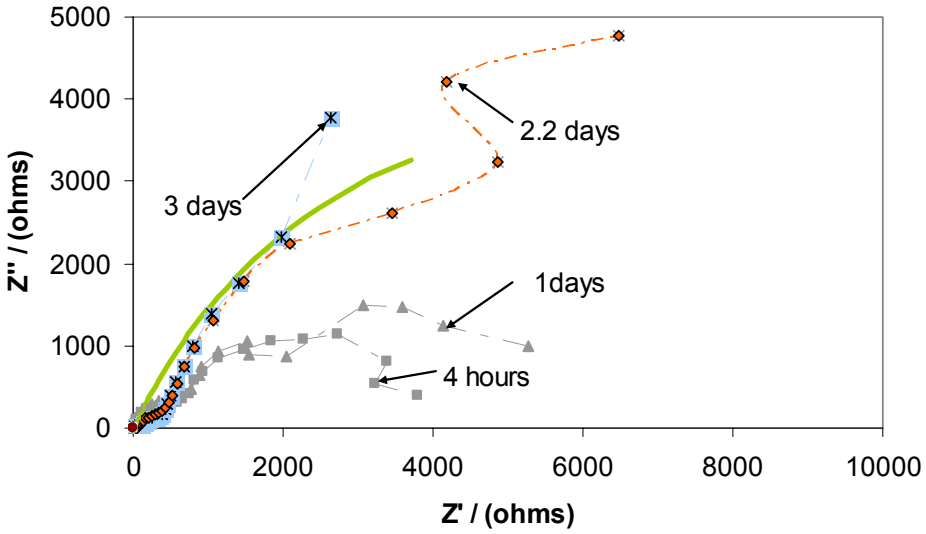

Figure 32. Experiment 1 - Comparison of Nyquist plot (2.2 to 4 days) from experiment and model (10 ppm Fe^{2+}, 25 ppm H_2S, pH = 6.0, SS_{FeS} = 34, SS_{FeCO3} = 10). Model parameters: $D/\delta = 2.03 \times 10^{-4}$ m/s, δ_f = 40 µm and ε = 0.65. The continuous line is the model curve and the discontinuous one is the experimental curve.

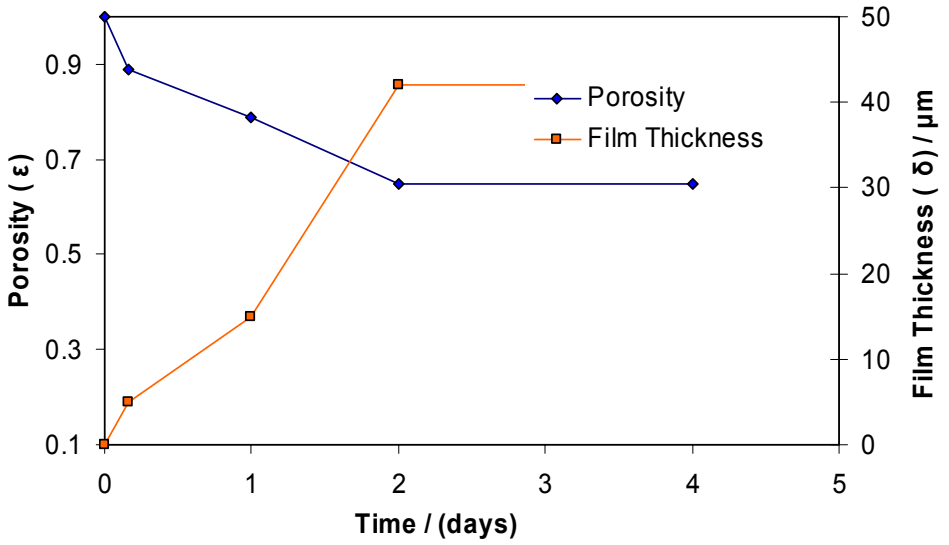

Figure 33. Experiment 1 – Change in porosity and thickness of the film as given by the model (10 ppm Fe^{2+}, 25 ppm H_2S, pH = 6.0, SS_{FeS} = 34, SS_{FeCO3} = 10).

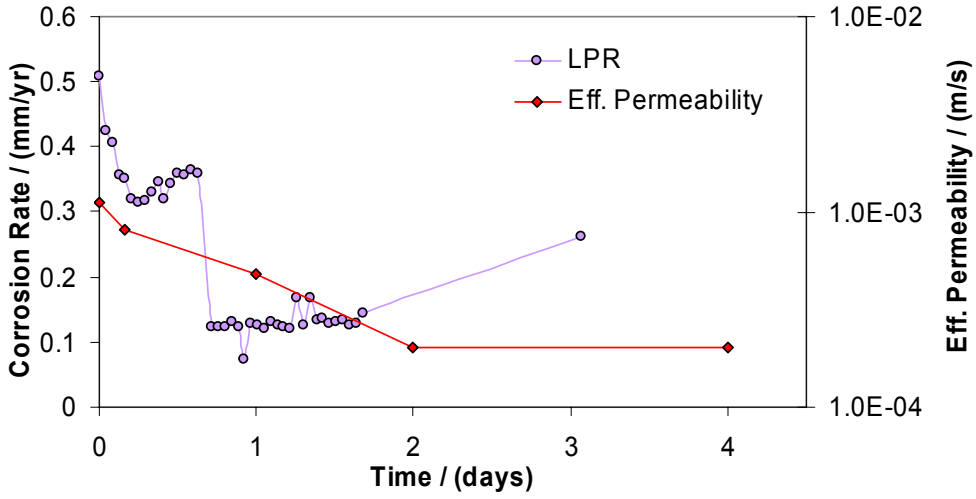

Figure 34. Experiment 1 – Comparison of effective permeability with time as given by the model and corrosion rate with time as given by the LPR method (10 ppm Fe^{2+}, 25 ppm H_2S, pH = 6.0, SS_{FeS} = 34, SS_{FeCO3} = 10).

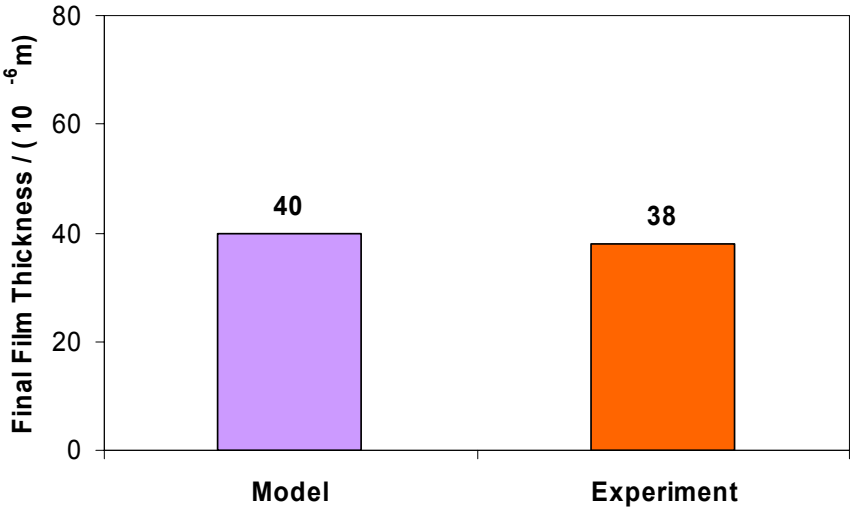

Figure 35. Experiment 1 – Comparison of film thickness as given by the model and the experiment (10 ppm Fe^{2+}, 25 ppm H_2S, pH = 6.0, SS_{FeS} = 34, SS_{FeCO3} = 10). The SEM image of the cross section of the specimen is shown in Figure 19.

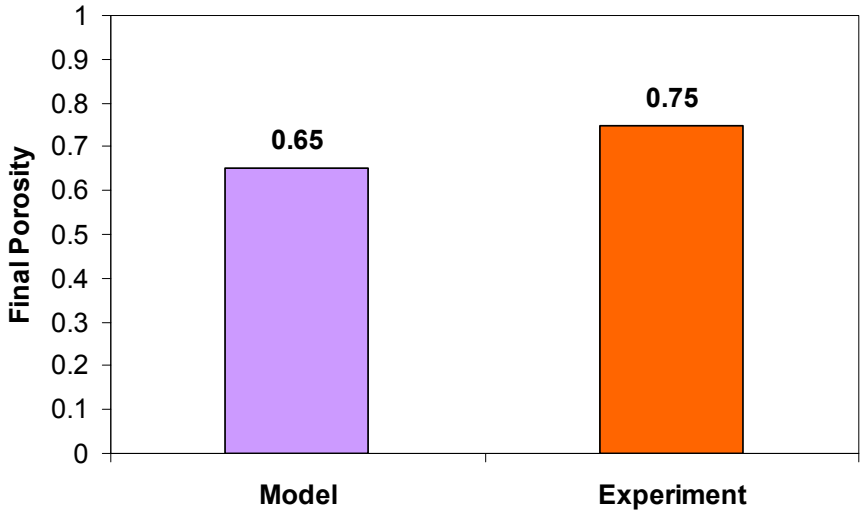

Figure 36. Experiment 1 – Comparison of film porosity as given by the model and calculated from the experiment (10 ppm Fe^{2+}, 25 ppm H_2S, pH = 6.0, SS_{FeS} = 34, SS_{FeCO3} = 10). Porosity of the film is calculated assuming a 100% $FeCO_3$ film.

Experiment 2

Corrosion rates from LPR and weight loss method for this experiment are shown in Figure 20. Figure 37 through Figure 39 show the comparison of the experimental Nyquist plots with time with that of the curves given by the model for Experiment 2. Values of different parameters in the model which led to the best fit of experimental curve are given for these figures. It can be observed that the corrosion rate for this experiment decreased with time and reached a constant value after three days. Figure 40 shows the change in porosity and thickness of the film on the surface of the metal with time as predicted by the model. Figure 41 shows the trend of effective permeability with time as given by the model and the corrosion rate as measured by LPR method with time. Figure 42 shows the comparison of film thickness from the model and experiment and Figure 43 shows the comparison of film porosity as calculated from the experiment and as given by the model. Figure 22 shows the SEM cross section of the sample that was used during for this experiment. It can be observed that the final values of film porosity and film thickness are in good agreement with the values of film thickness and film porosity obtained from the experiment.

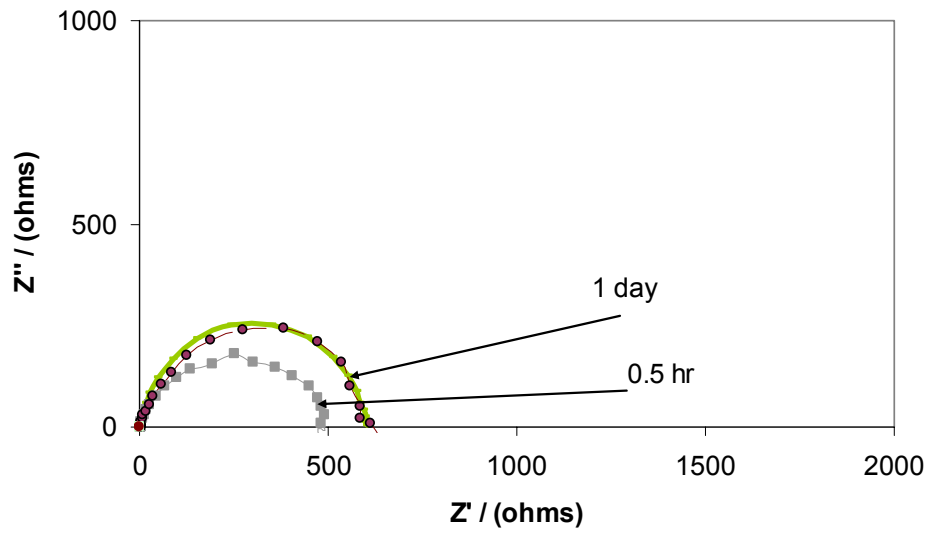

Figure 37. Experiment 2 - Comparison of Nyquist plot (1 day) from experiment and model (8 ppm Fe^{2+}, 100 ppm H_2S, pH = 6.6, SS_{FeS} = 500, SS_{FeCO3} = 37). Model parameters: $D/\delta = 1.12 \times 10^{-3}$ m/s, δ_f = 0 μm and ε = 0.99. The continuous line is the model curve and the discontinuous one is the experimental curve.

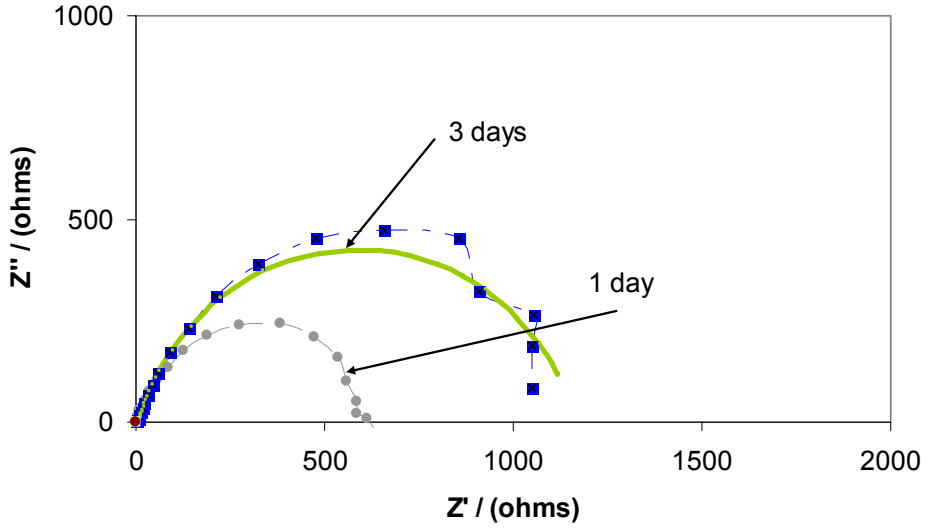

Figure 38. Experiment 2 - Comparison of Nyquist plot (3 days) from experiment and model (8 ppm Fe^{2+}, 100 ppm H_2S, pH = 6.6, SS_{FeS} = 500, SS_{FeCO3} = 37). Model parameters: $D/\delta = 7.71 \times 10^{-4}$ m/s, δ_f = 10 μm and ε = 0.89. The continuous line is the model curve and the discontinuous one is the experimental curve.

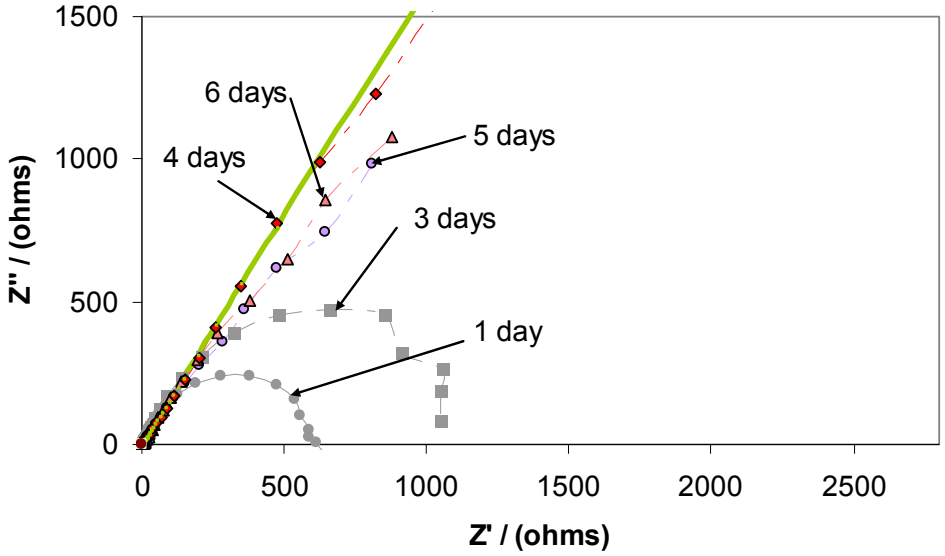

Figure 39. Experiment 2 - Comparison of Nyquist plot (4 days) from experiment and model (8 ppm Fe^{2+}, 100 ppm H_2S, pH = 6.6, $SS_{FeS} = 500$, $SS_{FeCO3} = 37$). Model parameters: $D/\delta = 3.93 \times 10^{-4}$ m/s, $\delta_f = 35$ µm and $\varepsilon = 0.69$. The continuous line is the model curve and the discontinuous one is the experimental curve.

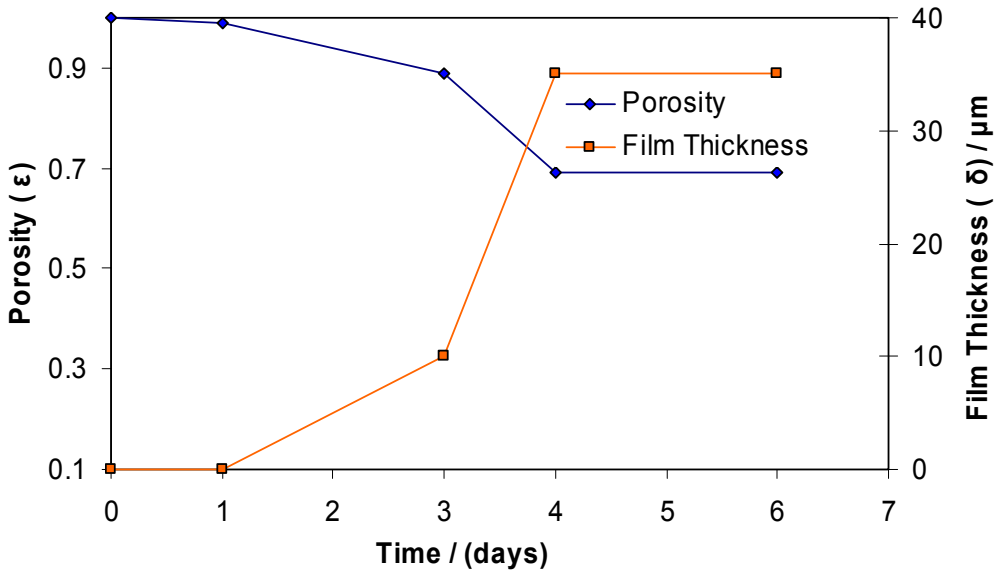

Figure 40. Experiment 2 – Change in porosity and thickness of the film as given by the model (8 ppm Fe^{2+}, 100 ppm H_2S, pH = 6.6, $SS_{FeS} = 500$, $SS_{FeCO3} = 37$).

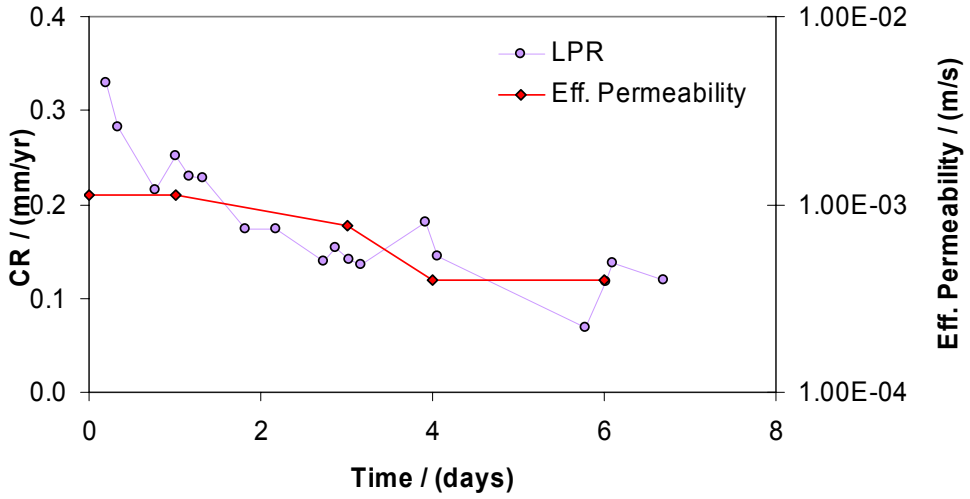

Figure 41. Experiment 2 – Comparison of effective permeability with time as given by the model and corrosion rate with time as given by the LPR method (8 ppm Fe^{2+}, 100 ppm H_2S, pH = 6.6, $SS_{FeS} = 500$, $SS_{FeCO3} = 37$).

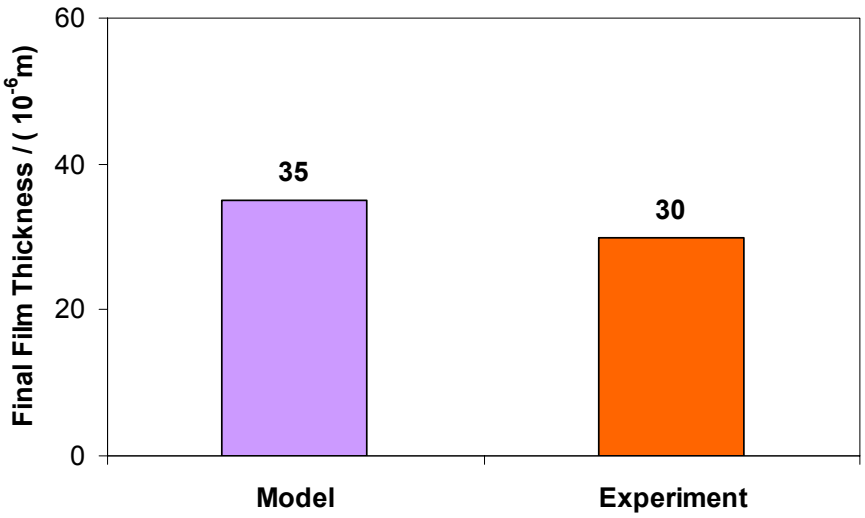

Figure 42. Experiment 2 – Comparison of film thickness as given by the model and from the experiment (8 ppm Fe^{2+}, 100 ppm H_2S, pH = 6.6, $SS_{FeS} = 500$, $SS_{FeCO3} = 37$). The SEM image of the cross section of the specimen is shown in Figure 22.

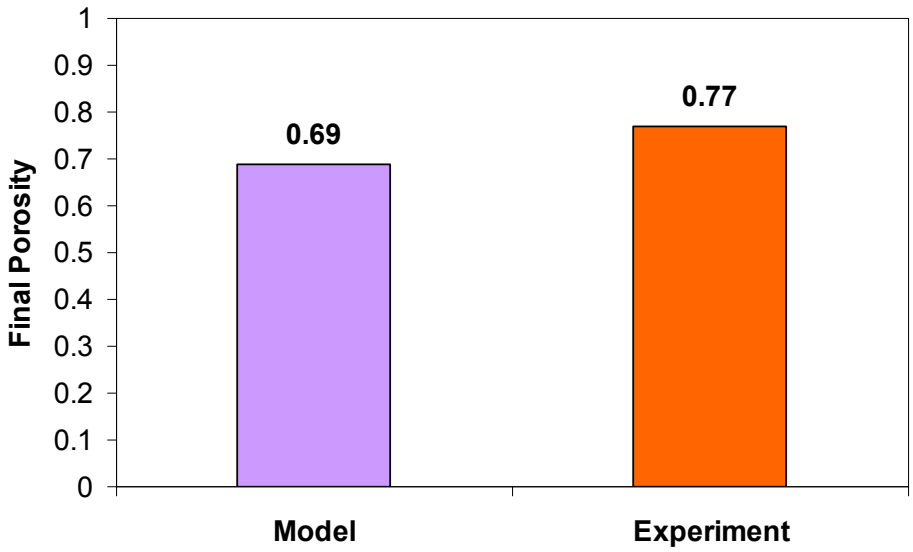

Figure 43. Experiment 2 - Comparison of film porosity as given by the model and calculated from the experiment (8 ppm Fe^{2+}, 100 ppm H_2S, pH = 6.6, SS_{FeS} = 500, SS_{FeCO3} = 37). Porosity of the film is calculated assuming a 100% $FeCO_3$ film.

Experiment 3

Corrosion rates from LPR and weight loss method for this experiment are shown in Figure 23. Figure 44 through Figure 47 show the comparison of the experimental Nyquist plots with time for Experiment 3 with that of the curves given by the model. It can be observed from the figures that the corrosion rate for this experiment decreased with time and reached a constant value after five days. The change of shape of Nyquist plots with time for this experiment was similar to the change during experiment 1 and experiment 2. Figure 48 shows the change in porosity and thickness of the film on the

surface of the metal with time. Figure 49 shows the trend of effective permeability with time as given by the model and the corrosion rate as measured by LPR method with time.

Figure 50 shows the comparison of film thickness from the model and experiment and Figure 51 shows the comparison of film porosity as calculated from the experiment and as given by the model. In this case also the final values of film thickness and film porosity from the experiment and model are in good agreement with each other.

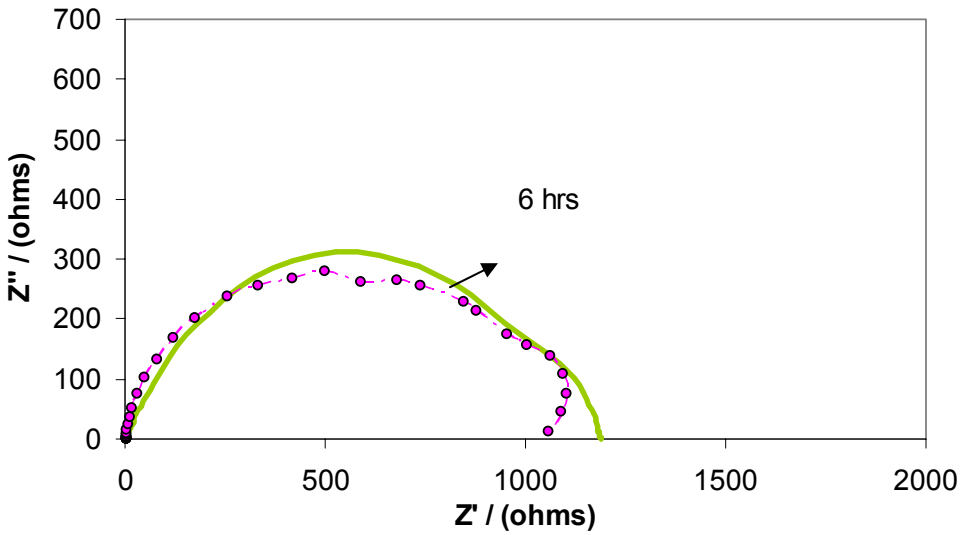

Figure 44. Experiment 3 - Comparison of Nyquist plot (6 hours) from experiment and model (15 ppm Fe^{2+}, 20 ppm H_2S, pH = 6.0, $SS_{FeS} = 7$, $SS_{FeCO3} = 9$). Model parameters: $D/\delta = 1.12 \times 10^{-3}$ m/s, $\delta_f = 0$ μm and $\varepsilon = 0.99$. The continuous line is the model curve and the discontinuous one is the experimental curve.

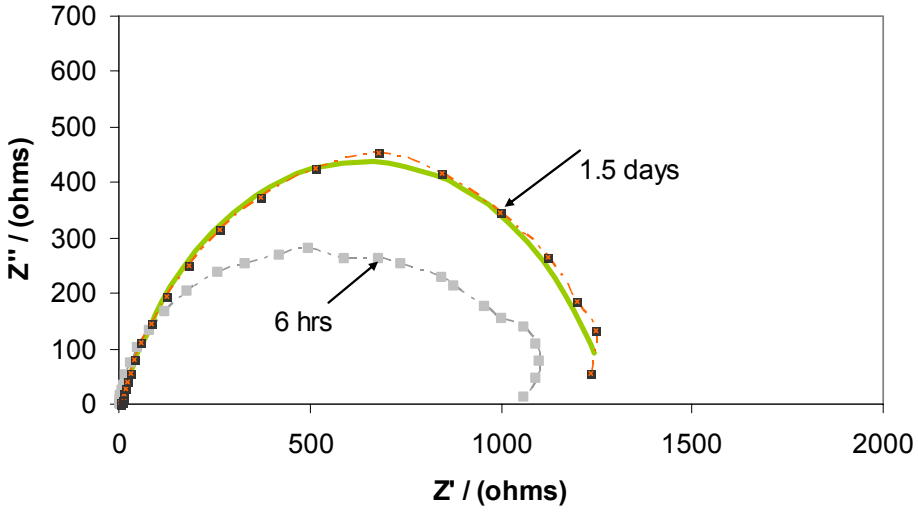

Figure 45. Experiment 3 - Comparison of Nyquist plot (1.5 days) from experiment and model (15 ppm Fe^{2+}, 20 ppm H_2S, pH = 6.0, $SS_{FeS} = 7$, $SS_{FeCO3} = 9$). Model parameters: $D/\delta = 8.1 \times 10^{-4}$ m/s, $\delta_f = 5$ µm and $\varepsilon = 0.89$. The continuous line is the model curve and the discontinuous one is the experimental curve.

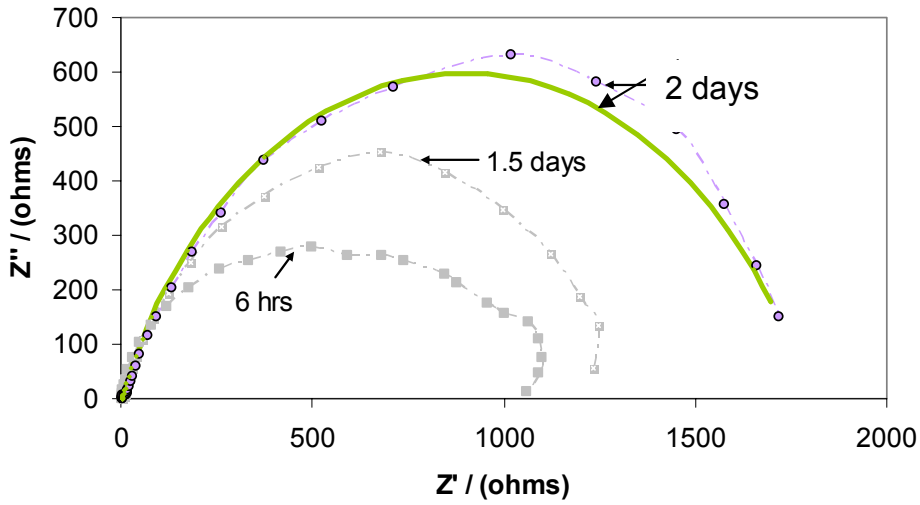

Figure 46. Experiment 3 - Comparison of Nyquist plot (47 hours) from experiment and model (15 ppm Fe^{2+}, 20 ppm H_2S, pH = 6.0, $SS_{FeS} = 7$, $SS_{FeCO3} = 9$). Model parameters: $D/\delta = 5.19 \times 10^{-4}$ m/s, $\delta_f = 15$ µm and $\varepsilon = 0.89$. The continuous line is the model curve and the discontinuous one is the experimental curve.

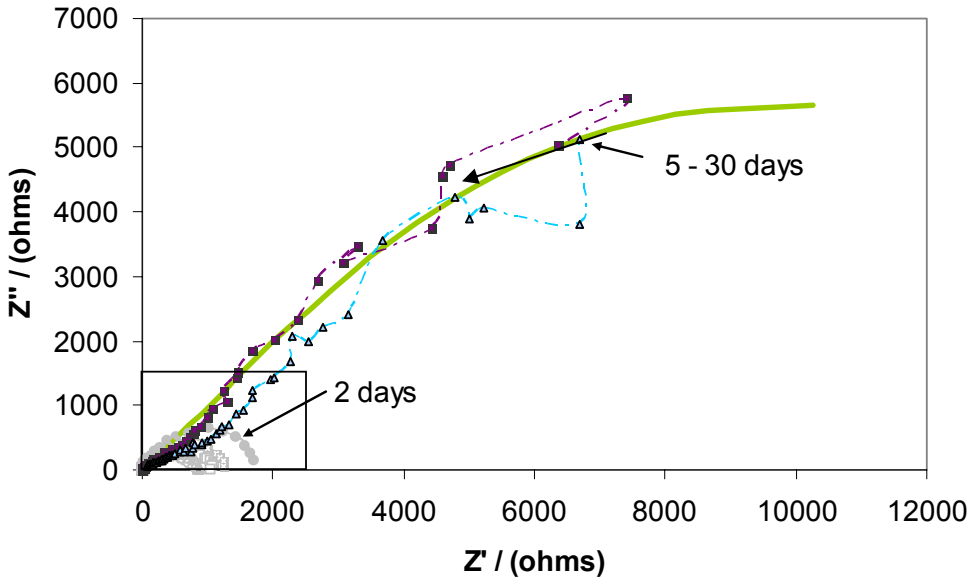

Figure 47. Experiment 3 - Comparison of Nyquist plot (5 – 30 days from experiment and model (15 ppm Fe^{2+}, 20 ppm H_2S, pH = 6.0, $SS_{FeS} = 7$, $SS_{FeCO3} = 9$). The small rectangle in the figure is the Figure 46. Figure 46 had been zoomed in as the axes have been stretched to plot other curves. Model parameters: $D/\delta = 1.25 \times 10^{-4}$ m/s, $\delta_f = 62$ μm and $\varepsilon = 0.59$. The curve that has been modeled is the one that was obtained at 5 days from the beginning of the experiment. The continuous line is the model curve and the discontinuous one is the experimental curve.

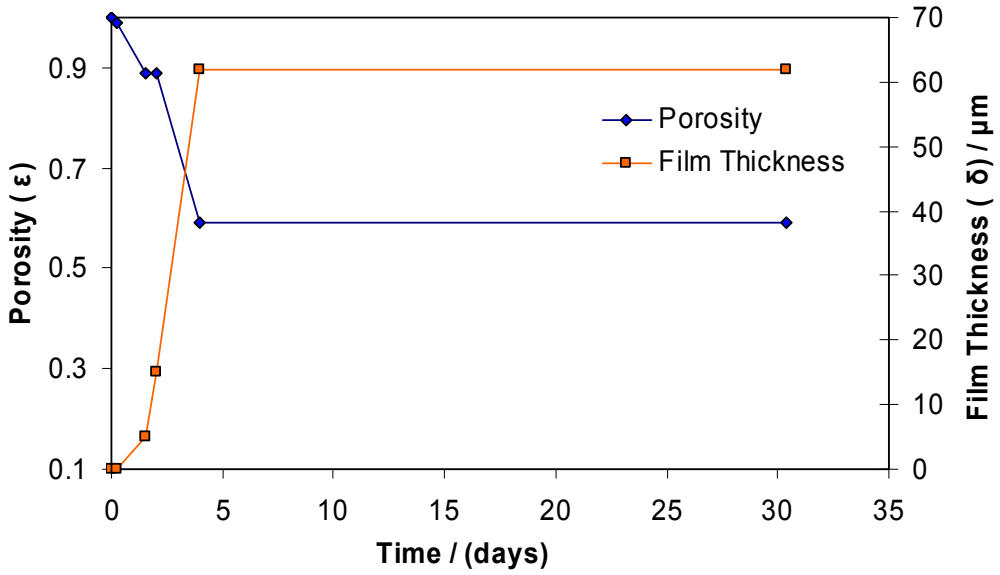

Figure 48. Experiment 3 - Change in porosity and thickness of the film as given by the model (15 ppm Fe^{2+}, 20 ppm H_2S, pH = 6.0, $SS_{FeS} = 7$, $SS_{FeCO3} = 9$).

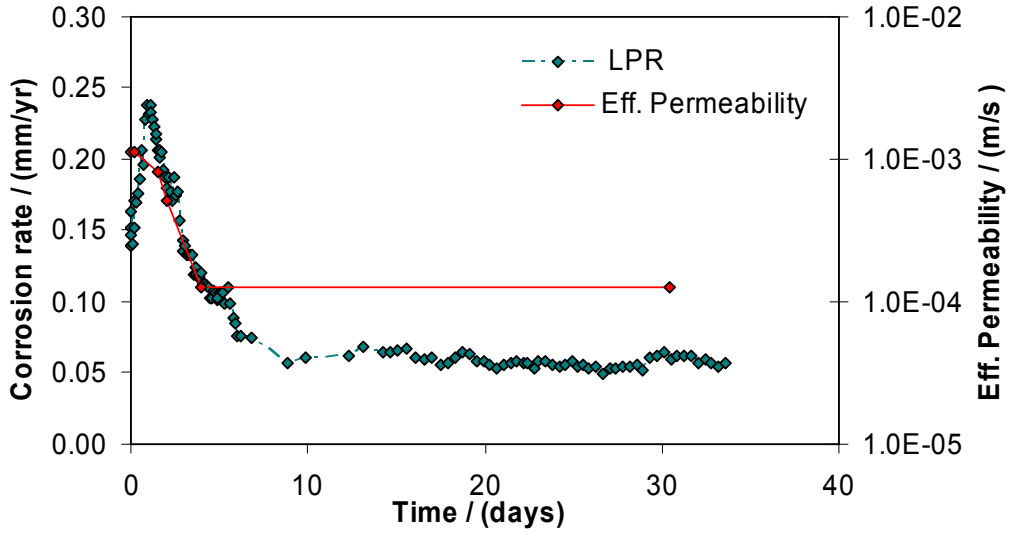

Figure 49. Experiment 3 - Comparison of effective permeability with time as given by the model and corrosion rate with time as given by the LPR method (15 ppm Fe^{2+}, 20 ppm H_2S, pH = 6.0, $SS_{FeS} = 7$, $SS_{FeCO3} = 9$).

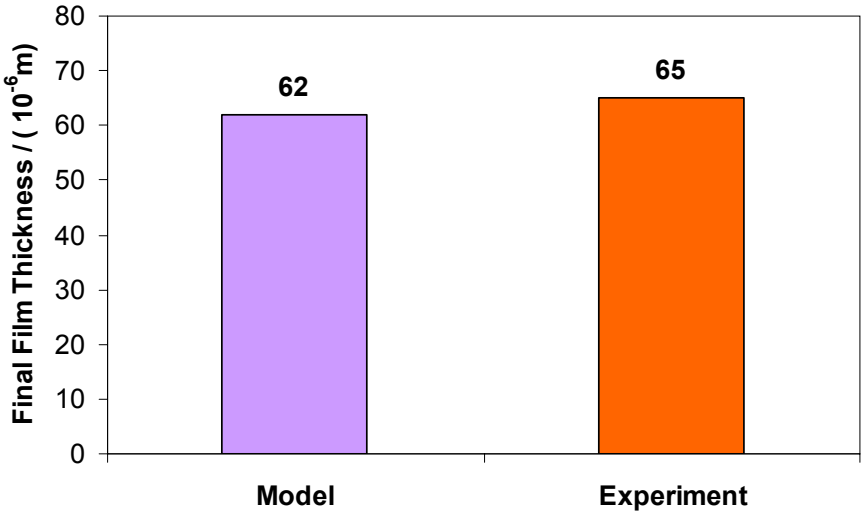

Figure 50. Experiment 3 - Comparison of film thickness as given by the model and from the experiment (15 ppm Fe^{2+}, 20 ppm H_2S, pH = 6.0, $SS_{FeS} = 7$, $SS_{FeCO3} = 9$). The SEM image of the cross section of the specimen is shown in Figure 26.

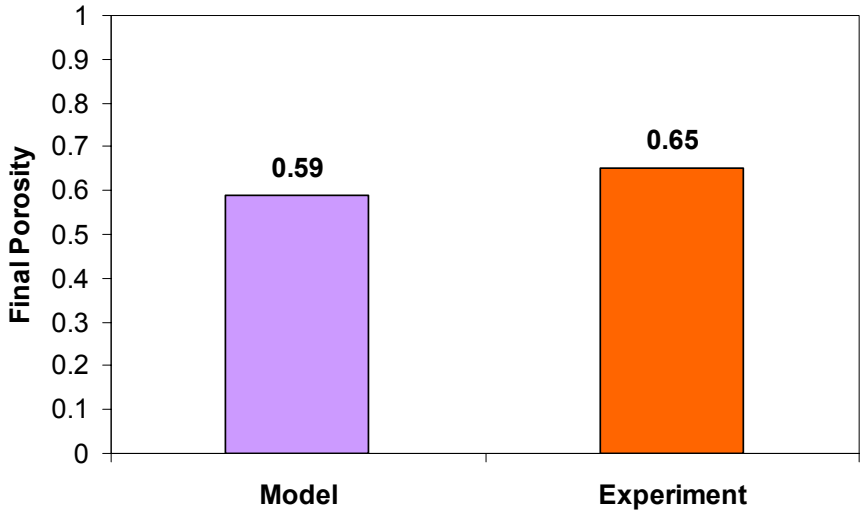

Figure 51. Experiment 3 - Comparison of film porosity as given by the model and calculated from the experiment (15 ppm Fe^{2+}, 20 ppm H_2S, pH = 6.0, $SS_{FeS} = 7$, $SS_{FeCO3} = 9$). Porosity of the film is calculated assuming a 100% $FeCO_3$ film.

Experiment 4

Corrosion rates from LPR and weight loss method for this experiment are shown in Figure 27. Figure 52 through Figure 54 show the comparison of the experimental Nyquist plots with time for Experiment 4, with that of the curves given by the model. It could be observed that the corrosion rate for this experiment has decreased with time and has reached a constant value after 15 days. No change in the Nyquist plots was seen after 15 days from the beginning of the experiment and the corrosion rate also seemed to be constant. Film formation was the reason for the decrease in corrosion rate for this experiment also. Figure 55 shows the change in porosity and thickness of the film on the surface of the metal with time as given by the model and Figure 56 shows the comparison of the trend of effective permeability with time as given by the model and the corrosion rate as measured by LPR method by time. Figure 57 shows the comparison of film thickness from the model and experiment. The optical microscopy image of the cross section of the sample is shown in Figure 29 and Figure 58 shows the comparison of film porosity as calculated from the experiment and as given by the model. There is a good agreement of values of film thickness and film porosity obtained from experiment and from model.

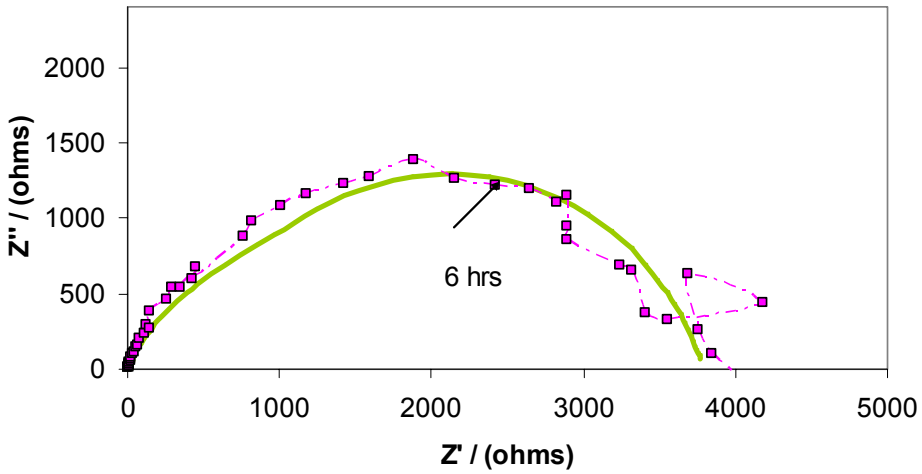

Figure 52. Experiment 4 - Comparison of Nyquist plot (6 hours) from experiment and model (5 ppm Fe^{2+}, 10 ppm H_2S, pH = 6.0, $SS_{FeS} = 3$, $SS_{FeCO3} = 6$). Model parameters: $D/\delta = 1.12 \times 10^{-3}$ m/s, $\delta_f = 0$ µm and $\varepsilon = 0.99$. The continuous line is the model curve and the discontinuous one is the experimental curve.

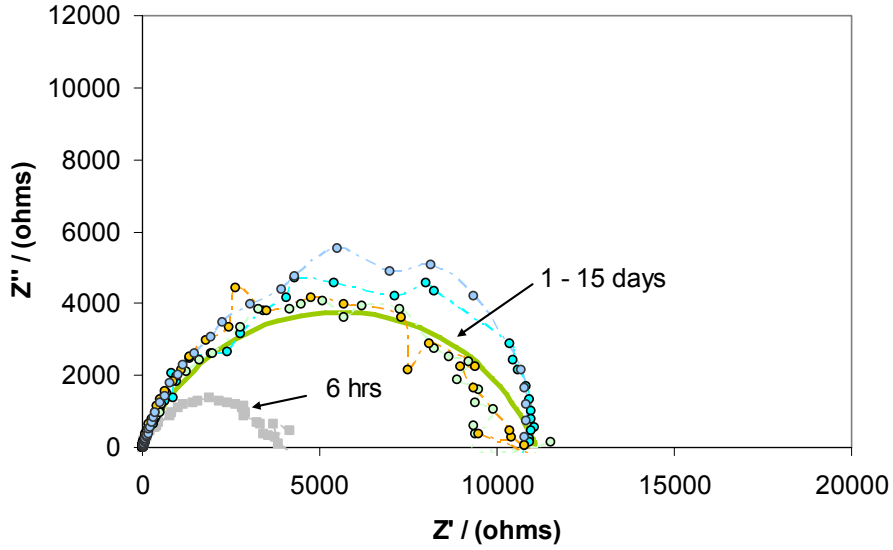

Figure 53. Experiment 4 - Comparison of Nyquist plot (1.5 days) from experiment and model (5 ppm Fe^{2+}, 10 ppm H_2S, pH = 6.0, $SS_{FeS} = 3$, $SS_{FeCO3} = 6$). Model parameters: $D/\delta = 1.6 \times 10^{-4}$ m/s, $\delta_f = 50$ µm and $\varepsilon = 0.62$. The continuous line is the model curve and the discontinuous one is the experimental curve.

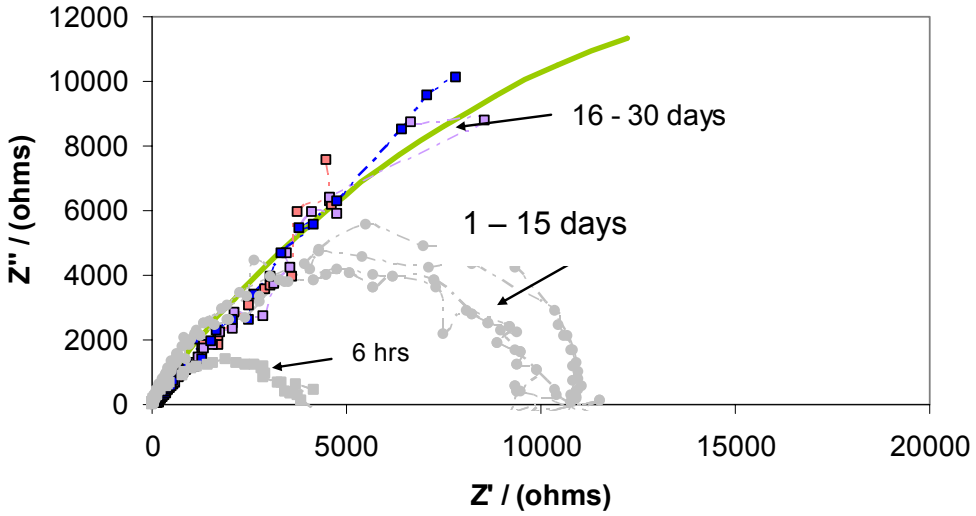

Figure 54. Experiment 4 - Comparison of Nyquist plot (16 days) from experiment and model (5 ppm Fe^{2+}, 10 ppm H_2S, pH = 6.0, $SS_{FeS} = 3$, $SS_{FeCO3} = 6$). Model parameters: $D/\delta = 8.61 \times 10^{-5}$ m/s, $\delta_f = 100$ µm and $\varepsilon = 0.62$. The continuous line is the model curve and the discontinuous one is the experimental curve.

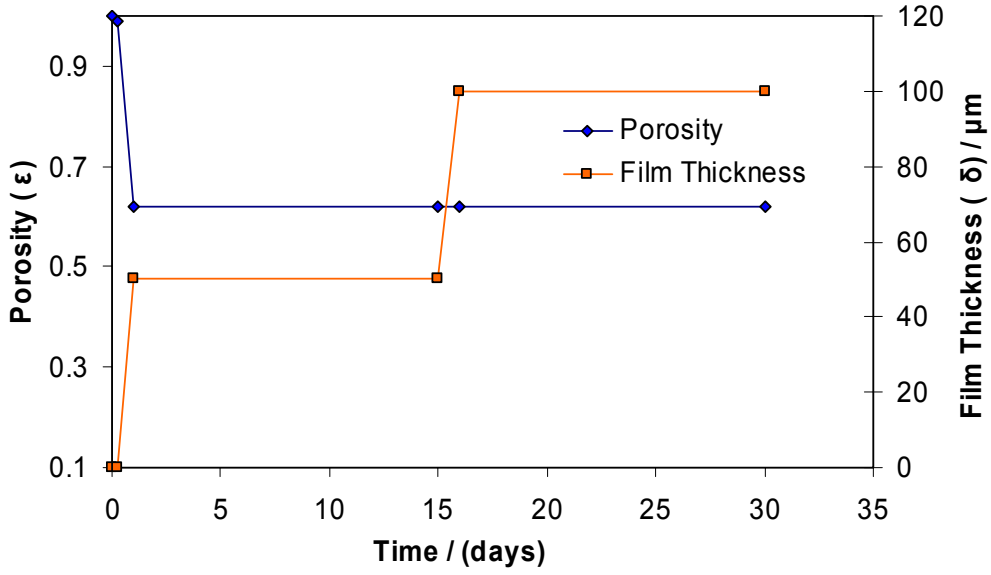

Figure 55. Experiment 4 – Change in porosity and thickness of the film as given by the model (5 ppm Fe^{2+}, 10 ppm H_2S, pH = 6.0, $SS_{FeS} = 3$, $SS_{FeCO3} = 6$).

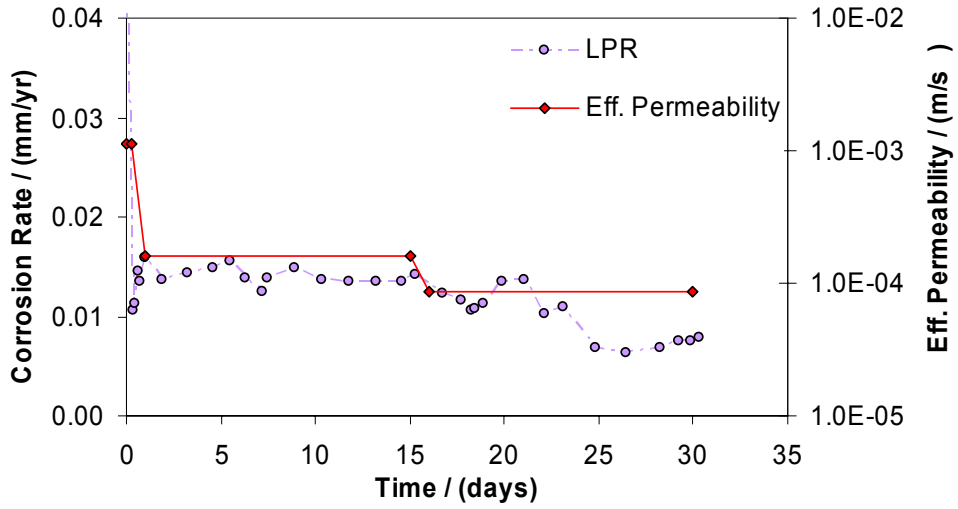

Figure 56. Experiment 4 - Comparison of effective permeability with time as given by the model and corrosion rate with time as given by the LPR method (5 ppm Fe^{2+}, 10 ppm H_2S, pH = 6.0, $SS_{FeS} = 3$, $SS_{FeCO3} = 6$).

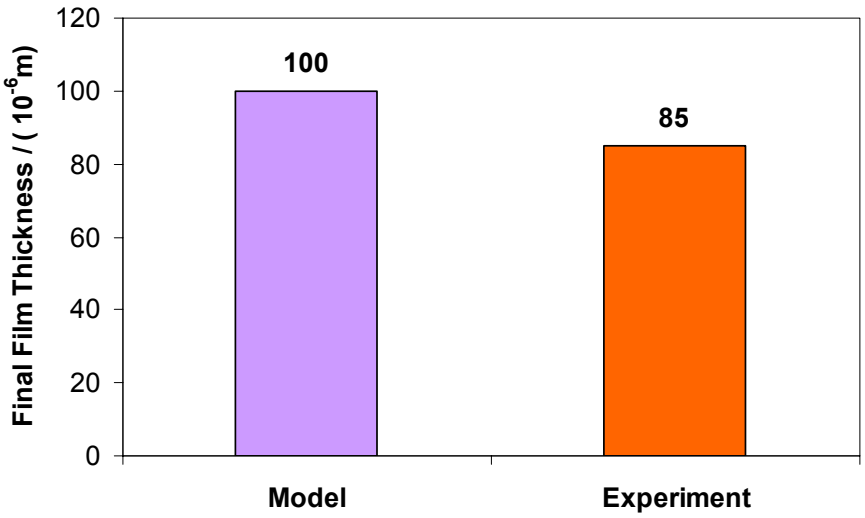

Figure 57. Experiment 4 – Comparison of film thickness as given by the model and from the experiment (5 ppm Fe^{2+}, 10 ppm H_2S, pH = 6.0, $SS_{FeS} = 3$, $SS_{FeCO3} = 6$). The optical microscopy image of the cross section of the specimen is shown in Figure 29.

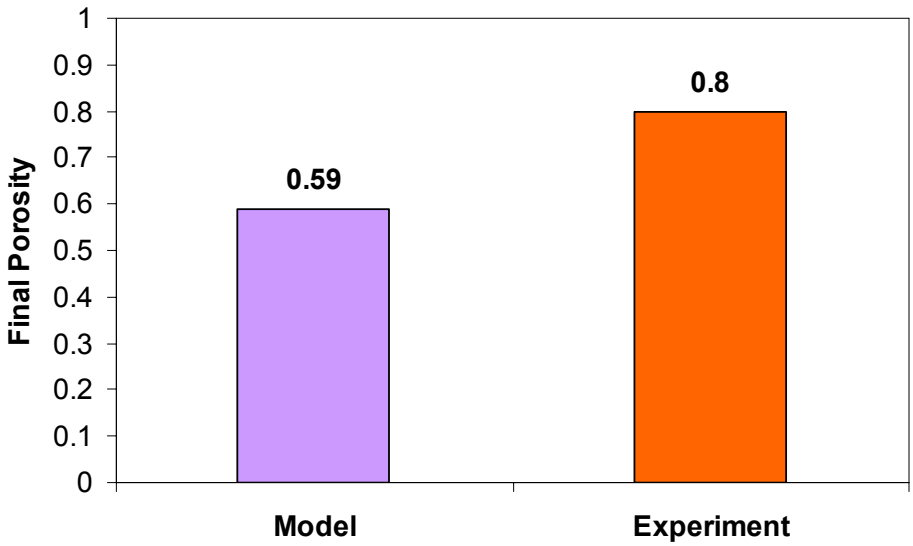

Figure 58. Experiment 4 – Comparison of final film porosity as given by the model and calculated from the experiment (5 ppm Fe^{2+}, 10 ppm H_2S, pH = 6.0, $SS_{FeS} = 3$, $SS_{FeCO3} = 6$). Porosity of the film is calculated assuming a 100% $FeCO_3$ film.

In general, for all the experiments, decrease in the diffusivity of H^+ ions and increase of the film thickness led to the decrease in corrosion rate. Porosity has been shown to be an important factor in the determination of corrosion rate. Initially, since there is no film, a porosity is 1 (100 %) is assumed and as the film starts to grow, the porosity of the film decreases depending on the type of film that is formed on the metal surface which, in turn depends, on various factors like pH value of the solution, the Fe^{2+}concentration, and the saturation value of the iron carbonate or iron sulfide film.

CHAPTER 8: CONCLUSIONS

Conclusions from the experimental work

1. A porous surface film observed at the end of the experiments conducted the presence of H_2S in a CO_2 environment confirmed that the observed decrease in corrosion rate was due to the coverage of the surface of the metal by film which acted as a diffusion barrier for the corrosive species.

2. Even in the "gray zone" conditions, localized corrosion was not observed for the material tested (AISI 1018) under the conditions studied.

3. Porosity and thickness of the film were found to be the most important factors determining the corrosion rate under the conditions studied.

4. Effective permeability of the corrosive species was found to be directly related to the corrosion rate of the metal sample.

REFERENCES

Altoe P., Pimenta G., Moulin C.F., Diaz S.L., and Mattos O.R., "Evaluation of Oilfield Corrosion Inhibitors in CO2 Containing Media : A Kinetic Study", Electrochemica Acta, 41 (1996): p.1165.

Bockris J.O.M., Drazic D., and Despic A.R., Electrochimica Acta, 4 (1961): p. 325.

Bonis M. R., and Crolet J.L., "Basics of the Prediction of the Risks of CO_2 corrosion in Oil and Gas Wells", Corrosion/89, paper no. 466.

Brown B., and Schubert A., "The design and development of a large-scale, multiphase flow loop for the study of corrosion in sour gas environments", Corrosion/2002, paper no. 02502.

Brown B., Lee K-L.J., and Nesic S., "Corrosion in multiphase flow containing small amounts of H_2S", Corrosion/ 2003, paper no. 03341.

Brown B., Parkala S.R., and Nesic,S., "$C0_2$ corrosion in the presence of trace amounts of H2S", " Corrosion/2003, paper no. 04736.

Darowicki K., "Corrosion rate measurements by Non-linear Electrochemical Impedance Spectroscopy", Corrosion Science, 37 (1995): p. 913.

Davies J. T., Turbulence Phenomena, (Academic Press, 1972).

Dugstad Arne, "The importance of $FeCO_3$ supersaturation on the CO_2 corrosion of carbon steels," CORROSION/92, paper no.14.

Dugstad Arne, Lunde L., Videm K., "Parametric testing of CO_2 corrosion of carbon steel," CORROSION/94, paper no.14.

Gerischer H. and Mehl W., Z. physik. Chem, (1955): p.1049.

Gray L.G. S., Anderson B.G., Danysh M. J., and Tremaine P.G., " Mechanism of Carbon Steel Corrosion in Brines Containing Dissolved Carbon Dioxide at pH 4", Corrosion/89, paper no. 464, (Houston, TX: NACE International, 1989).

Gray L.G. S., Anderson B.G., Danysh M. J., and Tremaine P.G., " Effect of pH and Temperature on the Mechanism of Carbon Steel Corrosion by Aqueous Carbon Dioxide", Corrosion /90, paper no.40, (Houston, TX: NACE International, 1990).

Gulbrandsen E., Nesic S., Stangeland A., Buchardt T., Sundfaer B., Hesjevik S. M., Skjerve S. "Effect of precorrosion on the performance of inhibitors for CO_2 corrosion of carbon steel," CORROSION/1998, paper no. 013.

Hausler R.H., Stegmann D.W., "CO2 corrosion and its prevention by chemical inhibition in oil and gas production", CORROSION/1988, paper no. 363.

Harmandas N.G., and Koutsoukos P.G, "The Formation of Iron(II) Sulfides in Aqueous Solutions", Journal of Crystal growth, 167 (1996): p.719.

Heyrosky J., Rec. Trav. Chim. Pays-Bas, 44 (1925): p.499.

Ikeda A., Mukai S., and Ueda M., "Corrosion behavior of 9 to 25% Cr steels in wet $C0_2$ environments", Corrosion/1984, paper no. 289.

Ikeda A., Ueda M., and Mukai S., "Influence of environmental factors on corrosion in $C0_2$ source well", Corrosion/2002.

Jasinski R., "Corrosion of N80-type steel by $C0_2$/water mixtures", Corrosion/1987.

Johnson M. L., Tomson M. B., "Ferrous carbonate precipitation kinetics and its impact on carbon dioxide corrosion", CORROSION/91, paper no.268. (Houston, TX: NACE International, 1991).

Keddam M., Mattos O.R., and Takenouti H., "Reaction Model for Iron Dissolution Studied by Electrode Impedance", J. Electrochem. Soc., 128 (1981): p.257.

Kermani M. B. and Morshed A., "Carbon dioxide corrosion in oil and gas production-a compendium," Corrosion, Vol.59, No. 8, (2003): p.659.

Kinsella B., Tan Y.J., and Bailey S., "EIS and Surface Characterisation Techniques to Study Carbondioxide Corrosion Product Scales", Corrosion/1998.

Kvarekval J., Nyborg R., and Seiersten M., "Corrosion product films on carbon steel in semi-sour $C0_2/H_2S$ environments", Corrosion/2002, paper no. 02296.

Lee K. L., "EIS Investigation of CO_2 / H_2S Corrosion," Advisory Board Meeting Report/Sept 2003, Institute for Corrosion and Multiphase Technology, Ohio University, OH, USA.

Levich V. G., Physicochemical Hydrodynamics, translation from Russian (Englewood Cliffs, NJ: Prentice-Hall Inc., 1962), p. 60.

Ma H.Y., Cheng X.L., Chen S.H., Li G.Q., Chen X., Lei S.B., and Yang H.Q., "Theoretical Interpretation on Impedance Spectra for Anodic Dissolution in Acidic Solutions Containing Hydrogen Sulfide", Corrosion/1998.

Ma H., Cheng X., Li G.Q., Chen S., Quan Z., Zhao S., and Niu L., "The Influence of Hydrogen Sulfide on Corrosion of Iron under Different Conditions", Corrosion Science, 42 (2000): p. 1669.

Morris D. R., Sampaleanu L.P., and Veysey., " The Corrosion of Steel by Aqueous Solutions of Hydrogen Sulfide", J. Electrochem. Soc., 127 (1980): p.1228.

Nesic S., Pots B.F.M., Postlethwaite J., and Thevenot N., "Superposition of diffusion and chemical reaction controlled limiting currents – application to CO_2 corrosion", J. Corrosion science and engineering, ISSN 1466-8858, (1995).

Nesic S., Postlethwaite J., and S. Olsen, "An Electrochemical Model for Prediction of CO_2 Corrosion", CORROSION/95, paper no.131.

Nesic S., Nordsveen M., Nyborg R., and Stangeland A., "A Mechanistic Model for CO_2 Corrosion with Protective Iron Carbonate Films", Corrosion/2001, paper no. 1040.

Nesic S. Lee K.L.J., and Ruzic V., "A mechanistic model of iron carbonate film growth and the effect on CO_2 corrosion of mild steel," Corrosion/2002, paper no. 02237.

Newman J.S., Electrochemical Systems, 2nd Edition, (Prentice Hall, Englewood Cliffs, New Jersey, 1991).

Roberge Pierre, *Handbook of corrosion Engineering*, McGraw Hill. 1999.

Shoesmith D.W., Taylor P., Bailey M.G., and Owen D.G., "The Formation of Ferrous Monosulfide Polymorphs during the Corrosion of Iron by Aqueous Hydrogen Sulfide at 21ºC,"J. Electrochem. Soc. 127 (1980) p.1007.

M. Sluyters-Rembach and J.H. Sluyters, Electroanalytical Chemistry, Vol. 4 (A. J. Bard, ed.), Marcel Dekker, New York, 1970.

Sun Y., George K., and Nesic S., "The effect of Cl^- and acetic acid on localized C02 corrosion in wet gas flow" Corrosion/2003, paper no. 03327.

Tafel J., Z. Physik, Chem, 50 (1905): p.641.

Valdes A., Case R., Ramirez M., and Ruiz A., "The effect of small amounts of H_2S on $C0_2$ corrosion of a carbon steel", Corrosion/1998, paper no. 22.

Van Hunnik E.W.J, Pots B.F.M., and Hendriksen E.L.J.A., "The formation of protective $FeCO_3$ corrosion product layers in CO_2 corrosion," CORROSION/96, paper no. 6.

Vetter K.J., Electrochemische Kinetik, (Springer-Verlag, Berlin, 1961) p. 256.

Videm K., Kvarekval J., "Corrosion of carbon steel in $C0_2$ saturated aqueous solutions containing small amounts of H_2S", Corrosion/1994, paper no.12.

Warburg E., Wied. Ann., 67 (1899): p.493.

APPENDIX A: OVERVOLTAGE RESPONSE

Charge transfer overvoltage response

The relationship between the charge transfer overvoltage when a sinusoidal current of small amplitude is given as an input was derived by Gerischer and Mehl as follows (Gerischer and Mehl, 1955):

$$\eta_t = \frac{I\sin(\omega t)}{L_D - \frac{ab}{b^2 + C_H^2\omega^2} + \frac{aC_H\omega}{b^2 + C_H^2\omega^2}j} \tag{3-9}$$

where,

j = imaginary component = $\sqrt{-1}$,

Charge transfer over voltage arises when the charge transfer reaction is the slowest or the rate determining step during flow of current. Therefore one needs to determine the relationship between current and over voltage resulting from the charge transfer reaction. The two-step charge transfer process with two possible paths of hydrogen evolution as shown above can be modeled by mathematical equations. The reaction (2-5) for the reduction of hydrogen ions on the bare metal surface can be modeled by the following relationship:

$$i_1 = (1-\theta)i_{0,1}10^{(-\eta/b_1)} \tag{A-1}$$

where

θ = coverage factor, percentage of H_{ads} covered on the metal surface ($0 \le \theta \le 1$)

$i_{0,1}$ = exchange current density for hydrogen ion reduction on fully uncovered electrode at equilibrium potential ≈ 1.58×10^{-2} A/m^2 for 20^{o}C and pH5

η= overvoltage = $\varepsilon-\varepsilon_0$

ε_0 = equilibrium potential

b_1= Tafel slope = $2.303RT/\alpha_1 F$

α_1=Symmetry factor, according to Bockris et al., for hydrogen evolution, α_1=0.5 giving b_1=0.108 at 20^{o}C.

On the other hand, Heyrosky's reaction (2-6) requires an adsorbed hydrogen atom to react with a hydrogen ion and an electron. Since this is an electrochemical reaction involving charge transfer, it can be described similarly as above:

$$i_2 = \theta i_{0,2} e^{(-\eta / b_2)} \tag{A-2}$$

The recombination of H_{ads} is a chemical reaction requiring two adsorbed hydrogen atoms; therefore rate of reaction (2-7) is modeled as:

$$K_3 = 2Fk_{f3}\theta^2 \tag{A-3}$$

The rate of change of H_{ads} adsorption coverage θ on the metal surface is described by the fact that reaction of hydrogen ion reduction (2-5) increases the H_{ads} adsorption coverage, whereas the Heyrosky's reaction (2-6) and recombination chemical reaction (2-7) decreases the adsorption coverage. Hence

$$\frac{d\theta}{dt} = \frac{i_1 - i_2 - K_3}{C_H} \tag{A-4}$$

where C_H is the constant linking the fraction of the adsorbed surface θ and the surface concentration of adsorbed species expressed in mol/cm^2. It is also called adsorption capacitance and it is considered to be equal to10^{-8} mol/cm^2. Combining equations (A-1)

through (A-4), with the initial condition on the metal surface which is: t=0; θ=0, adsorption coverage can be determined as a function of time θ(t).

Therefore the individual current i_1, i_2 is a function of over voltage and adsorption coverage, which is a function of time. The total current resulting from the cathodic charge transfer of hydrogen evolution is the sum of individual currents:

$$i_{total} = i_1 + i_2 \tag{A-5}$$

Hence when a sinusoidal alternating current of small amplitude is induced, a relationship between charge transfer over voltage and current was obtained as

$$\eta_t = \frac{I\sin(\omega t)}{L_D - \frac{ab}{b^2 + C_H^2\omega^2} + \frac{aC_H\omega}{b^2 + C_H^2\omega^2}j} \tag{A-6}$$

Where

j = imaginary component $= \sqrt{-1}$

$$L_D = \frac{F(\alpha_1 i_1^{'} + \alpha_2 i_2^{'})}{RT}$$

$$a = \frac{F(i_2 - i_1)(\alpha_2 i_2^{'} - \alpha_1 i_1^{'})}{RT}$$

$$b = i_1 + i_2 + 2F\theta^{'}k_{f3}$$

$i_1^{'}$, $i_2^{'}$ and $\theta^{'}$ are values at equilibrium potential.

It is seen in equation (A-6), that real and imaginary components in the denominator are both frequency dependent. This frequency dependence was evoked by periodic change of adsorption coverage 'θ'. This charge transfer over voltage has a phase shift with respect to the alternating current, and that's why there is an imaginary component.

Diffusion over voltage in infinite boundary layer

The relationship between the diffusion overvoltage when a sinusoidal current of small amplitude is given as an input was derived by Warburg as follows (Warburg, 1899):

$$\eta_d = \frac{RT}{n^2F^2}\frac{v^2}{\sqrt{\omega}[H^+]_{bulk}\sqrt{D_{H^+}}} I\sin(\omega t - \frac{\pi}{4}) \qquad (3\text{-}10)$$

where

ν = stoichiometric constant

$[H^+]_{bulk}$ = concentration of H^+ ions in the bulk

D_{H^+} = diffusion coefficient for H^+ ions.

The diffusion over voltage lags behind the current by a phase angle of $\pi/4=45^o$ and the so-called Warburg Impedance can be determined by:

$$Z_w = \frac{\eta_d}{i} \qquad (A\text{-}7)$$

where $i = I\sin(\omega t)$

The derivation for Warburg Impedance is as follows:

The change in the concentration of H^+ ions with respect to time and the distance from the metal surface should be evaluated as a result of diffusion process. Hence Fick's second law in the following form

$$\frac{\partial c}{\partial t} = D\frac{\partial^2 c}{\partial x^2} \qquad (A\text{-}8)$$

is applied for the change of the concentration (c) of H^+ ions with time (t) and distance (x) from the metal surface as a result of the diffusion processes where D is the diffusivity of H^+ ions. An assumption is made such that

$$\Delta c(x,t) = \frac{c(x,t) - \bar{c}}{\bar{c}} \tag{A-9}$$

Where $\bar{c}$ = bulk concentration. Substituting this equation in Fick's Law,

We get

$$\frac{\partial \Delta \mathrm{c}}{\partial \mathrm{t}} = \mathrm{D}\frac{\partial^2 \Delta \mathrm{c}}{\partial \mathrm{x}^2} \tag{A-10}$$

For an external imposed current, $i = I\sin(\omega t)$,

The boundary conditions at the surface of the metal are as follows:

$$\left(\frac{\partial \Delta c}{\partial x}\right)_{x=0} = -\frac{1}{nF\bar{c}D} I\sin\omega t \tag{A-11}$$

$$\Delta c_{x=\infty} = 0 \tag{A-12}$$

and the initial condition is $\Delta C(x,0) = 0$ (A-13)

Using separation of variables to solve the equation,

$$\Delta c(x,t) = X(x)T(t) \tag{A-14}$$

Substituting into Fick's Law (A-10), we get

$$\frac{\partial\left(X(x)T(t)\right)}{\partial t} = D\frac{\partial^2\left(X(x)T(t)\right)}{\partial x^2} \Rightarrow X(x)T'(t) = DX''(x)T(t) \tag{A-15}$$

After separating the variables, we have:

$$\frac{T'(t)}{T(t)} = \frac{DX''(x)}{X(x)} \tag{A-16}$$

For equality to hold, $\frac{T'(t)}{T(t)} = \alpha$ and $\frac{DX''(x)}{X(x)} = \alpha$

For X(x) space domain:

$$DX''(x) - \alpha X(x) = 0 \tag{A-17}$$

The characteristic equation for (A-17) is $D\lambda^2 - \alpha = 0$

One obtains two real roots for the above equation as $\lambda = \pm\sqrt{\frac{\alpha}{D}}$

Therefore the general solution of the X(x) of space domain:

$$X(x) = C_1 e^{\lambda x} + C_2 e^{-\lambda x}$$

Applying the boundary condition (A-12), we have

$$\Delta c_{x=\infty} = X(\infty)T(t) = 0$$

$$0 = C_1 e^{\lambda\infty} + C_2 e^{-\lambda\infty}$$

Hence $C_1 = 0$,

Therefore $X(x) = C_2 e^{-\lambda x}$ (A-18)

For time domain:

$$T' - \alpha T = 0$$

The general solution for this equation is :

$$T(t) = Ae^{\alpha t} \tag{A-19}$$

Combining the two general solutions in equations (A-18) and (A-19) together, we get

$$\Delta c = X(x)T(t) = C_2 e^{-\lambda x} Ae^{\alpha t} \tag{A-20}$$

Substitution of the expression in equation (A-20) into equation (A-10) and partial differentiation of the equation yields:

$$\frac{\partial \Delta c}{\partial t} = D\frac{\partial^2 \Delta c}{\partial x^2} \Rightarrow \frac{\partial\left(C_2 e^{-\lambda x} Ae^{\alpha t}\right)}{\partial t} = D\frac{\partial^2\left(C_2 e^{-\lambda x} Ae^{\alpha t}\right)}{\partial x^2} \tag{A-21}$$

C_2 can be obtained by applying the boundary condition mentioned in equation (A-11)

$$\left(\frac{\partial\left(C_2 e^{-\lambda x} Ae^{\alpha t}\right)}{\partial x}\right)_{x=0} = -C_2 \lambda e^{-\lambda x=0} \;\; Ae^{\alpha t} = -\frac{1}{nF\bar{c}D} I \sin \omega t$$

$Sin\omega t = e^{i\omega t}$ from the relationship according to Euler's theorem and assuming $A = I$, we get

$$\alpha = i\omega \;\text{ and }\; C_2 = \frac{1}{nF\bar{c}D\lambda} = \frac{1}{nF\bar{c}\sqrt{D\omega i}} = \frac{1-i}{nF\bar{c}\sqrt{2D\omega}}$$

[Imaginay Number Manipulation :

$$(1+i)(1-i) = 1-i^2 = 1+1 = 2$$

$$(1+i) = \frac{2}{1-i}$$

$$i = \frac{2}{1-i} - \frac{1-i}{1-i} = \frac{1+i}{1-i}$$

$$i\times 1=\frac{1+i}{1-i}\times\frac{1-i}{1-i} \qquad i\times 1=\frac{1+i}{1-i}\times\frac{1+i}{1+i}$$

$$\downarrow \qquad\qquad \downarrow$$

$$i=\frac{2}{(1-i)^2} \qquad i=\frac{(1+i)^2}{2}$$

$$\downarrow \qquad\qquad \downarrow$$

$$\sqrt{i}=\frac{\sqrt{2}}{(1-i)} \qquad \sqrt{i}=\frac{(1+i)}{\sqrt{2}} \quad]$$

Combining all the constants, $\Delta c=\dfrac{1-i}{nF\bar{c}\sqrt{2D\omega}}e^{-\sqrt{\frac{i\omega}{D}}x}Ie^{i\omega t}$ (A-22)

And from the Imaginary number manipulation Substituting the expression for i in the exponent part, we get,

$$\Delta c=\frac{1-i}{nF\bar{c}\sqrt{2D\omega}}e^{-\sqrt{\frac{\omega}{2D}}x}e^{-\sqrt{\frac{\omega}{2D}}ix}Ie^{i\omega t}$$

And $1-i=\sqrt{1^2+(-1)^2}e^{i\theta}$ where $\theta=\tan^{-1}\left(\dfrac{-1}{1}\right)=-\dfrac{\pi}{4}$

So, $1-i=\sqrt{2}e^{-\frac{\pi}{4}i}$

Therefore the final expression for the concentration gradient becomes

$$\Delta c=\frac{\sqrt{2}}{nF\bar{c}\sqrt{2D\omega}}e^{-\sqrt{\frac{\omega}{2D}}x}Ie^{(i\omega t-\sqrt{\frac{\omega}{2D}}ix-\frac{\pi}{4}i)} \qquad \text{(A-23)}$$

Since $\Delta c(x,t)=\dfrac{c(x,t)-\bar{c}}{\bar{c}}$,

$$c(x,t) = \bar{c} + \frac{I}{nF\sqrt{D\omega}} e^{-\sqrt{\frac{\omega}{2D}}x} \sin\left(\omega t - \sqrt{\frac{\omega}{2D}}x - \frac{\pi}{4}\right) \tag{A-24}$$

Expression for the concentration over potential is given by

$$\eta_d = \frac{RT}{nF} \ln \frac{(C)}{\left(\bar{C}\right)} \tag{A-25}$$

$$\text{Therefore } \eta_d = \frac{RT}{nF} \ln \frac{c}{\bar{c}} \approx \frac{RT}{nF} \frac{\Delta c}{\bar{c}} \text{ since } \{ \ln x = 1- x \text{ for } x<<<1) \tag{A-26}$$

Substituting (A-24) in (A_26) we get

$$\eta_d = \frac{IRT}{n^2F^2\bar{c}\sqrt{D\omega}} e^{-\sqrt{\frac{\omega}{2D}}x} \sin\left(\omega t - \sqrt{\frac{\omega}{2D}}x - \frac{\pi}{4}\right) \tag{A-27}$$

But $e^{-\sqrt{\frac{\omega}{2D}}x} = \sin\left(-\sqrt{\frac{\omega}{2D}}x\right)$

So,

$$\eta_d = \frac{IRT}{n^2F^2\bar{c}\sqrt{D\omega}} \sin\left(\omega t - \frac{\pi}{4}\right) \tag{A-28}$$

For $i = I\sin(\omega t)$

The overvoltage response for mass transfer in infinite boundary layer or stagnant condition (Warburg 1899)

$$\eta_d = \frac{RT}{n^2F^2} \frac{\nu^2}{\sqrt{\omega}\,\bar{c}\sqrt{D_{H^+}}} I\sin(\omega t - \frac{\pi}{4}) \tag{3-10}$$

[Explanation for the equation for concentration (or diffusion) over potential:

$\eta_c = \frac{RT}{nF} \ln \frac{(C)}{\left(\bar{C}\right)}$ means that the potential difference observed at equilibrium or zero current is not equal to the potential difference observed at a current density i not equal to zero.

The expression mentioned above can be explained as follows:

The general equation. for a half cell reaction is:

$$aA + m\ H^+ + n\ e^- \leftrightarrow b\ B + d\ H_2O \qquad (a)$$

For this equation., the potential is given by Nerst Equation,

$$e = e^0 + \frac{2.3RT}{nF} \log \frac{(A)^a \left(H^+\right)^m}{(B)^b \left(H_2O\right)^d} \qquad (b)$$

The equation (b) for the reaction given below at equilibrium (i = 0)

$2H^+ + 2\ e^- \leftrightarrow H_2$, becomes

$$e_e = e^0 + \frac{2.3RT}{nF} \log \frac{\left(H_b{}^+\right)^2}{\left(H_2\right)} \qquad (c)$$

where e_e = potential at equilibrium, $H_b{}^+$= conc. in bulk.

The same equation for the case of ($i \neq 0$)

$$e = e^0 + \frac{2.3RT}{nF} \log \frac{\left(H_{x=0}{}^+\right)^2}{\left(H_2\right)} \qquad (d)$$

where e = potential at ($i \neq 0$), $H^+_{x=0}$= concentration of H^+ ions at the metal surface.

From (c) and (d) we can write

$$\eta_d = e - e_e = \nu \frac{RT}{nF} \ln \frac{(C)}{\left(\bar{C}\right)}$$

where ν = stiochiometric coefficient of the species in the reaction equation.]

Diffusion overvoltage in infinite boundary layer and limiting reaction

The over voltage response with both diffusion and reaction when an alternating sinusoidal current is given as an input was given by Vetter as follows (Vetter, 1961):

$$\eta_r = \frac{RT}{n^2F^2} \frac{v^2}{\sqrt{\omega}[H^+]_{bulk}\sqrt{2D_{H^+}}} \sqrt{\frac{\sqrt{1+\left(\frac{k}{\omega}\right)^2}+\frac{k}{\omega}}{1+\left(\frac{k}{\omega}\right)^2}} I \sin \omega t - \frac{RT}{n^2F^2} \frac{v^2}{\sqrt{\omega}[H^+]_{bulk}\sqrt{2D_{H^+}}} \sqrt{\frac{\sqrt{1+\left(\frac{k}{\omega}\right)^2}-\frac{k}{\omega}}{1+\left(\frac{k}{\omega}\right)^2}} I \cos \omega t \quad (3\text{-}12)$$

where,

η_r is the over voltage response in v when there is both diffusion in the infinite boundary layer and limiting reaction, $\lambda = \sqrt{\frac{k+i\omega}{D}}$ and $k = \frac{\upsilon_0 p}{\bar{c}}$ where υ_0 is the equilibrium rate of the H^+ reduction, p is the order of reaction which is 1 in this case and $\bar{c}$ is the bulk concentration of H^+ that could be calculated from the bulk pH value of the solution.

Derivation of the reaction over voltage:

The derivation of reaction overvoltage is similar to the derivation of diffusion over voltage. Beginning with the Fick's Second Law with the reaction term for the change of H^+ concentration with time (t) and distance from the surface of the metal (x) as a result of the diffusion and reaction processes,

$$\frac{\partial c}{\partial t} = D\frac{\partial^2 c}{\partial x^2} + \upsilon \tag{A-29}$$

Vetter proposed the relation for the homogeneous reaction rate ν as

$$\upsilon = \upsilon_0\left[1 - \left(\frac{c}{\bar{c}}\right)^p\right] \tag{A-30}$$

with reaction order p, concentration c and bulk concentration $\bar{c}$. For the evaluation of the reaction impedance, only the current and over voltage range in which a linear relationship exists between current i and over voltage η is of interest. This is true only for relatively small concentration changes.

Since

$$\left(\frac{c}{\bar{c}}\right)^p = \left(1 + \frac{c-\bar{c}}{\bar{c}}\right)^p \approx 1 + p\frac{c-\bar{c}}{\bar{c}} \tag{A-31}$$

the following is approximately valid:

$$\upsilon = -\frac{\upsilon_0 p}{\bar{c}}\Delta c = -k\Delta c \tag{A-32}$$

where $\Delta c = c - \bar{c}$ and $k = \frac{\upsilon_0 p}{\bar{c}}$

The reaction order in this case is p=1. ν_0 is the rate at which the two opposing reactions meet to establish equilibrium and may therefore be designated as the reaction exchange rate.

Substituting equation (A-32) for the reaction rate into equation (A-29) gives the partial differential equation for the concentration difference $\Delta c(x,t) = c(x,t) - \bar{c}$

$$\frac{\partial \Delta c}{\partial t} = D\frac{\partial^2 \Delta c}{\partial x^2} - k\Delta c \tag{A-33}$$

where $\bar{c}$ = bulk concentration (=H^+ in this case)

When an alternating current of frequency $\omega/2\pi$ ($i = I\sin\omega t$) is applied, the boundary conditions at the surface becomes

$$\left(\frac{\partial \Delta c}{\partial x}\right)_{x=0} = -\frac{1}{nFD} I\sin\omega t \tag{A-34}$$

The boundary condition in the above equation means that the passage of current is related to the change in the concentration of H^+ ions on the surface of the metal.

$$\Delta c_{x=\infty} = 0 \tag{A-35}$$

And initial condition is $\Delta C(x,0) = 0$ (A-36)

Using separation of Variables:

$\Delta c(x,t) = X(x)T(t)$

And substituting into Fick's Law (A-33) we get:

$$\frac{\partial\left(X(x)T(t)\right)}{\partial t} = D\frac{\partial^2\left(X(x)T(t)\right)}{\partial x^2} - kXT \Rightarrow X(x)T'(t) = DX''(x)T(t) - kXT \quad \text{(A-37)}$$

Separating the variables:

$$\frac{T'(t)}{T(t)} = \frac{DX''(x)}{X(x)} - k \quad \text{(A-38)}$$

For this equality to hold, $\frac{T'(t)}{T(t)} = \alpha$ and $\frac{DX''(x)}{X(x)} - k = \alpha$

For X(x) space domain:

$$DX''(x) - kX(x) - \alpha X(x) = 0 \quad \text{(A-39)}$$

The characteristic equation for (A-39) is $D\lambda^2 - (\alpha + k) = 0$

And the two real roots are $\lambda = \pm\sqrt{\frac{\alpha + k}{D}}$

Therefore the general solution of the X(x) of space domain is:

$$X(x) = C_1 e^{\lambda x} + C_2 e^{-\lambda x} \quad \text{(A-40)}$$

Applying the boundary condition (A-35) we get

$\Delta c_{x=\infty} = X(\infty)T(t) = 0$

$$\Rightarrow 0 = C_1 e^{\lambda\infty} + C_2 e^{-\lambda\infty}$$

$$\Rightarrow C_1 = 0$$

Therefore $X(x) = C_2 e^{-\lambda x}$ (A-41)

The concentration gradient is now,

$$\Delta C = C_2 e^{-\lambda x} I e^{i\omega t} \quad \text{(A-42)}$$

Since the time domain solution remains the same as the one for Warburg impedance.

Substituting this into the Fick's law in equation (A-33) we get

$$\frac{\partial\left(C_2 e^{-\lambda x} A e^{i\omega t}\right)}{\partial t} = D\frac{\partial^2\left(C_2 e^{-\lambda x} A e^{i\omega t}\right)}{\partial x^2} - kC_2 e^{-\lambda x} A e^{i\omega t} \quad \text{(A-43)}$$

$$i\omega + k = D\lambda^2$$

$$\Rightarrow \lambda = \sqrt{\frac{k + i\omega}{D}}$$

C_2 can be obtained by applying the boundary condition in equation (A-34) as follows:

$$\left(\frac{\partial\left(C_2 e^{-\lambda x} A e^{i\omega t}\right)}{\partial x}\right)_{x=0} = -\lambda C_2 e^{-\lambda x=0}\ A e^{i\omega t} = -\frac{1}{nFD} I \sin\omega t$$

$$C_2 = \frac{1}{nFD\lambda} = \frac{1}{nF\sqrt{D}\sqrt{k + i\omega}} = \frac{1}{nF\sqrt{2\omega}} \frac{\sqrt{\frac{k}{\omega} - i}}{\sqrt{\frac{k^2}{\omega^2} + 1}} \quad \text{(A-44)}$$

Substituting equation (A-44) in the expression for concentration gradient in (A-42),

$$\Delta C = \frac{1}{nF\sqrt{D\omega}} \frac{\sqrt{\frac{k}{\omega} - i}}{\sqrt{\frac{k^2}{\omega^2} + 1}} e^{-\sqrt{\frac{k+i\omega}{D}}x} I e^{i\omega t} \tag{A-45}$$

Reaction overvoltage at the surface is given by $\eta = \frac{RT}{nF} \ln \frac{c}{\bar{c}} \approx \frac{RT}{nF} \frac{\Delta c}{\bar{c}}$ (A-46)

Therefore the reaction over voltage

$$\eta_r = \frac{RT}{n^2F^2} \frac{v^2}{\sqrt{\omega}[H^+]_{bulk}\sqrt{2D_{H^+}}} \sqrt{\frac{\sqrt{1+\left(\frac{k}{\omega}\right)^2} + \frac{k}{\omega}}{1+\left(\frac{k}{\omega}\right)^2}} I \sin \omega t - \frac{RT}{n^2F^2} \frac{v^2}{\sqrt{\omega}[H^+]_{bulk}\sqrt{2D_{H^+}}} \sqrt{\frac{\sqrt{1+\left(\frac{k}{\omega}\right)^2} - \frac{k}{\omega}}{1+\left(\frac{k}{\omega}\right)^2}} I \cos \omega t \tag{3-12}$$

Diffusion overvoltage in finite boundary layer and limiting reaction

The diffusion overvoltage involving the rate determining reaction in turbulent flow conditions was derived by Lee as follows (Lee, 2003):

$$\eta_{d,\delta,r} = \frac{RT}{n^2F^2\left[H^+\right]_{bulk} D_{H^+}\lambda} \tanh(\lambda\delta)\, I \sin \omega t \tag{3-13}$$

where,

$\eta_{d,\delta,r}$ is the diffusion overvoltage response in v involving chemical reaction and turbulent flow conditions and $\lambda = \sqrt{\frac{i\omega + k}{D_{H^+}}}$ and $k = \frac{\upsilon_0 p}{\bar{c}}$ where υ_0 is the equilibrium

rate of the H^+ reduction, p is the order of reaction which is 1 in this case and $\bar{c}$ is the bulk concentration of H^+ that could be calculated from the bulk pH value of the solution.

The derivation of the equation (3-13) is as follows:

In order to derive reaction impedance with mass transfer in a finite boundary layer, one needs to consider the following sequence of reactions:

When CO_2 is dissolved in water, hydration of aqueous carbon dioxide takes place to form carbonic acid:

$$CO_{2(aq)} + H_2O_{(aq)} \xleftrightarrow{Khyd} H_2CO_{3(aq)} \tag{A-47}$$

The carbonic acid H_2CO_3 is then dissociated in two steps:

$$H_2CO_{3(aq)} \xleftrightarrow{Kca} H^+_{(aq)} + HCO^-_{3(aq)} \tag{A-48}$$

$$HCO^-_{3(aq)} \xleftrightarrow{Kbi} H^+_{(aq)} + CO^{2-}_{3(aq)} \tag{A-49}$$

It is proposed that carbonic acid provides a reservoir of H^+ ions at a given pH. Therefore hydrogen evolution is assumed to be the most dominant cathodic reaction.

$$H^+ + e^- \leftrightarrow H_{ads} \tag{A-50}$$

$$H^+ + e^- + H_{ads} \leftrightarrow H_{2\,ads} \tag{A-51}$$

$$H_{ads} + H_{ads} \leftrightarrow H_{2\,ads} \tag{A-52}$$

The hydrogen ions depleted in the cathodic evolution of hydrogen gas are replaced by dissociation of the carbonic acid. Although the dissociation reactions (A-48) and (A-49) are inherently fast, the formation of carbonic acid via the hydration step of aqueous

carbon dioxide (A-47) is the rate determining chemical reaction and is the reason to find the overvoltage response in the presence of a chemical reaction.

The change in the concentration of H^+ ions with respect to time and the distance from the metal surface should be evaluated. Hence Fick's second law in the following form

$$\frac{\partial c}{\partial t} = D\frac{\partial^2 c}{\partial x^2} + \upsilon \tag{A-53}$$

is applied for the change of the concentration (c) of H^+ ions with time (t) and distance (x) from the metal surface as a result of the diffusion and reaction processes where D is the diffusivity of H^+ ions and υ is the reaction rate.

Vetter (Vetter, 1961) proposed the relation for formulation of the homogeneous reaction rate ν,

$$\upsilon = \upsilon_0\left[1-\left(\frac{c}{\bar{c}}\right)^p\right] \tag{A-54}$$

where p is the reaction order, c is the concentration of H^+ ions and $\bar{c}$ is the bulk concentration of the H^+ ions which could be calculated from the pH value of the solution. For the evaluation of the reaction impedance response, the current and overvoltage range in which a linear relationship exists between current i and overvoltage η is of interest. This is true only for relatively small concentration changes.

Since

$$\left(\frac{c}{\bar{c}}\right)^p = \left(1+\frac{c-\bar{c}}{\bar{c}}\right)^p \approx 1+p\frac{c-\bar{c}}{\bar{c}} \tag{A-55}$$

the following is approximately valid:

$$\upsilon = -\frac{\upsilon_0 p}{\bar{c}}\Delta c = -k\Delta c \tag{A-56}$$

where $\Delta c = c - \bar{c}$ and $k = \frac{\upsilon_0 p}{\bar{c}}$

The reaction order in this case is p=1. ν_0 is the rate at which the two opposing reactions meet to establish equilibrium and may therefore be designated as the reaction exchange rate.

Substituting equation (A-56) for the reaction rate into equation (A-53) gives the partial differential equation

$$\frac{\partial \Delta c}{\partial t} = D\frac{\partial^2 \Delta c}{\partial x^2} - k\Delta c \tag{A-57}$$

for the concentration difference $\Delta c(x,t) = c(x,t) - \bar{c}$ where $\bar{c}$ = bulk concentration (=H^+ in this case)

when an alternating current of frequency $\omega/2\pi$, i.e.

$$i = I\sin\omega t \tag{A-58}$$

is given as an input to the system, the concentration of H^+ ions on the surface of the metal (at x=0) can be expressed in the form of a boundary condition as follows:

$$\left(\frac{\partial \Delta c}{\partial x}\right)_{x=0} = -\frac{1}{nFD} I \sin \omega t \qquad \text{(A-59)}$$

In addition, a boundary condition for a finite diffusion boundary layer is also satisfied.

$$\Delta c_{x=\delta} = 0 \qquad \text{(A-60)}$$

where δ= boundary layer thickness (in this case this is equal to $\delta_f + \delta_{mbl,}$ where δ_f is the film thickness and δ_{mbl} is the thickness of the mass transfer boundary layer).

Also, at time t = 0, there is no concentration gradient of H^+ ions, which can be defined as the initial condition

$$\Delta C(x,0) = 0 \text{ for all x} \qquad \text{(A-61)}$$

Using the separation of variable method, one starts by looking for product solutions of the form

$$\Delta c(x,t) = X(x)T(t) \qquad \text{(A-62)}$$

where $X(x)$ is a function of x alone and $T(t)$ is a function of t alone. Plugging into the modified partial differential equation of Fick's second law (A-17), one obtains

$$XT' = DX''T - kXT \qquad \text{(A-63)}$$

After separating the variables, the equation is now in the form of

$$\frac{T'}{T} = \frac{DX''}{X} - k \tag{A-64}$$

For the equality to hold, one must have

$$\frac{T'}{T} = \alpha \text{ and } \frac{DX''}{X} - k = \alpha$$

where α is the separation constant. From these equations, one obtains two ordinary differential equations

$$T' - \alpha T = 0 \tag{A-65}$$

and

$$DX'' - (k + \alpha)X = 0 \tag{A-66}$$

Separating variables in the boundary condition (A-60), we get

$$X(\delta)T(t) = 0 \tag{A-67}$$

If $X(\delta) \neq 0$, then *T(t)* must be 0 for all t, if so, $\Delta c(x,t) = X(x)T(t) = 0$. To avoid trivial solutions we set

$$X(\delta) = 0 \tag{A-68}$$

Hence we obtain the boundary value problem in X:

$$DX'' - (k + \alpha)X = 0, \; X(\delta) = 0$$

with characteristic equation

$$D\lambda^2 - (k+\alpha) = 0 \tag{A-69}$$

Also, one obtains the distinct real characteristic roots of $\lambda_1 = \sqrt{\frac{(k+\alpha)}{D}}$ and $\lambda_2 = -\sqrt{\frac{(k+\alpha)}{D}}$

Therefore the general solution of X of this differential equation is given as

$$X = C_1 e^{\lambda x} + C_2 e^{-\lambda x} \tag{A-70}$$

By applying the boundary condition (A-17),

$$0 = C_1 e^{\lambda\delta} + C_2 e^{-\lambda\delta} \tag{A-71}$$

$$C_1 e^{\lambda\delta} = -C_2 e^{-\lambda\delta} \tag{A-72}$$

$$C_1 = -C_2 \frac{e^{-\lambda\delta}}{e^{\lambda\delta}} \tag{A-73}$$

substitute C_1 into the general solution (A-30) for space domain, we get

$$X(x) = -C_2 \frac{e^{-\lambda\delta}}{e^{\lambda\delta}} e^{\lambda x} + C_2 e^{-\lambda x} \tag{A-74}$$

Doing mathematical manipulation, we can write (A-34) as follows:

$$X(x) = -C_2 \frac{e^{-\lambda\delta}}{e^{\lambda\delta}} e^{\lambda x} + C_2 e^{-\lambda x} \frac{e^{\lambda\delta}}{e^{\lambda\delta}} \tag{A-75}$$

which gives

$$X(x) = \frac{C_2}{e^{\lambda\delta}}\left(e^{\lambda(\delta-x)} - e^{-\lambda(\delta-x)}\right) \tag{A-76}$$

On the other hand, for the time domain,

$$T' - \alpha T = 0 \tag{A-77}$$

The general solution for the above differential equation for the time domain is then given as

$$T(t) = Ae^{\alpha t} \tag{A-78}$$

Combining the two general solutions together, one obtains the general solution of equation (A-62) as follows

$$\Delta c = X(x)T(t) = \frac{C_2}{e^{\lambda\delta}}\left(e^{\lambda(\delta-x)} - e^{-\lambda(\delta-x)}\right)Ae^{\alpha t} \tag{A-79}$$

By partial differentiation of the above equation with respect to *x* and *t*, and by substituting into partial differential equation (A-57) of the modified Fick's second law, the coefficient λ can be obtained

$$\begin{aligned} &i\omega \frac{C_2}{e^{\lambda\delta}}\left(e^{\lambda(\delta-x)} - e^{-\lambda(\delta-x)}\right)Ae^{\alpha t} = \\ &D\lambda^2 \frac{C_2}{e^{\lambda\delta}}\left(e^{\lambda(\delta-x)} - e^{-\lambda(\delta-x)}\right)Ae^{i\omega t} - k\frac{C_2}{e^{\lambda\delta}}\left(e^{\lambda(\delta-x)} - e^{-\lambda(\delta-x)}\right)Ae^{i\omega t} \end{aligned} \tag{A-80}$$

After canceling out the Δc term from the above equation, one obtains

$$\alpha = i\omega = D\lambda^2 - k \tag{A-81}$$

Thus

$$\lambda = \sqrt{\frac{i\omega + k}{D}} \tag{A-82}$$

On the other hand, separating variables in the initial condition, one gets

$$X(x)T(0) = 0 \tag{A-83}$$

Since $X(x) \neq 0$, $T(0)=0$

$$0 = \mathrm{Ae}^{0} \tag{A-84}$$

If A=0, $T(t)=0$ and Δc=0. To avoid a trivial solution, one needs to make use of Euler's identity

$$Ae^{i\omega t} = A(\cos\omega t + i\sin\omega t) \tag{A-85}$$

Now applying the initial condition, one obtains

$$0 = A(\cos 0 + i\sin 0) \tag{A-86}$$

In order for the above equation to hold true, the cos ωt term must be omitted.

Therefore

$$T(t) = i\ A\ sin\omega t \tag{A-87}$$

However, for the purpose of mathematical simplicity, the general solution $T = Ae^{iwt}$ is used for the determination of the coefficient C_2, which can be obtained by applying the boundary condition at the surface (A-59)

$$\frac{C_2}{e^{\lambda\delta}}\left(-\lambda e^{\lambda(\delta-x)} - \lambda e^{-\lambda(\delta-x)}\right)_{x=0} Ae^{i\omega t} = -\frac{1}{nFD} I \sin\omega t \tag{A-88}$$

Simplifying the above equation, we get,

$$-\lambda\frac{C_2}{e^{\lambda\delta}}\left(e^{(\lambda\delta)} + e^{-(\lambda\delta)}\right)Ae^{i\omega t} = -\frac{1}{nFD} I \sin\omega t \tag{A-89}$$

After applying the hyperbolic identity $\cosh(x) = \frac{e^x + e^{-x}}{2}$ and canceling the $I\ sin\omega t$ term on both sides (since $Ae^{iwt} = I\ sin\omega t$), C_2 is then obtained to be

$$C_2 = \frac{e^{\lambda\delta}}{\lambda nFD2\cosh(\lambda\delta)} \tag{A-90}$$

Finally, substituting the coefficient C_2 and applying the hyperbolic identity $\sinh(x) = \frac{e^x - e^{-x}}{2}$ into the general solution in equation (A-79)

$$\Delta c = \frac{\sinh\left[(\delta - x)\lambda\right]}{\lambda nFD\cosh(\delta\lambda)} Ie^{i\omega t} \tag{A-91}$$

where $\lambda = \sqrt{\frac{i\omega + k}{D}}$

The objective of the above concentration derivation is to calculate c(0,t)/$\bar{c}$ at the surface. It was assumed that $|\Delta c|/\bar{c} << 1$ and thus c/$\bar{c} \approx 1$. Therefore the following relation for the reaction overvoltage is approximately valid, (Vetter, 1961)

$$\eta_r = \frac{RT}{nF}\ln\frac{c(0,t)}{\bar{c}} \approx \frac{RT}{nF}\frac{\Delta c(0,t)}{\bar{c}} \tag{A-92}$$

After substituting equation (A-91) for Δc with *x*=0 into the above equation (A-92) and applying the trigonometric identity *tanh(x)=sinh(x)/cosh(x)*, the reaction overvoltage with finite diffusion boundary layer is obtained as follows:

$$\eta_{d,\delta,r} = \frac{RT}{n^2F^2\bar{c}D\lambda}\tanh(\lambda\delta)\, I\sin\omega t \tag{A-93}$$

where $\lambda = \sqrt{\frac{i\omega + k}{D}}$

Hence this expression was used in the results and modeling section to model the experimental data.

APPENDIX B: CALCULATIONS AND ANALYSIS OF LPR DATA

Analysis of LPR data

The anodic and cathodic Tafel slopes β_a and β_c are the functions of temperature. They can be expressed as:

$$\beta_a = \frac{2.303RT}{\alpha_a F} \tag{B-1}$$

$$\beta_c = \frac{2.303RT}{\alpha_c F} \tag{B-2}$$

where,

T is Absolute temperature in K, R is the universal gas constant (8.314 J/mol K), α_a and α_c are the symmetry factors for anodic and cathodic reaction. The values of α_a and α_c are typically 1.5 and 0.5 respectively. F is Faraday's constant (96,500 coulombs/equivalent).

From the above equations the 'B' value can be calculated by using the following expression:

$$B = \frac{\beta_a \beta_c}{2.303(\beta_a + \beta_c)} \tag{B-3}$$

From the above equations (B-1, B-2, B-3), the average value of the 'B' value (B) in the temperature range of 20 °C - 100 °C was calculated to be 14.3 mV.

The corrosion rate was monitored using the linear polarization resistance (LPR) techniques. From the basic electrochemical theory, the corrosion current density i_{corr} (A/m^2) can be described as:

$$i_{corr} = B \times \frac{1}{R_p} \times \frac{1}{A} \tag{B-4}$$

where,

B is the 'B' value explained above, R_p is the corrosion resistance in Ohm, A is the working electrode surface area in m^2.

The corrosion rate (CR) in mm/yr can then be calculated according to the following equation:

$$CR = \frac{m}{At\rho} = \frac{i_{corr} M_w}{\rho n F} = 1.16 i_{corr} \quad \text{(B-5)}$$

where,

m is the metal loss in kg, t is the time in seconds, ρ is the density of the material in kg/m^3, M_w is the molecular weight of iron, F is the Faraday constant, n is the number of electrons exchanged in the electrochemical reaction.

Integrated Average of Corrosion rate

Corrosion rates with time are obtained from the LPR measurements. The area under the curve of LPR corrosion rates with time is integrated using the "Trapezoidal rule" and the value is averaged out for time.

Porosity Calculations

Film porosity (ε) is calculated using the following expression

$$\varepsilon = 1 - \frac{thickness\ of\ 100\%\ dense\ film}{thickness\ of\ \ porous\ \ film} \quad \text{(B-6)}$$

where thickness of porous film is found from SEM images of the cross section, and thickness of 100% film is found out using the following calculations

$$thickness\ of\ 100\%\ dense\ film = \frac{vol\ of\ 100\%\ dense\ film}{A}$$

where A is the cross section area in cm^2 of the specimen and *vol of 100% film* is found using

$$vol\ of\ 100\%\ dense\ film = \frac{W_f - W_{wf}}{\rho}$$

where W_f is the weight of the specimen with the film in gm, W_{wf} is the weight of the specimen with the film cleaned using an inhibited acidic solution in gm, ρ is the density of a 100% $FeCO_3$ film (3.96 gm/cc). The area of cross section of the samples used for weight loss measurements as shown in Figure 16 was 1.12 cm^2.

APPENDIX C: EXPERIMENTAL UNCERTAINTY ANALYSIS

The factors that affect the accuracy of the corrosion rate measurements and calculations include temperature, applied current, applied potential and the working electrode area. According to the Appendix C, corrosion rate can be written as,

$$CR = 1.16 i_{corr} \tag{C-1}$$

where corrosion rate (CR) is expressed in mm/yr, and i_{corr} is in A/m^2

Substituting (B-1) and (B-3) into (C-1) we get,

$$CR = 0.505 \frac{\beta_a \beta_c}{(\beta_a + \beta_c)} \times \frac{1}{R_P} \tag{C-2}$$

Since, β_a and β_c are only dependent on temperature and vary linearly with temperature (Equation B-1, B-2), they can be rewritten as the following equations:

$$\beta_a = \beta_{a0} + m_1 T \tag{C-3}$$

$$\beta_c = \beta_{c0} + m_2 T \tag{C-4}$$

where, β_{a0} and β_{c0} are the base anodic and cathodic Tafel constant at a suitable reference temperature. The slope m_1 and m_2 can be easily obtained by plotting the equation (B-1) and (B-2). The values obtained are $m_1 = 0.14$ mV/K and $m_2 = -0.4$ mV/K.

In equation (C-2), R_p can be expressed as follows:

$$R_P = \frac{dE}{di_{app}} \tag{C-5}$$

where, i_{app} is the applied current density in A/m^2

$$i_{app} = \frac{I_{app}}{a} \tag{C-6}$$

where, I_{app} is the applied current in A and a is the working area in cm^2

Substituting equation (C-3) to (C-6) in equation (C-2), we get

$$CR = 0.505\frac{(\beta_{a0} + m_1 T)(\beta_{c0} + m_2 T)}{\beta_{a0} + \beta_{c0} + (m_1 + m_2)T} \times \frac{\Delta I_{app}}{\Delta E \Delta a} \tag{C-7}$$

Above equation can then be written in the following form:

$$CR = 0.505(\beta_{a0} + m_1 T)(\beta_{c0} + m_2 T)[\beta_{a0} + \beta_{a0} + (m_1 + m_2)T](\Delta I_{app})(\Delta E)^{-1}(\Delta a)^{-1} \tag{C-8}$$

The sensitivity of small changes in the corrosion rate to small changes in each variable is expressed by taking partial derivatives of the corrosion rate with respect to each variable. The errors in β_{a0}, β_{c0}, m_1 and m_2 are assumed to be negligible. Thus, the absolute uncertainty in the measurement of corrosion rate because of uncertainties in the system variables can be expressed as follows:

$$\frac{\delta(CR)}{CR} = \left[\frac{\partial(CR)}{\partial T}\right]\frac{\delta T}{CR} + 2\left[\frac{\partial(CR)}{\partial E}\right]\frac{\delta E}{CR} + 2\left[\frac{\partial(CR)}{\partial I_{app}}\right]\frac{\delta I_{app}}{CR} + 2\left[\frac{\partial(CR)}{\partial a}\right]\frac{\delta a}{CR} \tag{C-9}$$

Deriving the partial derivatives of each item above according to equation (C-8) and then substituting into (C-8), the following equation is obtained:

$$\frac{\delta(CR)}{CR} = \left(\frac{m_1}{\beta_a} + \frac{m_2}{\beta_c}\right)\delta T - \frac{2}{E}\delta E + \frac{2}{I_{app}}\delta I_{app} - \frac{2}{a}\delta a \tag{C-10}$$

Therefore, the corrosion rate uncertainty above can be considered an overall uncertainty through the experiment for LPR techniques. It considers the uncertainties due to the temperature, due to instrumentation (potential and applied current), and due the working electrode surface area. The contribution of each item in (C-10) to the corrosion rate uncertainty measurements is calculated as follows:

Temperature

The temperature during the experiment was maintained at 60 °C ± 0.2 °C, thus δT=0.2. Tafel slopes calculated at 60 °C are, β_a = 40 mV and β_c = 120 mV. Hence the first part on the right hand side of the equation (C-10) is:

$$\left(\frac{m_1}{\beta_a}+\frac{m_2}{\beta_c}\right)\delta T=\left(\frac{0.14}{40}+\frac{-0.4}{120}\right)\times 0.2=4.09\times 10^{-4} \quad \text{(C-11)}$$

Potential

According to Gamry, the DC accuracy in voltage measurement is ±0.3% range ±1 mV. During the experiment, the applied potential was ±5 mV over the open circuit potential. Thus the uncertainty in the potential would be δE = 1.03 mV. The error in the potential could be different for measurements before and after formation of the iron carbonate scale or the inhibitor film. Before the formation of the scale, the *Rp* was determined over the entire applied potential since there was a linear relationship between the potential and the current, as shown in Figure 59. Hence, the absolute uncertainty due to the potential in equation (C-10) can be described as:

$$\frac{2}{E}\delta E=\frac{2}{10}\times 1.03=0.206 \quad \text{(C-12)}$$

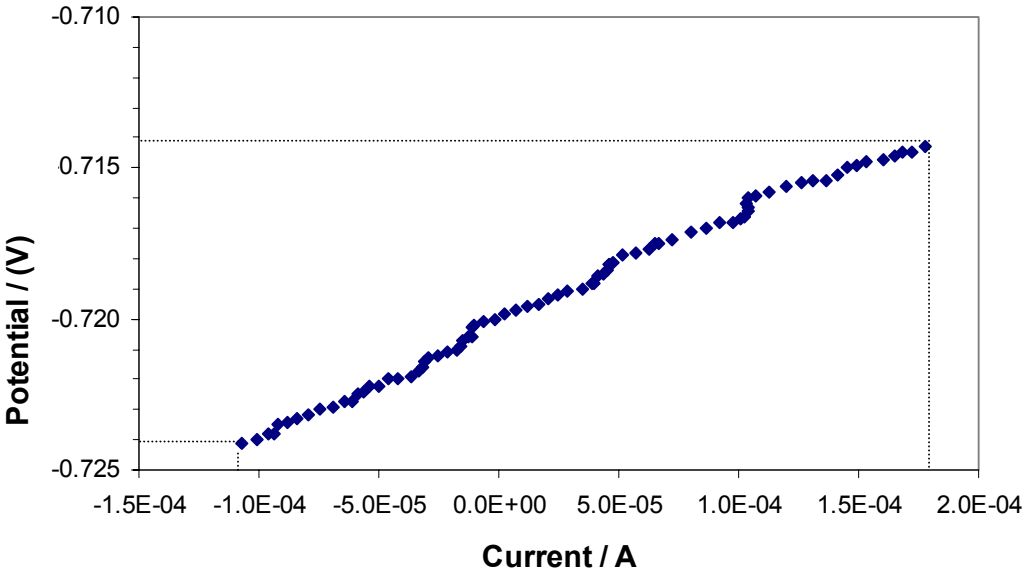

Figure 59. A typical linear polarization curve obtained in experiments before the formation of film.

However, after the film was formed on the metal surface, the linear relationship did not exist over the entire applied potential, as indicated Figure 60**.** The actual potential used to get the *Rp* was only taken from the linear region, which was a 3 mV range. Thus the absolute uncertainty after the scale formation is:

$$\frac{2}{E}\delta E = \frac{2}{3} \times 1.03 = 0.343 \qquad \text{(C-13)}$$

Hence, depending on when the LPR was taken, the error due to the potential measurement should be somewhere in between with and without film formation.

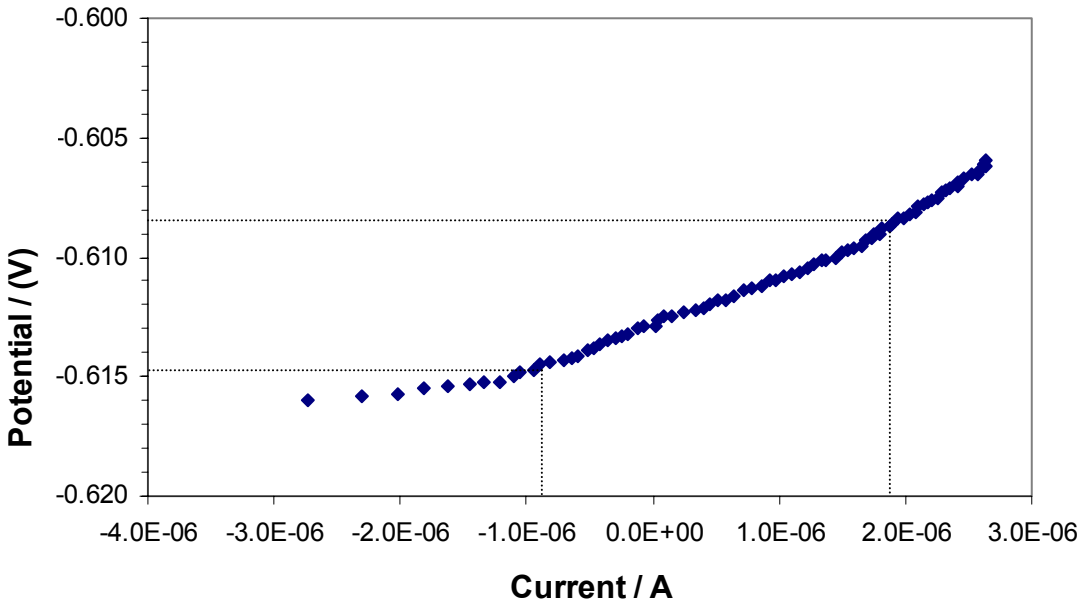

Figure 60. A typical linear polarization curve obtained in experiments after scale formation.

Current

According to Gamry, the DC accuracy in current measurement is ±0.3% range ±50 pA. The current range was different for different experiments, and varied with time because of the change in the corrosion rate. During the start of the experiment, the applied current range is usually around 400 μA. Thus the uncertainty in the current would be:

$$\delta I_{app} = 4 \times 10^{-4} \times 0.003 = 1.2 \times 10^{-6}\, A \qquad \text{(C-14)}$$

Hence, the absolute uncertainty in the equation (C-10), due to the current would be:

$$\frac{2}{I_{app}}\delta I_{app} = \frac{2}{4\times10^{-4}}\times1.2\times10^{-6} = 6.0\times10^{-3} \quad \text{(C-15)}$$

After the formation of the film, since the corrosion rate reduced, the applied current was reduced to about 4 μA. Thus the uncertainty in the current would be:

$$\delta I_{app} = 1.2\times10^{-8}\,A \quad \text{(C-16)}$$

Hence, the absolute uncertainty in the equation (C-10), due to the current would be:

$$\frac{2}{I_{app}}\delta I_{app} = \frac{2}{4\times10^{-6}}\times1.2\times10^{-8} = 6.0\times10^{-3} \quad \text{(C-17)}$$

Hence, , the error in corrosion rate due to the current is found from the above equation.

Electrode Area

The uncertainty in the area was due to the accuracy of the measuring instrument, the loss of area due to the polishing of the sample and corrosion loss of the reused sample. It was estimated to be 0.01 cm^2. Therefore, the absolute uncertainty due to the surface area in equation (C-10) is:

$$\frac{2}{a}\delta a = \frac{2}{5.4}\times0.01 = 3.7\times10^{-3} \quad \text{(C-18)}$$

Thus the uncertainties in the corrosion rate measurement from the LPR techniques for the specified experiment are expressed as:

$$\frac{\delta(CR)}{CR} = \pm\left(4.09\times10^{-4} - \frac{0.206+0.343}{2} + 6.0\times10^{-3} - 3.7\times10^{-3}\right) = \pm27.2\% \quad \text{(C-19)}$$

From the above equations, it can be concluded that in the LPR measurement techniques, the uncertainty in the potential is a major source of error in corrosion rate. The error calculated in equation (C-19) would be the average error over entire length of

the experiment. Hence, at the beginning of the experiment, the error could be about 20% while, towards the end of the experiment, after formation of the iron carbonate scale or the iron sulfide scale, the error could be 34%.